UNIVERSIDADE ESTADUAL PAULISTA
"JÚLIO DE MESQUITA FILHO"

UNIVERSIDADE ESTADUAL PAULISTA
Faculdade de Engenharia de São João da Boa Vista

Nawar Darweesh

Wideband Series-Fed Microstrip Array Antenna with Low Side-Lobe Level for Millimeter-Wave Applications

São João da Boa Vista

2025

Nawar Darweesh

Wideband Series-Fed Microstrip Array Antenna with Low Side-Lobe Level for Millimeter-Wave Applications

Dissertation presented to the School of Engineering of São Paulo State University, São João da Boa Vista Campus, as a partial requirement for the Master's degree in Electrical Engineering within the Graduate Program in Electrical Engineering.

Concentration Area: Electronic Systems

Universidade Estadual Paulista

Supervisor: Prof. Dr. Rafael Abrantes Penchel
Co-supervisor: Prof. Dr. Renan Alves dos Santos

São João da Boa Vista
2025

D228w

Darweesh, Nawar Younis
Wideband Series-Fed Microstrip Array Antenna with Low Side-Lobe Level for Millimeter-Wave Applications / Nawar Younis Darweesh. -- São João da Boa Vista, 2025
114 p.

Dissertação (mestrado) - Universidade Estadual Paulista (UNESP), Faculdade de Engenharia, São João da Boa Vista
Orientador: Prof. Dr. Rafael Abrantes Penchel
Coorientador: Prof. Dr. Renan Alves dos Santos

1. Arranjos de antenas em série. 2. MnM interposer. 3. membrana de nanofios metalicos (MnM). 4. Millimeter-Wave (mmW). 5. Series-fed array antennas. I. Título.

Sistema de geração automática de fichas catalográficas da Unesp. Dados fornecidos pelo autor(a).

Nawar Darweesh

Wideband Series-Fed Microstrip Array Antenna with Low Side-Lobe Level for Millimeter-Wave Applications

Dissertation presented to the School of Engineering of São Paulo State University, São João da Boa Vista Campus, as a partial requirement for the Master's degree in Electrical Engineering within the Graduate Program in Electrical Engineering.

Concentration Area: Electronic Systems

EXAMINATION BOARD

Prof. Dr. Rafael Abrantes Penchel
FESJ/Unesp

Prof. Dr. Renan Alves dos Santos
FEE/UFU

Prof. Dr. Ivan Aldaya
FESJ/Unesp

Prof. Dr. Gustavo Pamplona Rehder
Poli/USP

UNIVERSIDADE ESTADUAL PAULISTA

Câmpus de São João da Boa Vista

CERTIFICADO DE APROVAÇÃO

TÍTULO DA DISSERTAÇÃO: Wideband Series-Fed Microstrip Array Antenna with Low Side-Lobe Level for Millimeter-Wave Applications

AUTOR: NAWAR DARWEESH
ORIENTADOR: RAFAEL ABRANTES PENCHEL

Aprovado no Exame Geral de qualificação no programa de Pós-Graduação em Engenharia Elétrica, Curso de Mestrado Acadêmico, área: Sistemas Eletrônicos, pela Comissão Examinadora:

Prof. Dr. RAFAEL ABRANTES PENCHEL (Participaçao Virtual)
Departamento de Engenharia Eletronica e de Telecomunicacoes / Faculdade de Engenharia de Sao Joao da Boa Vista UNESP

Prof. Dr. RENAN ALVES DOS SANTOS (Participaçao Virtual)
Faculdade de Engenharia Elétrica / Universidade Federal de Uberlândia

Prof. Dr. GUSTAVO PAMPLONA REHDER (Participaçao Virtual)
Escola Politécnica (EP) / Universidade de São Paulo (USP)

Prof. Dr. IVAN ARITZ ALDAYA GARDE (Participaçao Virtual)
Departamento de Engenharia Eletronica e de Telecomunicacoes / Faculdade de Engenharia de Sao Joao da Boa Vista UNESP

Faculdade de Engenharia - Câmpus de São João da Boa Vista -
Profª Isette Corrêa Fontão, 505, 13876750, São João da Boa Vista - São Paulo
http://www.sorocaba.unesp.br/#!/pos-graduacao/--engenharia-eletrica-local/CNPJ: 48031918004111.

São João da Boa Vista, 25 de junho de 2025.

Verônica Liberali Messias
Supervisora Técnica de Seção
Seção Técnica de Graduação e Pós-Graduação

Assinado de forma
digital por Veronica
Liberali
Messias:36823715839
Dados: 2025.07.01
09:53:22 -03'00'

بسم الله الرحمن الرحيم

In the name of God, the most Gracious, the most Merciful

Acknowledgements

Firstly, I would like to express my sincere gratitude to my family for their continuous support throughout this academic journey. I am especially thankful to my parents, Younis and Rajaa, for the values they taught me, for always encouraging me to be resilient and honest. I am also grateful for their support during the most critical stages of my personal and professional development. I also thank my brothers, Manar and Maiar, for their advice, support, and for ensuring that everything remained in order at home during my absence.

A special dedication go to Renata, my partner, bride, and future wife, I am deeply grateful for her patience, support, and unconditional encouragement throughout the most challenging phases of this work. Her presence has been fundamental to the completion of this thesis.

I would like to thank all the members of the examination board, my co-supervisor, Prof. Dr. Renan Alves dos Santos, Prof. Dr. Ivan Aldaya, and a special thanks for Prof. Dr. Gustavo Pamplona Rehder from the Department of Electronic Systems at the Polytechnic School of the University of São Paulo (USP) for fabricating and characterising the devices studied in this work. And of course, for my advisor, Prof. Rafael Abrantes Penchel, for his immeasurable support and guidance throughout this work. His mentorship has been instrumental in my development since my undergraduate years. His technical insight and dedication were essential in shaping my research path and fostering my long-standing interest in wireless communication systems and transmission devices. Thank you very much for your confidence in me and for this great opportunity.

Finally, thank God, the main responsible for getting me this far, for the gift of life and for always guiding me on my journey, and for my family, and all the experiences, lessons and opportunities he has given me over the years. I am very grateful for everything and everyone that God has put in my path for a reason. Thank you, God, for everything.

I also extend my appreciation to everyone who, in any way, contributed to this achievement. This work is the result of collective effort and reinforces the essential role of collaboration in scientific progress. This study was financed in part by the Coodernação de Aperfeiçoamento de Pessoal de Nível Superior- Brasil (CAPES) - Finance Code 001.

“Knowledge is light, while ignorance is darkness.”

Old popular proverb

Resumo

Este trabalho apresenta um estudo técnico voltado ao projeto e ao desenvolvimento de arranjos de antenas microfita retangulares alimentadas em série para operação em ondas milimétricas. Foram projetados e otimizados arranjos em série compostos por dois, quatro e oito elementos. A adaptação de impedância dos arranjos foi realizada por meio de um transformador de um quarto de comprimento de onda. Análises paramétricas foram conduzidas variando-se as larguras da linha de transmissão e do transformador, com o objetivo de alcançar desempenho de banda larga.

A resposta de banda larga desejada foi obtida apenas quando a arquitetura em série incorporou oito elementos ressonantes. Dois arranjos foram projetados para operar nas faixas de 60 GHz e 79 GHz, amplamente empregadas em sistemas de radar automotivo.

Na segunda etapa do estudo, técnicas de otimização foram aplicadas com o objetivo de reduzir os níveis de lóbulos laterais do diagrama de ganho do arranjo. No Capítulo 2, é apresentado um estudo sobre técnicas de síntese de arranjos não uniformes. Diversos métodos de atenuação de amplitude são discutidos e posteriormente aplicados ao projeto de arranjos lineares não uniformes. Entre os métodos avaliados, a distribuição de amplitude Dolph–Chebyshev proporcionou o comportamento mais adequado entre largura do lóbulo principal e supressão no nível dos lóbulos laterais.

Por fim, a antena foi fabricada utilizando a tecnologia emergente Millimetric-Nanowire-Membrane (MnM), que emprega alumina nanoporosa preenchida com cobre para implementar interconexões verticais entre as camadas do dispositivo. Medições experimentais foram realizadas, e os resultados demonstraram boa concordância com os dados simulados.

Palavras-chave: arranjos de antenas em série; ondas milimetricas (mmWave); membrana de nanofios metalicos (MnM).

Abstract

This work presents a technical study focused on the design and development of series-fed rectangular microstrip antenna arrays for mmWave operation. Series antenna arrays consisting of two, four, and eight elements were designed and optimized. The arrays were impedance-matched using a quarter-wave transformer. Parametric analyses were conducted by varying the widths of transmission line and the transformer to achieve broadband performance.

The desired wideband response was obtained only when the series architecture incorporated eight radiating elements. Two arrays were designed to operate in the 60 GHz and 79 GHz bands, which are widely employed in automotive radar systems.

In the second phase of the study, optimization techniques were applied to reduce the side-lobe levels of the array gain pattern. In Chapter 2, a study on non-uniform array synthesis techniques is presented. Various amplitude tapering methods are discussed and subsequently applied in the design of non-uniform linear arrays. Among the evaluated methods, the Dolph–Chebyshev amplitude distribution provided the most suitable trade-off between main-lobe width and side-lobe suppression.

Finally, the antenna was fabricated using the emerging Millimetric-Nanowire-Membrane (MnM) technology, which employs nanoporous alumina filled with copper to implement vertical interconnects between device layers. Experimental measurements were performed and the results demonstrated good agreement with the simulated data.

Keywords: millimeter-wave (mmWave); series-fed array antennas; MnM interposer.

List of Figures

List of Tables

List of abbreviations and acronyms

1G	First-Generation
2G	Second-Generation
3G	Third-Generation
4G	Fourth-Generation
5G	Fifth-Generation
6G	Sixth-Generation
ADAS	Advanced Driver Assistance System
ACC	Adaptive Cruise Control
AMC	Artificial Magnetic Conductor
AWACS	Airborne Warning and Control System
AEB	Automatic Emergency Braking
AAO	Anodic Aluminum Oxide
AiP	Antenna-in-Package
AoP	Antenna-on-Package
BPS	Bits-per-second
BSD	Blind Spot Detection
CDMA	Code Division Multiple Access
CMOS	Complementary Metal-Oxide-Semiconductor
CNPQ	Brazilian agencies National Council for Scientific and Technological Development
dB	Decibels
dBi	Decibels relative to isotropic radiator
dBic	Decibels relative to isotropic radiator circularly polarized
FAPESP	São Paulo Research Foundation

FINEP	Financier of Studies and Projects
FoV	Field-of-View
FCW	Forward Collision Warning
FEM	Finite Element Method
GCPW	Grounded Coplanar Waveguide
GaN	Gallium Nitride
GSM	Global System for Mobile
GNSS	Global Navigation Satellite System
GSG	Ground-Signal-Ground
HPBW	Half-Power Beamwidths
Hz	Hertz
HFSS	High Frequency Structure Simulator
IoT	Internet of Things
LKA	Lane Keeping Assist
M2M	Machine-to-Machine
MMIC	Monolithic Microwave Integrated Circuits
MnM	Metallic Nanowire Membrane
mmW	Millimeter-Wave
MEMS	Microelectromechanical Systems
mm	Millimeter
PAE	Power-Added Efficiency
PCB	Printed Circuit Board
QWT	Quarter Wave Transformer
QoS	Quality of Service
RO4830	Rogers Duroid RO4830
RO3003	Rogers Duroid RO3003

RO4350B	Rogers Duroid 4350B
ROCLTE-XT	Rogers CLTE-XT
RFIC	Radio Frequency Integrated Circuit
RF	Radio Frequency
SDV	Software-Defined-Vehicles
SMS	Short Message Service
SC	Suspended Cavity
SRR	Short-Range-Radar
SiP	System-in-Package
SMVs	Stacked Microvias
SiO_2	Silicon Dioxide
SLL	Sidelobe level
SFSP	Single Feed Single Patch
3D-IC	Three-Dimensional Integrated Circuit
TSVs	Through-Silicon Via
TL	Transmission Line
Wi-Fi	Wireless Fidelity
WiGig	Wireless Gigabit
V2V	Vehicle-to-Vehicle
V2X	Vehicle-to-Everything
VLS	Vapor-Liquid-Solid

CONTENTS

1 Introduction

1.1 Contextualization

The increasing demand for spectrum resources, driven by high data rates, a large number of connections, and machine-to-machine (M2M) communications, poses significant challenges for both industry and academia in developing innovative wireless systems. This demand has directed research efforts toward the exploration of millimeter-wave (mmWave) frequency bands. Recognized as critical for current and emerging wireless technologies, the mmWave bands enable applications such as 5G and 6G networks, automotive radar, satellite communications, remote sensing, and medical imaging. These bands offer substantial bandwidth, low latency, and high spatial resolution, effectively addressing the requirements of advanced connectivity and sensing applications (Secgin, 2023).

The evolution of mobile telephony exemplifies the progression of wireless communication systems. First-generation (1G) networks, introduced in the 1970s and 1980s, operated at 800–900 MHz with data rates of 2.4 kbps, supporting only voice calls. In the 1990s, second-generation (2G) systems adopted digital technologies (GSM/CDMA) at 800–1900 MHz, achieving 64 kbps and enabling SMS. The 2000s saw third-generation (3G) networks expand to 1.8–2.5 GHz, offering 384 kbps to 2 Mbps for mobile data and video conferencing. Fourth-generation (4G) networks, deployed in the 2010s at 700–2.6 GHz, reached 1 Gbps, supporting streaming and IoT applications. Since 2020, fifth-generation (5G) networks have utilized sub-6 GHz and millimeter-wave bands (24–100 GHz), delivering over 10 Gbps with sub-1 ms latency, enabling autonomous vehicles and smart grids (Secgin, 2023). Sixth-generation (6G) networks, anticipated for the 2030s, aim to leverage sub-terahertz bands (100–300 GHz) to achieve 1 Tbps, integrating artificial intelligence and ubiquitous connectivity for smart cities and holographic teleportation (Saad; Bennis; Chen, 2020). The adoption of millimeter-wave bands in 5G and 6G standards addresses the increasing demand for high connection density, low latency, and elevated data rates. Consequently, smaller coverage cells necessitate a higher density of optimized radio base stations.

The development of high-performance radio-frequency (RF) systems operating in the millimeter-wave (mmWave) bands faces several challenges related to device design and implementation. Major limitations include the low power-added efficiency (PAE) of amplifiers, typically below 15–20% at 60 GHz in CMOS technologies (Dawn et al., 2011), and the unfavorable propagation characteristics inherent to mmWave frequencies. These include high atmospheric absorption (Narekar; Bhalerao, 2015), significant rain attenuation (Shamsan, 2020), elevated path loss in urban environments (Maccartney et al.,

Figure 1. Applications for millimeter waves at 60GHz-range.

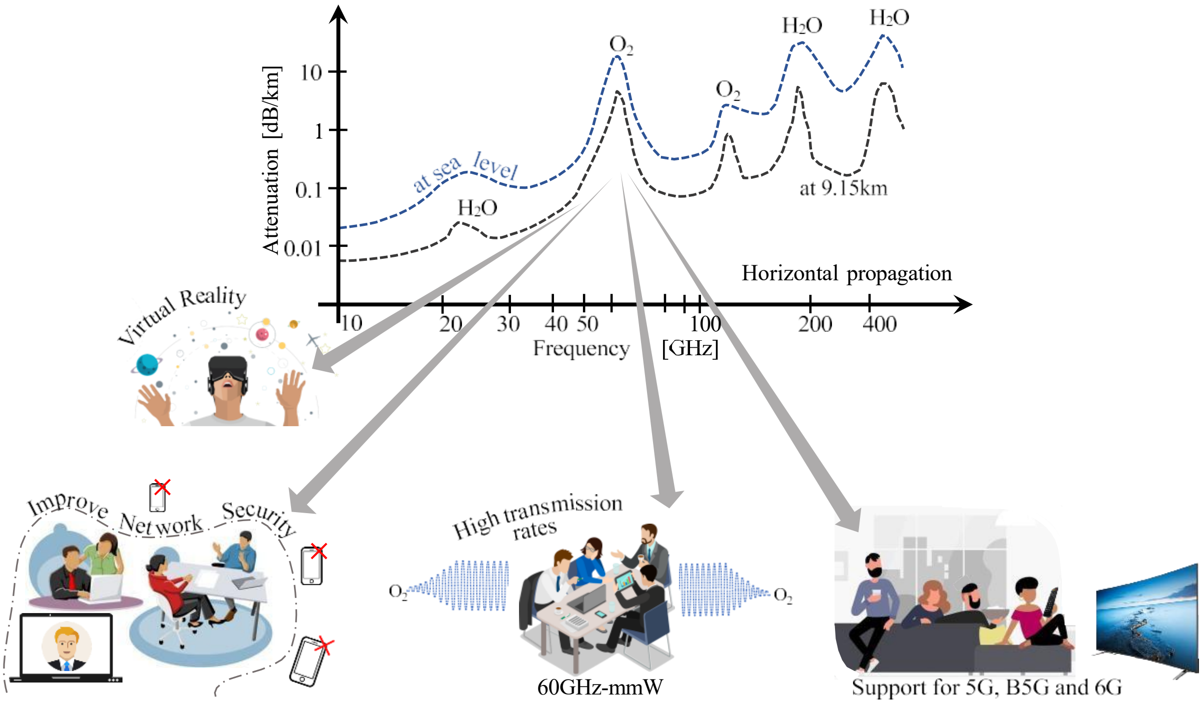

Source: Prepared by the author, 2024

2013), limited diffraction (Kim et al., 2020), multipath delay spread (Zhang et al., 2020), and foliage-induced losses (Rahim et al., 2017). Such effects hinder the establishment of reliable and efficient communication links. Figure 1 summarizes the principal atmospheric mechanisms that influence the operational performance of mmWave systems. Experimental results indicate that heavy rainfall (150 mm/h) can reduce the effective detection range of mmWave automotive radars by approximately 45% (Zang et al., 2019). Between the 60- and 80-GHz bands, atmospheric oxygen absorption exhibits a pronounced peak caused by molecular resonance. This intrinsic absorption attenuates external interference, which is advantageous for short-range interference rejection in automotive radar systems. Because distant signals are strongly attenuated, the receiver is less exposed to unintended high-power interferers. This effect directly supports the atmospheric interference-mitigation behavior highlighted in Figure 1, as the 60-GHz O_2 absorption peak naturally limits interference to short operational distances.

The use of antenna arrays represents a key approach to mitigating the aforementioned challenges. Arrays enable the control, synthesis, and optimization of radiation patterns to concentrate power in desired directions. Techniques such as beamforming and beamsteering, implemented in discrete-element antenna arrays (Balanis, 2016, Ch. 6), enhance directivity and gain while reducing the effects of path loss, fading, and multipath propagation. Beamforming adjusts the amplitude and phase excitation of array elements to shape or steer the radiation pattern, thereby focusing energy toward specific directions. Beamsteering provides dynamic control of the main beam direction in phased arrays by varying the relative phase and amplitude of individual elements (Balanis, 2016, Ch. 6).

In this context, the 60- and 79-GHz frequency bands are particularly suitable for addressing the challenges faced by the automotive industry. However, a critical factor for the practical deployment and consolidation of such systems lies in the development of devices capable of maintaining operational reliability in the presence of external electromagnetic interference. In particular, antenna systems must exhibit radiation patterns with high directivity and main-lobe gain, while simultaneously ensuring low side-lobe levels (SLL) to minimize undesired radiation and susceptibility to interference. These characteristics are essential to enhance the performance and robustness of wireless communication links in vehicular environments (Abir; Chowdhury; Jang, 2023).

Another major challenge concerns the fabrication of mmWave devices. High production costs arise from the requirement for specialized infrastructures, such as CMOS or GaN microfabrication facilities, which hinder large-scale and cost-effective manufacturing (Dawn et al., 2011). The realization of complex geometries, including antenna arrays and metasurfaces, is limited by the precision and flexibility of conventional fabrication methods, restricting the implementation of intricate structures critical for mmWave operation (Whittow; Churm; Vardaxoglou, 2019). Additional challenges include the sensitivity to micrometer-scale tolerances, where surface roughness variations degrade radiation efficiency (Bansal et al., 2024), and thermal management issues in miniaturized components, which affect reliability at high frequencies. Consequently, mmWave device fabrication remains both technically demanding and economically challenging.

Emerging technologies such as Three-Dimensional Integrated Circuits (3D-ICs) have gained prominence as a viable approach to enhance the performance and miniaturization of resonant devices operating at mmW frequencies. This method enables the vertical stacking of functional layers—such as active circuits, passive components, and distinct substrates—within a single compact structure, thereby reducing signal losses and electromagnetic interference by shortening interconnect lengths. A key advantage of this approach is the ability to combine disparate technologies within the same system. For instance, ceramic substrates can be employed for resonators, while CMOS silicon technology is used for control circuitry, thus optimizing system performance and potentially reducing overall costs (Theeda; Kumar, 2025). Additionally, this architecture improves electromagnetic efficiency and reduces device footprint, making it well suited for compact, high-frequency applications.

Nevertheless, several technical challenges remain, including precise layer alignment, thermal management, and the complexity of vertical interconnections, which contribute to elevated initial development costs. Despite these challenges, as industrial processes mature, 3D heterogeneous integration is expected to become a key enabling technology for high-performance mmW systems. In the meantime, Metallic Nanowire Membranes (MnM)

Figure 2. Schematic 3D-integration

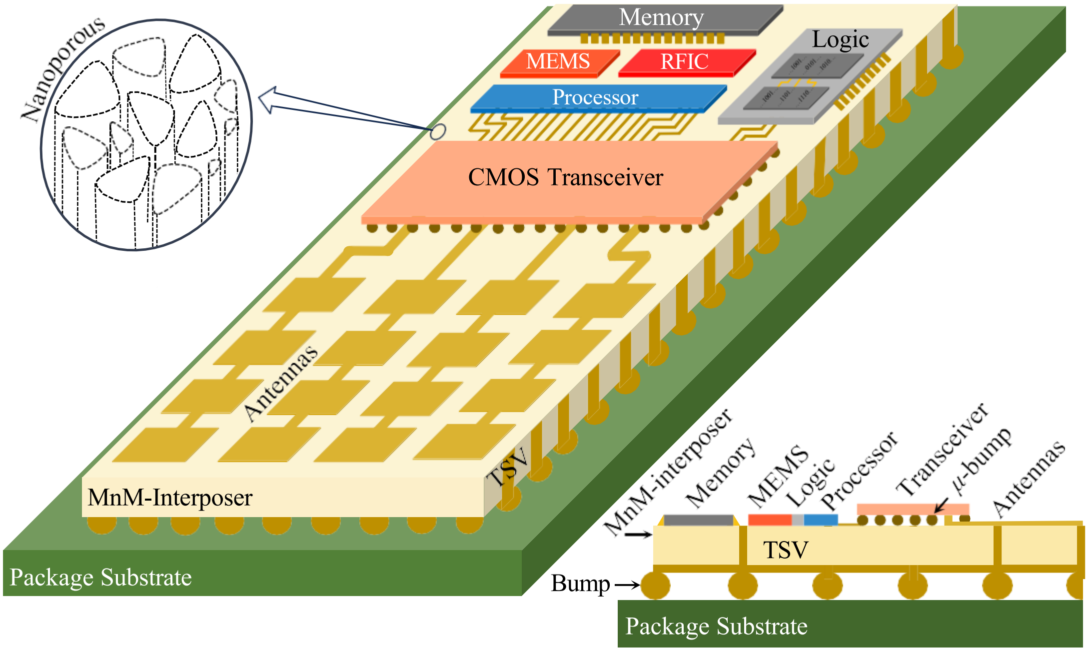

Source: Prepared by the author, 2024

technology emerges as a promising solution to these challenges, providing flexible and lightweight membranes formed by three-dimensional networks of metallic nanowires with nanometric dimensions and high electrical conductivity (Pelegrini et al., 2016b).

In summary, two major research challenges emerge from the current state of mmWave technology. The first lies in the design of high-gain antenna arrays capable of achieving low side-lobe levels (SLL) without compromising bandwidth or radiation efficiency. Advanced amplitude tapering, array synthesis, and beamforming techniques must be explored to ensure precise control of the radiation pattern and suppression of undesired emissions. The second challenge concerns the fabrication of these arrays with the precision required for operation at mmW frequencies. Achieving submicrometer accuracy, low surface roughness, and cost-effective production remains a critical barrier.

1.2 State of the Art in Series-Fed Microstrip Array Antennas

This section provides a structured review of the main contributions related to series-fed rectangular microstrip patch antenna arrays. As outlined earlier, the objective is to identify and consolidate key academic works on antenna array design, focusing on configurations with both uniform and non-uniform element spacing for radiation pattern synthesis and side-lobe level (SLL) optimization.

The literature on series-fed microstrip patch antenna arrays in the 60 GHz band includes several representative approaches. In (Lee et al., 2024), a compact three-element array achieves a 5.78 GHz bandwidth (60.95–66.73 GHz) centered at 62.5 GHz, with impedance matching provided by symmetric inset slots and optimized patch dimensions on a Rogers RO4830 substrate (ε_r = 3.23, tan δ = 0.0033, thickness 0.125 mm). The array measures 1.41 mm × 7.04 mm and reaches a maximum realized gain of 10.24 dBi with half-power beamwidth (HPBW) of 33.96° and 76.19° in the E- and H-planes, respectively; SLL was not reported. Similarly, (Li; Matos; Ghalichechian, 2021) presents a low-cost, high-efficiency PCB-fabricated array on Rogers CLTE-XT (ε_r = 2.94, tan δ = 0.0012, thickness 0.254 mm), achieving 3.6 GHz bandwidth and gains of 18.5 dBi and 18.7 dBi in the E- and H-planes. A four-element series-fed array for 60 GHz AiP integration is reported in (Govindarajulu; Hokayem; Alwan, 2021), covering 58.46–62.14 GHz with 3.6 GHz bandwidth, 10.51 dBi peak gain, 14 dB SLL, and dimensions 9.6 mm × 2.8 mm × 0.568 mm on Isola Tachyon (ε_r = 3.02, tan δ = 0.0021, thickness 0.13 mm). Finally, (Xu et al., 2023) employs MEMS technology to realize a three-element, non-uniformly spaced series-fed array with a suspended-cavity structure on quartz glass (ε_r = 3.78), operating from 57 to 66 GHz, achieving SLL below −20 dB and a main-lobe width smaller than 60°. These studies collectively illustrate design strategies, substrate choices, fabrication methods, and performance metrics for compact high-frequency arrays, providing insights into bandwidth, gain, and SLL control at mmWave frequencies.

Extending the review to the 77 GHz band, several studies illustrate different design strategies for automotive mmWave applications. In (Kang; Noh; Kim, 2020), a progressive-wave series-fed microstrip array is proposed for 76.5 GHz operation with a 3 GHz bandwidth (75–78 GHz). The design employs microstrip elements optimized via a radiated-to-available power ratio (RARP) method to control radiated power and minimize SLL. Numerical analysis of three antenna configurations demonstrates that an eight-element array achieves SLL below −17 dB through tailored element excitation. Fabrication details are not provided. Similarly, (Tan et al., 2020) presents a ten-element series-fed array designed for 78 GHz, covering 76.9–79.4 GHz, optimized through a hybrid HFSS-MATLAB procedure to determine patch widths and inter-element spacing. The array achieves a return loss of −10 dB, a stable peak gain of 16.2 dBi, and an SLL of −23.5 dB, using sequential element variations for SLL suppression. In (Xu et al., 2017), an array-of-arrays configuration operating at 77 GHz is realized on a Taconic TLY-5 substrate (ε_r = 2.2, tan δ = 0.0009, thickness 0.254 mm) via standard PCB fabrication. The array employs a three-way power divider with a binomial amplitude distribution, achieving an SLL of −15 dB, a gain of 20 dBi, and a bandwidth of approximately 5 GHz (75–80 GHz). These studies collectively demonstrate diverse optimization techniques, amplitude tapering strategies, and fabrication approaches for achieving high-gain, low-SLL series-fed microstrip arrays at 77 GHz.

Focusing on the 79 GHz band, several studies illustrate diverse design strategies for improving impedance bandwidth, suppressing side-lobe levels (SLL), and enhancing radiation performance. In (Tan et al., 2022), a six-element linear microstrip array with a grounded coplanar waveguide (GCPW) feed and artificial magnetic conductor (AMC) achieves 3 GHz bandwidth (77–80 GHz), gains of 22 dBi, and SLLs of –24 dB and –23 dB in the E- and H-planes, respectively, via a hybrid HFSS–MATLAB optimization. Similarly, (Liu; Bai; Yagoub, 2020) employs parasitic patches and tapered element sizing in an 8×6 array, obtaining 4.14 GHz bandwidth, 22 dBi gain, and SLLs of –19 dB and –17 dB. In (Chong; Wenbin, 2012), a 16×20 two-dimensional conical array uses a four-stage T-junction divider with Taylor amplitude distribution to achieve 29 dBi gain, SLLs of –17 dB and –19 dB, and 4 GHz bandwidth (77–81 GHz), while compact layout reduces feed losses. A combined loop-patch multilayer array in (Kashino; Uno; Sato, 2014) covers 77–81 GHz, delivering 20.5–21.5 dBi gain and SLL below –15 dB. For compactness and SLL reduction, (Dash; Sarkar; Antar, 2023) introduces an 11-element array with modified tapering and parasitic loading, achieving 13.1 dBi gain, SLL of –22 dB, 7% improvement in azimuth field of view, and 47% bandwidth enhancement versus uniform arrays. In (Mohan et al., 2023), a Dolph–Tschebyshev taper and transmission-line impedance-matching network on Rogers 4350B yields 76.73–86 GHz bandwidth and 13.73 dBi gain at 81.44 GHz. Finally, (Aliakbari et al., 2022) presents a multilayer series-fed array with stacked microvias, covering 74.5–85.81 GHz, with 12.67 dBi peak gain and SLL better than –13 dB, demonstrating the feasibility of PCB-based structures for low-cost, high-resolution automotive radar systems. These works collectively illustrate the effectiveness of amplitude tapering, parasitic loading, and multilayer integration in achieving high-gain, low-SLL arrays at 79 GHz.

Extending this analysis to sub-THz frequencies, (Oh; Oh, 2023) presents an antenna-on-package (AoP) transceiver for D-band operation at 140 GHz, fabricated using standard PCB processes. The transmitter comprises a two-element array with 6.3 GHz bandwidth, 9.8 dBi peak gain, and physical dimensions of 1.91 mm × 1.87 mm, while the receiver consists of a four-element array with 11.5 GHz bandwidth, 11.8 dBi peak gain, and dimensions of 3.41 mm × 1.59 mm. Both arrays are integrated into a radio-frequency integrated circuit (RFIC) platform, achieving SLL suppression of –17 dB and –10 dB for the transmitter and receiver, respectively. These results illustrate the feasibility of compact, high-gain, and low-SLL antenna arrays at sub-THz frequencies, highlighting the potential for AoP-based mmW and sub-THz transceivers in next-generation radar and communication systems.

In summary, the presented works cover series-fed microstrip array designs operating in the 60 GHz, 77–81 GHz, and sub-THz (140 GHz) frequency bands. These studies demonstrate the versatility of series-fed arrays in addressing millimeter-wave radar requirements, employing diverse strategies for bandwidth enhancement, side-lobe level (SLL) suppression, and compact integration. Techniques such as amplitude tapering, parasitic loading, and multilayer integration have proven effective in optimizing radiation performance while maintaining manufacturability for automotive and high-frequency applications.

Despite these advances, several limitations remain in the published series-fed arrays. These include relatively narrow impedance bandwidth, limited SLL control without multilayer feed networks, and challenges in achieving low-cost single-layer fabrication. Table 6 provides a comparative summary of the key characteristics of the reviewed arrays. To overcome these constraints, alternative fabrication platforms such as the Millimetric-Nanowire-Membrane (MnM) technology are employed, enabling low-cost processing and vertically integrated interconnects suitable for compact series-fed architectures.

Table 1. Comparison table of series-fed microstrip antennas in millimetre waves.

Ref.	**Substract** (ϵ_r, h [mm])	**Array Archit.**	**Array Size [λ^3]** ($\lambda = c/f$)	**f [GHz]**	**BW [%]**	**SLL [dB]**	**Peak Gain [dBi]**	**Ampl. Distrib.**
(Lee et al., 2024)	Rogers RO4830 (3.23, 0.125)	3x1	$7.04 \times 1.412 \times 0.125\lambda^3$	62.5	5.78	-8	10.24	Uniform
(Kang; Noh; Kim, 2020)	Rogers 3003C (3.16, 0.127)	8	$4.11 \times 0.45 \times 0.127\lambda^3$	76.5	3.92	-17	13.8	Dolph-Tschebyshev
(Tan et al., 2020)	Rogers R03003 (3.0, 0.127)	10	$22.24 \times 1.4 \times 0.127\lambda^3$	77	2.5	-23.5	16.2	Binomial
(Tan et al., 2022)	Rogers R03003 (3.0, 0.127)	10x6	$23.63 \times 1.4 \times 0.127\lambda^3$	79	3	-24	21	Binomial
(Liu; Bai; Yagoub, 2020)	Rogers R05880 (2.2, 0.127)	8x6	$31 \times 21 \times 0.407\lambda^3$	79	4.14	-19	22	Non-Uniform
(Chong; Wenbin, 2012)	Rogers R05880 (2.2, 0.127)	20x16	$39.5 \times 1. \times 0.127\lambda^3$	76	4	-17	29	Taylor
(Kashino; Uno; Sato, 2014)	Rogers R04830 (3.3, 0.388)	12x8	$29.05 \times 6 \times 0.388\lambda^3$	79	4	-15	21.5	Taylor
(Dash; Sarkar; Antar, 2023)	Rogers R03003 (3.0, 0.25)	11x3	$28.27 \times 7.55 \times 0.25\lambda^3$	79	3	-22	13.1	Binomial
(Oh; Oh, 2023)	Rogers RO4350 (2.98, 0.13)	4	$3.41 \times 1.59 \times 0.13\lambda^3$	140	11.5	TX -18 / -10	11.8	Uniform
(Xu et al., 2023)	Quartz Glass (3.78, 0.003)	9	$4.17 \times 0.7 \times 0.127\lambda^3$	60	4.18	-20	9.1	Dolph-Tschebyshev
(Mohan et al., 2023)	Rogers 4350B (3.66, 0.168)	3	$2.558 \times 1.25 \times 0.168\lambda^3$	80	10	N/A	13.73	Dolph-
(Aliakbari et al., 2022)	Any-Layer PCB (3.26, 0.16)	10	$22.5 \times 2.15 \times 0.168\lambda^3$	79	7.6	-13	12.7	Dolph-Tschebyshev
(Xu et al., 2017)	Taconic TLY-5 (2.2, 0.254)	10x6	$27.6 \times 1.6 \times 0.168\lambda^3$	77	5	-15	20	Binomial
(Li; Matos; Ghalichechian, 2021)	CLTE-XT (2.94, 0.254)	5x5	$15 \times 15 \times 0.254\lambda^3$	60	3.6	-10	18.7	Uniform
(Govindarajulu; Hokayem; Alwan, 2021)	Isola Tachyon (3.02, 0.13)	4	$9.6 \times 2.8 \times 0.568\lambda^3$	60	5.7	-14	10.51	Uniform

Source: Prepared by the author, 2025

1.3 Objectives

The primary objective of this work is the development of broadband series-fed microstrip antenna arrays operating at 60 GHz and 79 GHz, with particular emphasis on SLL reduction through amplitude tapering techniques.

The specific objectives are as follows:

1. Design a uniform series-fed array operating at 60 GHz with broadband behavior. This study will investigate various design parameters, including the number of elements, the dimensions of the QWT impedance matcher, and the width of the inter-element feed lines, aiming to optimize bandwidth performance.
2. Extend the design methodology to the 79 GHz band and implement amplitude tapering techniques to reduce SLL, improving radiation pattern performance.
3. Evaluate the Metallic Nanowire Membrane (MnM) fabrication technique to assess its impact on the electromagnetic performance and practical feasibility of the proposed arrays.

All antennas presented in this work were fabricated at the Millimeter-Wave Laboratory of Poli-USP, under the supervision of Professors Gustavo Pamplona Rehder and Ariana Serrano. The experimental characterization of the prototypes was also conducted at the same facility.

1.4 Work Organization

This thesis is organized into four chapters. Chapter 1 provides a contextual overview of the current state of wireless technology, emphasizing the growing demand for higher frequency bands to support increased data throughput. Key challenges in the development of devices suitable for mmWave operation are identified. A focused literature review highlights primary technologies and substrate materials used in the fabrication of series-fed antenna arrays for mmWave applications, with particular attention to techniques for side-lobe level suppression.

Chapter 2, *Design and Fabrication Methods*, presents the theoretical background required for the design of antenna arrays in the target frequency bands. Fundamental electromagnetic principles are reviewed, and the calculations necessary for determining array dimensions are detailed. Established methods for reducing unwanted side-lobe radiation, including amplitude tapering techniques, are also discussed. This chapter also introduces the fabrication strategies employed, including conventional PCB and MnM approaches.

Chapter 3, *Numerical and Experimental Results*, describes the antenna geometries, starting with the design of a single rectangular microstrip patch element and extending to arrays of two, four, and eight elements. The simulation procedures and parametric analyses are performed using Ansys HFSS electromagnetic simulation software. Fabrication considerations and the experimental setup for antenna parameter measurements are also summarized. The chapter presents the analysis and discussion of the main results, highlighting the electromagnetic performance characteristics observed for the antenna arrays. The impact of parametric variations on the optimized array designs is examined, and the effectiveness of the Dolph–Chebyshev amplitude distribution technique for SLL reduction is demonstrated.

Chapter 4, *Conclusions*, summarizes the main contributions of this work and outlines potential directions for future research. It reflects on the employed methodologies, design trade-offs, and the key challenges addressed through the proposed approaches.

2 Design and Fabrication Methods

This chapter presents the design methodologies and fabrication approaches employed in the development of high-performance antenna arrays for millimeter-wave applications. The discussion begins with the analysis of linear antenna arrays, emphasizing the array factor and a variety of amplitude distributions, including uniform, Dolph–Chebyshev, triangular, Hamming, binomial, and Blackman, followed by a comparative evaluation of their radiation characteristics. The design of the rectangular microstrip patch antenna is then introduced, covering the geometric formulation of the patch, the synthesis of microstrip feed lines, and impedance matching strategies such as the inset-feed technique and the QWT. Subsequently, the focus shifts to series-fed microstrip antenna arrays, where the trade-offs between parallel- and series-fed configurations are examined, as well as the distinction between traveling-wave and resonant implementations, leading to the design principles of resonant series-fed arrays. Finally, the chapter details the fabrication process based on Metallic Nanowire Membrane (MnM) technology, highlighting its potential to enable low-cost, compact, and high-efficiency structures suitable for operation at millimeter-wave frequencies.

2.1 Linear Antenna Array

Linear antenna arrays are cornerstone structures in antenna design, enabling high directivity, beam steering, and tailored radiation patterns for applications such as wireless communications, radar systems, and satellite links (Balanis, 2016). These arrays consist of multiple radiating elements arranged along a straight line, with their combined radiation pattern governed by the array factor, which is determined by element spacing, amplitude distribution, and phase excitation. In the context of series-fed microstrip patch antenna arrays, the linear configuration offers simplicity, compact design, and compatibility with planar fabrication techniques, making it particularly suitable for high-frequency applications (James; Hall, 1989).

The theory of antenna arrays is based on the principle of superposition, where the total far-field radiation pattern results from the combined contributions of individual element patterns modified by the array factor (Balanis, 2016). For a linear array of N identical elements, the far-zone electric field E_{total} at a point in space is given by the product of the field of a single element, evaluated at a reference point (typically the origin), and the array factor of the array. Mathematically, this is expressed as:

$$E_{\mathrm{total}}(\vartheta) = E_{\mathrm{elem}}(\vartheta) \times \mathrm{AF}(\vartheta), \tag{2.1}$$

Figure 3. Linear array with N elements.

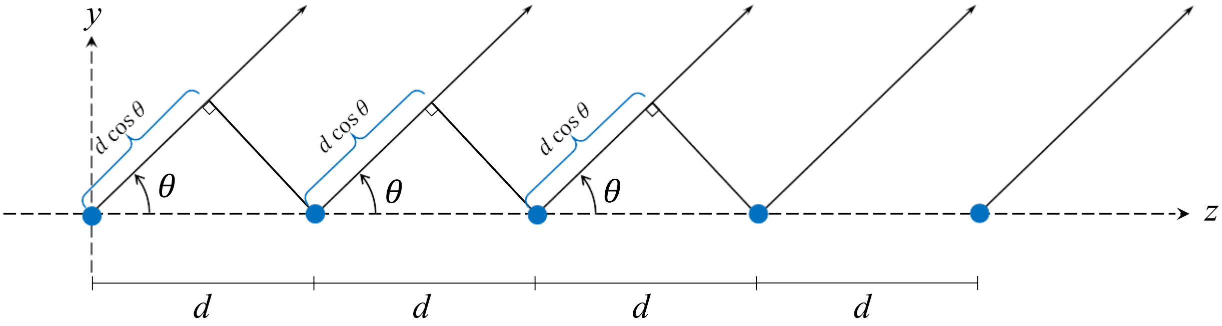

Source: (Balanis, 2016)

where $E_{\text{elem}}(\vartheta)$ is the electric field pattern of a single element at the reference point, and AF(ϑ) is the array factor, which accounts for the phase and amplitude contributions of all elements. For a linear array along the z-axis (see Fig. 3) with elements spaced by distance d, the array factor is:

$$\mathrm{AF}(\vartheta) = a_0 e^{j0(kd\cos\vartheta+\beta)} + a_1 e^{j1(kd\cos\vartheta+\beta)} + a_2 e^{j2(kd\cos\vartheta+\beta)} + \cdots + a_{N-1} e^{j(N-1)(kd\cos\vartheta+\beta)}. \quad (2.2)$$

where $k = 2\pi/\lambda$ is the free-space wave-number, ϑ is the angle from the array axis, and $e^{j0(kd\cos\vartheta+\beta)} = 1$. It can be expressed as

$$\mathrm{AF}(\vartheta) = \sum_{n=1}^{N} a_n e^{j(n-1)(kd\cos\vartheta+\beta)}, \quad (2.3)$$

which can be written as

$$\mathrm{AF}(\psi) = \sum_{n=1}^{N} a_n e^{j(n-1)\psi}. \quad (2.4)$$

where

$$\psi = kd\cos\vartheta + \beta. \quad (2.5)$$

The array factor determines key radiation characteristics, such as directivity, beamwidth, and SLL, which can be controlled by adjusting the excitation coefficients a_n and spacing d.

The analysis of linear antenna arrays relies on several simplifying assumptions to facilitate mathematical modeling and design:

- **Negligible Mutual Coupling**: Mutual coupling between elements is neglected to focus on the array factor's contribution to the radiation pattern. In practice, coupling affects impedance and pattern, requiring full-wave simulations (Balanis, 2016).

- **Uniform Spacing**: Elements are equally spaced, typically at $d = \lambda/2$ or $\lambda_g/2$ (guided wavelength in microstrip arrays), to achieve broadside radiation without grating lobes (Balanis, 2016).

- **Linear Array Geometry**: The elements are aligned along a straight line, ensuring a symmetric radiation pattern in the plane perpendicular to the array axis (Balanis, 2016).

These assumptions enable a tractable analysis of the array factor and radiation characteristics, as explored in the following subsections, while acknowledging that practical designs may require adjustments for non-ideal effects.

2.1.1 Array Factor

The array factor is a key concept in antenna array design, governing the radiation pattern through the number of elements, their linear arrangement, excitation amplitudes, phases, and inter-element spacings (Balanis, 2016, Ch. 6). For a linear array, it shapes critical characteristics such as directivity, main lobe width, and side-lobe levels, independently of individual element patterns. To simplify analysis, elements are modeled as isotropic point sources ($E_{\text{single}}(\vartheta) = 1$), allowing the total far-field pattern to be expressed solely by the array factor. This isolates the effects of array geometry and excitation, providing a clear framework for studying amplitude and phase distributions.

For a linear array of N identical elements along the z-axis with uniform spacing d, $\beta = 0$, the array factor is

$$AF(\vartheta) = \sum_{n=1}^{N} a_n e^{j(n-1)kd\cos\vartheta}. \tag{2.6}$$

By adjusting a_n, the radiation pattern can be tailored to enhance directivity or reduce side-lobe levels. This study examines uniform and non-uniform amplitude distributions in series-fed microstrip arrays with spacing $d = \lambda/2$. Uniform distributions ($a_n = 1$) offer high directivity but yield side-lobe levels for broadside arrays. Non-uniform distributions, such as Dolph-Tschebyshev, enable precise side-lobe control by varying a_n, trading some directivity for lower side-lobes, which is critical for applications like radar and wireless communications. The analysis explores six amplitude distributions—Uniform, Dolph-Tschebyshev (with side-lobe levels of 20 dB, 30 dB, and 40 dB), Triangular, Hamming, Binomial, and Blackman—through mathematical formulations, amplitude visualizations, and performance comparisons to provide insights into optimizing array designs for specific system requirements.

For a linear array consisting of an even number of isotropic elements, $2M$, uniformly spaced by a distance d along the z-axis and symmetrically positioned with respect to the origin (as illustrated in Fig. 4), the array factor (AF) for a broadside array ($\beta = 0$) can be written explicitly as

Figure 4. Non-uniform amplitude array with even number of elements.

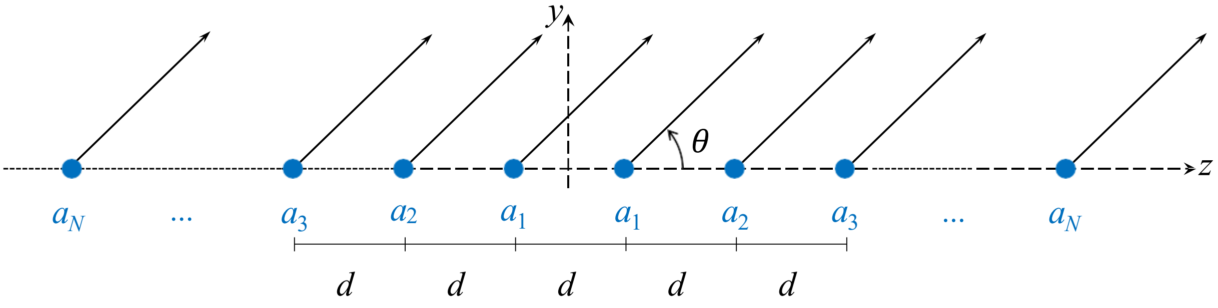

Source: (Balanis, 2016)

Figure 5. Non-uniform amplitude array with odd number of elements.

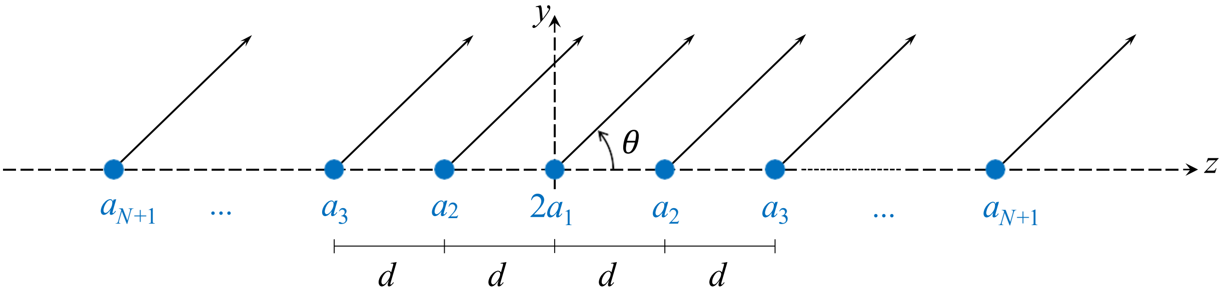

Source: (Balanis, 2016)

$$\begin{aligned}(\mathrm{AF})_{2N}(\vartheta) &= a_1 e^{j\frac{1}{2}kd\cos\vartheta} + a_2 e^{j\frac{3}{2}kd\cos\vartheta} + \cdots + a_M e^{j\frac{2N-1}{2}kd\cos\vartheta} \\ &+ a_1 e^{-j\frac{1}{2}kd\cos\vartheta} + a_2 e^{-j\frac{3}{2}kd\cos\vartheta} + \cdots + a_M e^{-j\frac{2N-1}{2}kd\cos\vartheta}.\end{aligned} \tag{2.7}$$

Defining the phase term

$$\psi = kd\cos\vartheta, \tag{2.8}$$

the expression in (2.7) can be written in compact summation form as

$$(\mathrm{AF})_{2N}(\vartheta) = \sum_{n=1}^{N} a_n \left[e^{j\left(n-\frac{1}{2}\right)\psi} + e^{-j\left(n-\frac{1}{2}\right)\psi} \right]. \tag{2.9}$$

Applying Euler's formula,

$$e^{jx} + e^{-jx} = 2\cos(x)$$

the array factor becomes

$$\mathrm{AF}_{2N}(\vartheta)_{2N} = 2\sum_{n=1}^{N} a_n \cos\left[\left(n-\frac{1}{2}\right)\psi\right]. \tag{2.10}$$

The normalized form of the array factor is expressed as

$$\mathrm{AF}_{2N}(\vartheta) = \sum_{n=1}^{N} a_n \cos\left[\left(n-\frac{1}{2}\right)\psi\right]. \tag{2.11}$$

Now consider a linear array consisting of an odd number of isotropic elements, $2N+1$ (where N is an integer), uniformly spaced by a distance d along the z-axis and symmetrically positioned with respect to the origin, the array factor (AF) for a broadside array ($\beta = 0$) can be explicitly expressed as

$$\begin{aligned}\mathrm{AF}_{2N+1}(\vartheta) = 2a_1 + a_2 e^{jkd\cos\vartheta} + a_3 e^{j2kd\cos\vartheta} + \cdots + a_{N+1} e^{jNkd\cos\vartheta} \\ + a_2 e^{-jkd\cos\vartheta} + a_3 e^{-j2kd\cos\vartheta} + \cdots + a_{N+1} e^{-jNkd\cos\vartheta}\end{aligned} \tag{2.12}$$

Defining the phase term

$$\psi = kd\cos\vartheta \tag{2.13}$$

the array factor in (2.12) can be rewritten in compact summation form as

$$\mathrm{AF}_{2N+1}(\vartheta) = 2a_1 + \sum_{n=2}^{N+1} a_n \left[e^{j(n-1)\psi} + e^{-j(n-1)\psi} \right]. \tag{2.14}$$

Applying Euler's identity,

$$e^{jx} + e^{-jx} = 2\cos(x),$$

the array factor simplifies to

$$\mathrm{AF}_{2N+1}(\vartheta) = 2\sum_{n=1}^{N+1} a_n \cos\left[(n-1)\psi\right]. \tag{2.15}$$

The normalized form of the array factor is expressed as

$$\mathrm{AF}_{2N+1}(\vartheta) = \sum_{n=1}^{N+1} a_n \cos\left[(n-1)\psi\right]. \tag{2.16}$$

Equations (2.10) and (2.16) represent the array factor for linear arrays with an even ($2N$) and odd ($2N+1$) number of isotropic elements, respectively. In both cases, the elements are uniformly spaced and symmetrically positioned with respect to the origin, assuming symmetric amplitude excitation. The cosine-based formulation is particularly convenient for array synthesis, as it allows straightforward control of radiation characteristics, such as SLL and beamwidth, through appropriate selection of the excitation coefficients a_n. The next step is to determine these coefficients according to the desired radiation pattern specifications.

The SLL is used as a key metric to evaluate the performance of different amplitude distributions. In this work, the SLL is defined as the ratio between the maximum magnitude of the first side-lobe and the main-lobe peak, expressed in decibels (dB). Mathematically, it is calculated as

$$\mathrm{SLL} = 20\log_{10}\left(\frac{|\mathrm{AF}|_{\text{side-lobe}}^{\max}}{|\mathrm{AF}|_{\text{main-lobe}}^{\max}}\right) \quad [\mathrm{dB}], \tag{2.17}$$

where $|\mathrm{AF}|_{\text{side-lobe}}^{\max}$ is the highest side-lobe magnitude and $|\mathrm{AF}|_{\text{main-lobe}}^{\max}$ is the peak of the main lobe. This definition ensures a consistent basis for comparing the effectiveness of different excitation schemes in side-lobe suppression.

The directivity of an antenna is defined as the ratio between the maximum radiation intensity in the main beam direction and the average radiation intensity over all directions, assuming an isotropic radiator as reference. Mathematically, the directivity D is given by

$$D_{\max} = \frac{U_{\max}}{U_{\text{avg}}} = \frac{4\pi U_{\max}}{P_{\text{rad}}}, \tag{2.18}$$

where $U_{\max}$ is the maximum radiation intensity, U_{avg} is the average radiation intensity over the sphere, and P_{rad} is the total radiated power by the antenna.

For a broadside linear array of isotropic elements, the radiation intensity at an angle ϑ is proportional to the squared magnitude of the array factor (AF), i.e.,

$$U(\vartheta) = C\,|\mathrm{AF}(\vartheta)|^2, \tag{2.19}$$

where C is a constant related to the total power and element gain.

The total radiated power is obtained by integrating the radiation intensity over all directions, considering azimuthal symmetry:

$$P_{\text{rad}} = \int_0^{2\pi}\int_0^{\pi} U(\vartheta)\sin\vartheta\, d\vartheta\, d\phi. \tag{2.20}$$

Since the array is linear and symmetric about the z-axis, the radiation pattern is independent of ϕ, and the integral over ϕ yields a factor of 2π. Thus,

$$P_{\text{rad}} = 2\pi\int_0^{\pi} U(\vartheta)\sin\vartheta\, d\vartheta = 2\pi C\int_0^{\pi} |\mathrm{AF}(\vartheta)|^2 \sin\vartheta\, d\vartheta. \tag{2.21}$$

In the main beam direction (broadside), $\vartheta = \pi/2$, the array factor achieves its maximum value:

$$\mathrm{AF}_{\max} = \left|\sum_{n=1}^{N} a_n\right|.$$

Therefore, the maximum radiation intensity is

$$U_{\max} = C\left|\sum_{n=1}^{N} a_n\right|^2. \tag{2.22}$$

Substituting (2.22) and (2.21) into (2.18) yields

$$D_{\max} = \frac{4\pi C\left|\sum_{n=1}^{N} a_n\right|^2}{2\pi C\int_0^{\pi} |\mathrm{AF}(\vartheta)|^2 \sin\vartheta\, d\vartheta} = \frac{2\left|\sum_{n=1}^{N} a_n\right|^2}{\int_0^{\pi} |\mathrm{AF}(\vartheta)|^2 \sin\vartheta\, d\vartheta}. \tag{2.23}$$

Thus, the directivity of the broadside linear array is given by

$$D_{\max} = \frac{2\left|\sum_{n=1}^{N} a_n\right|^2}{\int_0^{\pi} |\mathrm{AF}(\vartheta)|^2 \sin\vartheta\, d\vartheta}. \tag{2.24}$$

The integral is evaluated numerically using adaptive quadrature methods to ensure accurate computation across varying radiation patterns. This formulation provides a quantitative measure of how effectively the array concentrates energy in the desired direction. This chapter analyzes a broadside array ($N = 8$, $d = \lambda/2$) with several amplitude distributions, including Uniform, Dolph-Chebyshev (with side-lobe attenuation levels of $R_0 = 20$, 30, and 40 dB), Triangular, Hamming, Binomial, and Blackman. Each distribution is examined through detailed mathematical derivations, amplitude coefficient visualization, array factor plots, and comprehensive performance analysis in terms of SLL and directivity (D).

2.1.2 Uniform Distribution

The uniform distribution assigns equal amplitude to all elements, maximizing directivity but producing high side-lobes (Balanis, 2016). For $N = 8$, the amplitude coefficients are:

$$a_n = 1, \quad n = 1, \ldots, 8, \tag{2.25}$$

normalized as

$$a_n = [1,\ 1,\ 1,\ 1,\ 1,\ 1,\ 1,\ 1]. \tag{2.26}$$

The array factor simplifies to:

$$\mathrm{AF}(\vartheta) = \frac{\sin\left(\frac{Nkd\cos\vartheta}{2}\right)}{\sin\left(\frac{kd\cos\vartheta}{2}\right)}, \tag{2.27}$$

with $kd = \pi$ for $d = \lambda/2$. This yields a sinc-like pattern with a narrow main beam and side-lobes at approximately −13.2 dB. The amplitude distribution, shown in Fig. 6, is constant, reflecting equal excitation across elements.

The array factor, depicted in Fig. 7, has an HPBW of 10.26° and directivity of 9.03 dB. The uniform distribution serves as a baseline for comparing tapered distributions, which sacrifice directivity for side-lobe suppression (Balanis, 2016).

2.1.3 Dolph-Chebyshev Distribution

The Dolph-Chebyshev distribution uses Chebyshev polynomials to achieve a specified side-lobe level with minimal beamwidth (Dolph, 1946). For 8 elements ($N = 4$), we analyze cases with side-lobe levels $R_0 = 20, 30, 40$ dB. The array factor is given by (2.11),

Figure 6. Normalized amplitude distribution for uniform distribution ($N = 8$).

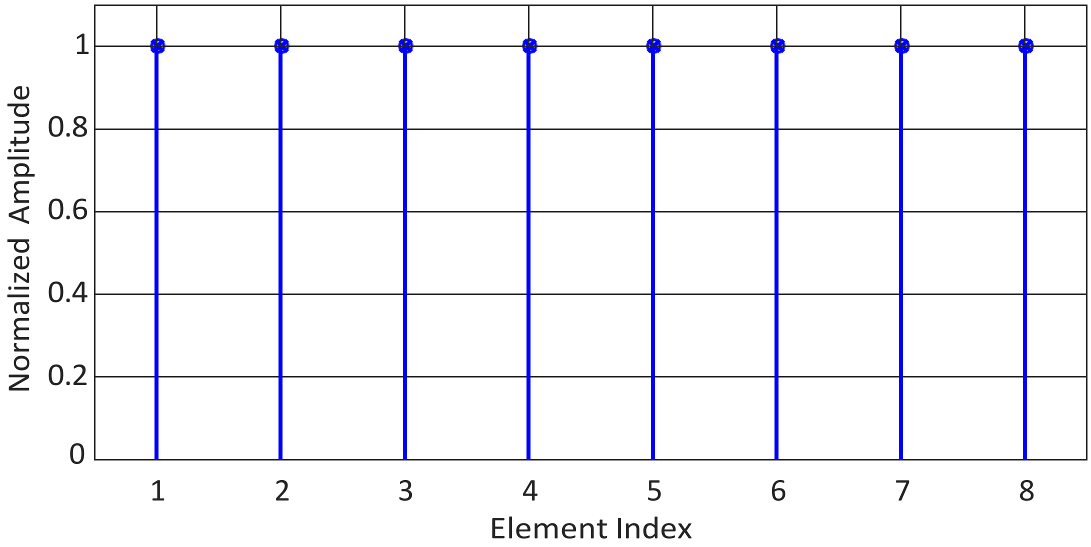

Source: Prepared by the author, 2025.

Figure 7. Normalized array factor (dB) for uniform distribution ($N = 8$, $d = \lambda/2$).

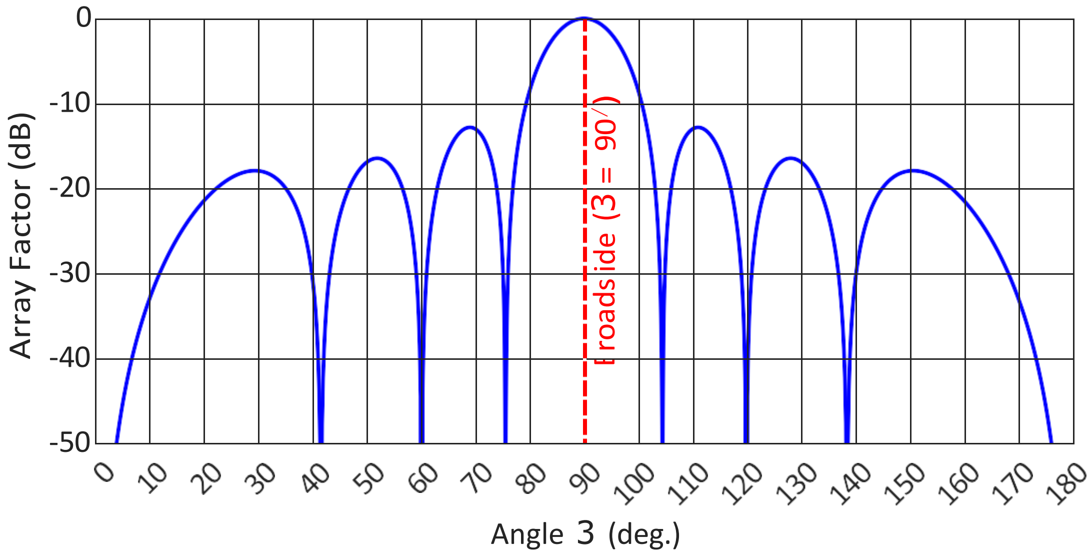

Source: Prepared by the author, 2025.

in this case, is

$$(\mathrm{AF})_{2N} = \sum_{n=1}^{N=4} = a_n \cos[(2n-1)\psi] \tag{2.28}$$

where

$$\psi = \frac{2\pi d}{\lambda}\cos\vartheta\Big|_{d=\lambda/2} = \pi\cos\vartheta \tag{2.29}$$

For $N = 4$, when expanded, the array factor can be written as

$$(\mathrm{AF})_8 = a_1\cos(\psi) + a_2\cos(3\psi) + a_3\cos(5\psi) + a_4\cos(7\psi). \tag{2.30}$$

Each cosine term whose argument is an integer multiple of a fundamental frequency ψ can be expressed as a polynomial function. This transformation relies on well-known trigonometric identities. Specifically, any function of the form $\cos(m\psi)$, where m is a non-negative integer, can be rewritten as a polynomial of $\cos(\psi)$. The polynomial expansions for m for 1, 3, 5 and 7 are given by (Balanis, 2016):

$$\begin{aligned} m = 1 :&\quad \cos(m\psi) = \cos\psi \\ m = 3 :&\quad \cos(3\psi) = 4\cos^3\psi - 3\cos\psi \\ m = 5 :&\quad \cos(5\psi) = 16\cos^5\psi - 20\cos^3\psi + 5\cos\psi \\ m = 7 :&\quad \cos(7\psi) = 64\cos^7\psi - 112\cos^5\psi + 56\cos^3\psi - 7\cos\psi. \end{aligned} \tag{2.31}$$

To simplify the notation, we define

$$z = \cos\psi. \tag{2.32}$$

Substituting this into the previous expressions, the cosine terms can be written as polynomials in z

$$\begin{aligned} T_1(z) &= z \\ T_3(z) &= 4z^3 - 3z \\ T_5(z) &= 16z^5 - 20z^3 + 5z \\ T_7(z) &= 64z^7 - 112z^5 + 56z^3 - 7z. \end{aligned} \tag{2.33}$$

These the Chebyshev polynomials of the first kind, denoted as $T_m(z)$, which are widely used in approximation theory and array synthesis due to their mini-max property that leads to equal-ripple behavior in side-lobe levels. The polynomials are illustrated in Fig. 8. Note that, for an N -element Dolph-Chebyshev array, the Chebyshev polynomial $T_{N-1}(z)$ of order $m = N - 1$ is used. The recurrence relation is given by:

$$T_m(z) = 2zT_{m-1}(z) - T_{m-2}(z), \tag{2.34}$$

with the initial conditions $T_0(z) = 1$ and $T_1(z) = z$. Each polynomial can also be computed using

$$T_m(z) = \begin{cases} \cos\left(m\cos^{-1}(z)\right), & \text{for } -1 \le z \le +1 \\ \cosh\left(m\cosh^{-1}(z)\right), & \text{for } z < -1 \text{ or } z > +1 \end{cases} \tag{2.35}$$

The Chebyshev polynomials—depicted in Fig. 8 for $m = 1, 3, 5,$ and 7— used in the design of Dolph-Chebyshev arrays exhibit the following key properties within the interval $-1 \le z \le 1$:

1. All polynomials, regardless of order, pass through the point $(1, 1)$. This means that for any order m, $T_m(1) = 1$ (see Fig. 8).

Figure 8. Chebyshev polynomials.

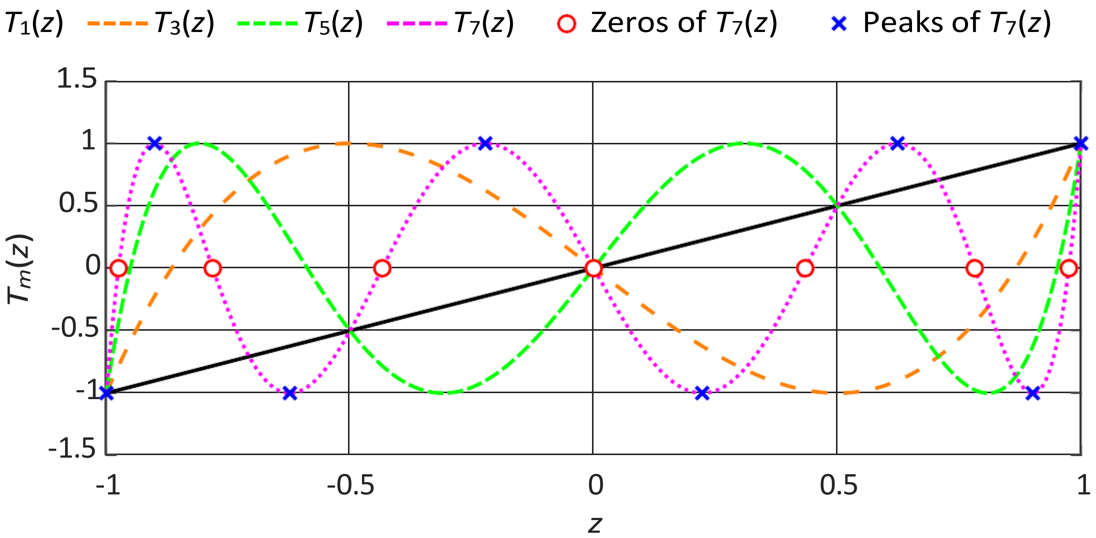

Source: Prepared by the author, 2025.

2. Within the range $-1 \leq z \leq 1$, the polynomials have values bounded between -1 and $+1$, i.e., $|T_m(z)| \leq 1$. This oscillatory behavior is critical for controlling the side lobe levels in antenna array patterns.
3. For a Chebyshev polynomial of order m, $T_m(z)$ has exactly m roots, all located within the interval $-1 \leq z \leq 1$. Additionally, the polynomial exhibits exactly $m+1$ extrema (maxima and minima) within this interval, alternating between $+1$ and -1. This behavior guarantees a uniform ripple amplitude in the oscillatory region, which is a key characteristic of Chebyshev functions.

By substituting the cosine terms using (2.31) and the corresponding Chebyshev polynomial expansions from (2.33), the array factor in (2.30) is reformulated as

$$\begin{aligned}(\mathrm{AF})_8 = a_1 z & \\ + a_2 & \left(4z^3 - 3z\right) \\ + a_3 & \left(16z^5 - 20z^3 + 5z\right) \\ + a_4 & \left(64z^7 - 112z^5 + 56z^3 - 7z\right).\end{aligned} \tag{2.36}$$

Grouping by powers of z, the array factor becomes

$$\begin{aligned}(\mathrm{AF})_8 = {} & (64a_4)z^7 \\ & + (16a_3 - 112a_4)z^5 \\ & + (4a_2 - 20a_3 + 56a_4)z^3 \\ & + (a_1 - 3a_2 + 5a_3 - 7a_4)z.\end{aligned} \tag{2.37}$$

This transformation expresses the array factor as a polynomial in z, where $z = \cos\psi = \cos(\pi \cos\vartheta)$. As ϑ varies from 0 to π, the variable ψ ranges from $+\pi$ to $-\pi$, and z spans the interval from -1 to 1. This mapping enables the formulation of the array factor in terms of the Chebyshev polynomial $T_7(z)$.

The primary objective of the Dolph–Chebyshev synthesis is to design an array radiation pattern in which the main-lobe exhibits a normalized amplitude of unity, while all side-lobes are constrained to have equal amplitudes defined by $1/R_0$, where R_0 is the main-to-side-lobe voltage ratio. To achieve this characteristic response, the array factor (AF) must be shaped to follow the behavior of a single Chebyshev polynomial, specifically $T_{N-1}(z)$, appropriately mapped through a scaling transformation. This approach contrasts with traditional polynomial expansions that employ linear combinations of multiple terms, such as

$$(\mathrm{AF})_8 = a_1T_1(z) + a_2T_3(z) + a_3T_5(z) + a_4T_7(z) \tag{2.38}$$

In the case of an eight-element array, the synthesis employs the polynomial $T_7(z)$, since the order of the polynomial is defined as $m = N - 1 = 7$.

Instead, the coefficients a_n are chosen such that the array factor is proportional to $T_7\left(\frac{z}{z_0}\right)$, where z_0 is a scaling parameter that controls the SLL. The procedure is detailed as follows.

a) Substitution $\cos\psi = \frac{z}{z_0}$*:* To align the AF with $T_7(z)$, the following substitution is applied (Balanis, 2016):

$$\cos\psi = \frac{z}{z_0} \tag{2.39}$$

or equivalently,

$$z = z_0 \cos\psi \tag{2.40}$$

This substitution rewrites the AF, originally expressed as a function of $\cos\psi$, in terms of $\frac{z}{z_0}$. Each cosine term of the form $\cos[(2n - 1)\psi]$ in the AF is replaced by its corresponding Chebyshev polynomial expansion. For example:

$$\cos(\psi) = \frac{z}{z_0} \tag{2.41}$$

$$\cos(3\psi) = T_3\left(\frac{z}{z_0}\right) = 4\left(\frac{z}{z_0}\right)^3 - 3\left(\frac{z}{z_0}\right) \tag{2.42}$$

$$\cos(5\psi) = T_5\left(\frac{z}{z_0}\right) \tag{2.43}$$

$$\cos(7\psi) = T_7\left(\frac{z}{z_0}\right) \tag{2.44}$$

Accordingly, the expanded AF for an eight-element array becomes:

$$\begin{aligned}\mathrm{AF}_8 = {} & a_1 \frac{z}{z_o} + a_2 \left[4\left(\frac{z}{z_o}\right)^3 - 3\left(\frac{z}{z_o}\right) \right] \\ & + a_3 \left[16\left(\frac{z}{z_o}\right)^5 - 20\left(\frac{z}{z_o}\right)^3 + 5\left(\frac{z}{z_o}\right) \right] \\ & + a_4 \left[64\left(\frac{z}{z_o}\right)^7 - 112\left(\frac{z}{z_o}\right)^5 + 56\left(\frac{z}{z_o}\right)^3 - 7\left(\frac{z}{z_o}\right) \right] \end{aligned} \tag{2.45}$$

Grouping terms by powers of z, the AF expression simplifies to:

$$\begin{aligned}\mathrm{AF}_8 = {} & \frac{z}{z_o}(a_1 - 3a_2 + 5a_3 - 7a_4) \\ & + \frac{z^3}{z_o^3}(4a_2 - 20a_3 + 56a_4) \\ & + \frac{z^5}{z_o^5}(16a_3 - 112a_4) \\ & + \frac{z^7}{z_o^7}(64a_4) \end{aligned} \tag{2.46}$$

b) Matching with $T_7(z)$: The key step is to equate this AF to the Chebyshev polynomial $T_7(z)$, which is defined as:

$$T_7(z) = 64z^7 - 112z^5 + 56z^3 - 7z \tag{2.47}$$

By matching the coefficients of the corresponding powers of z, the following system of equations is obtained:

$$\frac{64a_4}{z_o^7} = 64 \quad \Longrightarrow \quad a_4 = z_o^7, \tag{2.48}$$

$$\frac{16a_3 - 112a_4}{z_o^5} = -112 \quad \Longrightarrow \quad a_3 = 7(z_o^7 - z_o^5), \tag{2.49}$$

$$\frac{4a_2 - 20a_3 + 56a_4}{z_o^3} = 56 \quad \Longrightarrow \quad a_2 = 14z_o^3 + 21z_o^7 - 35z_o^5, \tag{2.50}$$

$$\frac{a_1 - 3a_2 + 5a_3 - 7a_4}{z_o} = -7 \quad \Longrightarrow \quad a_1 = -7z_o + 42z_o^3 - 70z_o^5 + 35z_o^7. \tag{2.51}$$

This procedure guarantees that:

$$\mathrm{AF}_8 = T_7\left(\frac{z}{z_o}\right) \tag{2.52}$$

Thus, the array factor is not represented as an arbitrary linear combination of the Chebyshev polynomials $T_1(z)$, $T_3(z)$, $T_5(z)$, and $T_7(z)$, but rather as the scaled Chebyshev polynomial $T_7\left(\frac{z}{z_o}\right)$, with the coefficients a_n specifically determined to satisfy this equality.

An important observation is that the parameter z_o directly controls the SLL of the array. This parameter is defined by the condition

$$T_7(z_o) = R_o, \tag{2.53}$$

where R_o is the voltage ratio between the main lobe and the side-lobes. The desired SLL, expressed in decibels, determines R_o according to

$$R_o = 10^{\frac{\text{SLL (dB)}}{20}}. \tag{2.54}$$

For SLL specifications of −20 dB, −30 dB, and −40 dB, the corresponding values of R_o are 10, 31.6228, and 100, respectively. The scale factor z_o is given by

$$z_o = \frac{1}{2}\left[\left(R_o + \sqrt{R_o^2 - 1}\right)^{1/P} + \left(R_o - \sqrt{R_o^2 - 1}\right)^{1/P}\right]. \tag{2.55}$$

where P is an integer equal to one less than the number of array elements. For the present case (P = 7), that is.

$$z_o = \frac{1}{2}\left[\left(R_o + \sqrt{R_o^2 - 1}\right)^{1/7} + \left(R_o - \sqrt{R_o^2 - 1}\right)^{1/7}\right] \tag{2.56}$$

and

$$z_o = \frac{1}{2}\left[\left(10 + \sqrt{10^2 - 1}\right)^{1/7} + \left(10 - \sqrt{10^2 - 1}\right)^{1/7}\right] = 1.0928, \tag{2.57}$$

$$z_o = \frac{1}{2}\left[\left(31.6228 + \sqrt{31.6228^2 - 1}\right)^{1/7} + \left(31.6228 - \sqrt{31.6228^2 - 1}\right)^{1/7}\right] = 1.1807, \tag{2.58}$$

$$z_o = \frac{1}{2}\left[\left(100 + \sqrt{100^2 - 1}\right)^{1/7} + \left(100 - \sqrt{100^2 - 1}\right)^{1/7}\right] = 1.3004. \tag{2.59}$$

The parameter z_o defines the point where $T_7(z)$ reaches the main lobe amplitude. The side lobes are mapped to the region $-1 \leq z \leq z_1$, where $z_1 \approx 0.9749$ is the root of $T_7(z) = 0$ closest to $z = 1$. Solving:

$$64z^7 - 112z^5 + 56z^3 - 7z = 0 \implies z(64z^6 - 112z^4 + 56z^2 - 7) = 0 \tag{2.60}$$

The roots include $z = 0$ and those of the sixth-degree polynomial, with $z_1 \approx 0.9749$, defining the oscillatory region of $T_7(z)$. The normalized excitation coefficients are summarized in Table 2.

These coefficients ensure that the array factor is proportional to $T_7(z/z_o)$, achieving the specified SLLs. As R_o increases, the coefficients exhibit greater tapering, reducing side lobe levels at the cost of a wider main lobe, consistent with Dolph-Chebyshev array design principles (Balanis, 2016). Alternatively, one can use directly

$$a_i = \sum_{j=i}^{N/2} (-1)^{N/2-j} z_o^{2j-1} \frac{(j + N/2 - 2)!(2N/2 - 1)}{(j-i)!(j+i-1)!(N/2-j)!}. \tag{2.61}$$

Table 2. Normalized Excitation Coefficients for Dolph-Chebyshev Array (N = 8)

SLL (dB)	z_0	a_1	a_2	a_3	a_4
−20	1.0928	1	0.875120	0.660305	0.579902
−30	1.1807	1	0.811960	0.518747	0.262216
−40	1.3004	1	0.759446	0.417904	0.146097

Source: Prepared by the author, 2025.

Figure 9. Normalized amplitude distributions for Dolph-Chebyshev (R_0 = 20, 30, 40 dB, N = 8).

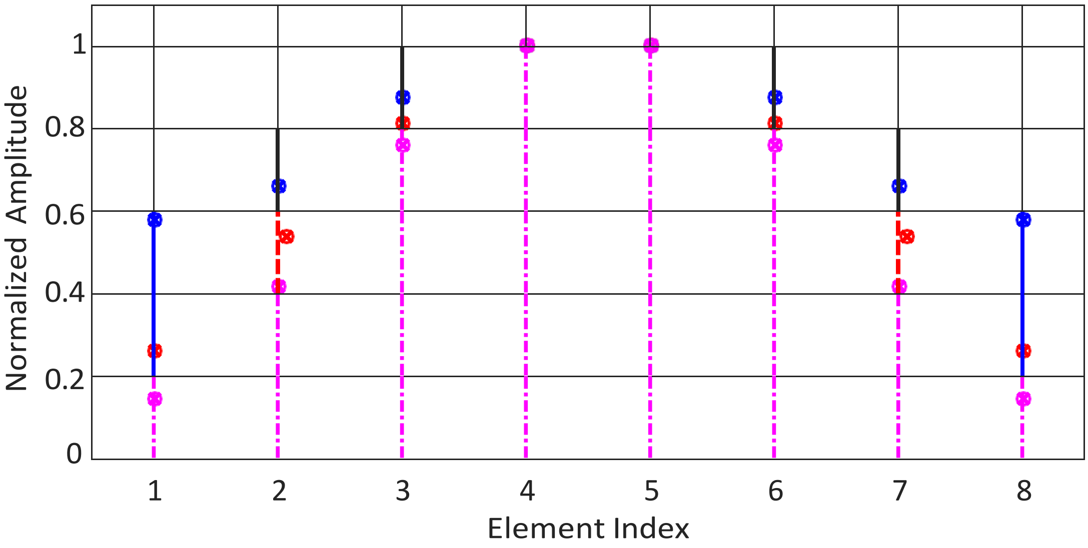

Source: Prepared by the author, 2025.

The combined amplitude distributions, shown in Fig. 9, illustrate increasing taper as R_0 rises, reducing edge amplitudes to suppress side-lobes.

The combined array factors, depicted in Fig. 10, confirm SLL at −20 dB, −30 dB, and −40 dB, with HPBWs of 11.02°, 12.49°, and 14.08°, and directivities of 8.92 dB, 8.65 dB, and 8.37 dB, respectively. Higher R_0 reduces side-lobes but widens the beam and lowers directivity, a trade-off critical for radar and satellite systems requiring low interference (Dolph, 1946).

Comparative analysis reveals that R_0 = 20 dB balances narrow beamwidth and moderate side-lobe suppression, suitable for 5G base stations. R_0 = 30 dB offers stronger interference rejection for radar, while R_0 = 40 dB prioritizes ultra-low side-lobes for satellite links, despite reduced directivity. Table 3 summarizes these metrics.

2.1.4 Triangular Distribution

The triangular distribution applies a linear taper to reduce side-lobes compared to the uniform case (Kraus; Marhefka, 2002). For N = 8, amplitudes are:

Figure 10. Normalized array factors (dB) for Dolph-Chebyshev (R_0 = 20, 30, 40 dB, N = 8, $d = \lambda/2$).

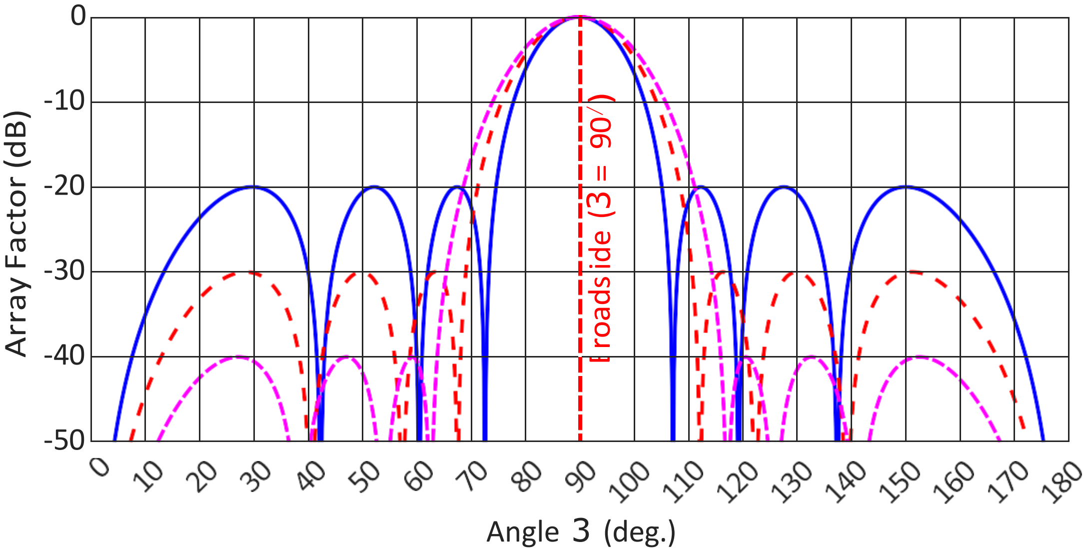

Source: Prepared by the author, 2025.

Table 3. Performance comparison of Dolph-Chebyshev distributions (N = 8, $d = \lambda/2$).

R_0 (dB)	Side-lobe Level (dB)	HPBW (deg.)	Directivity (dB)
20	-20.00	11.02	8.92
30	-29.98	12.49	8.65
40	-40.00	14.08	8.37

Source: Prepared by the author, 2025.

$$a_n = 1 - \frac{\left|n - \frac{N+1}{2}\right|}{\frac{N}{2}}, \quad n = 1, \ldots, 8, \tag{2.62}$$

yielding

$$a_n = [0.125,\ 0.375,\ 0.625,\ 0.875,\ 0.875,\ 0.625,\ 0.375,\ 0.125], \tag{2.63}$$

normalized as

$$a_n = [0.1429,\ 0.4286,\ 0.7143,\ 1.0000,\ 1.0000,\ 0.7143,\ 0.4286,\ 0.1429] \tag{2.64}$$

This linear decrease from the array center reduces side-lobes by concentrating energy in the main beam. The amplitude distribution is shown in Fig. 11.

The array factor, in Fig. 12, has a SLL of −26.4 dB, HPBW of 13.69°, and directivity of 8.35 dB. Compared to the uniform distribution, it offers significant side-lobe reduction with moderate beam broadening, making it suitable for general-purpose arrays in wireless communications where cost and simplicity are priorities (Kraus; Marhefka, 2002).

Figure 11. Normalized amplitude distribution for triangular distribution ($N = 8$).

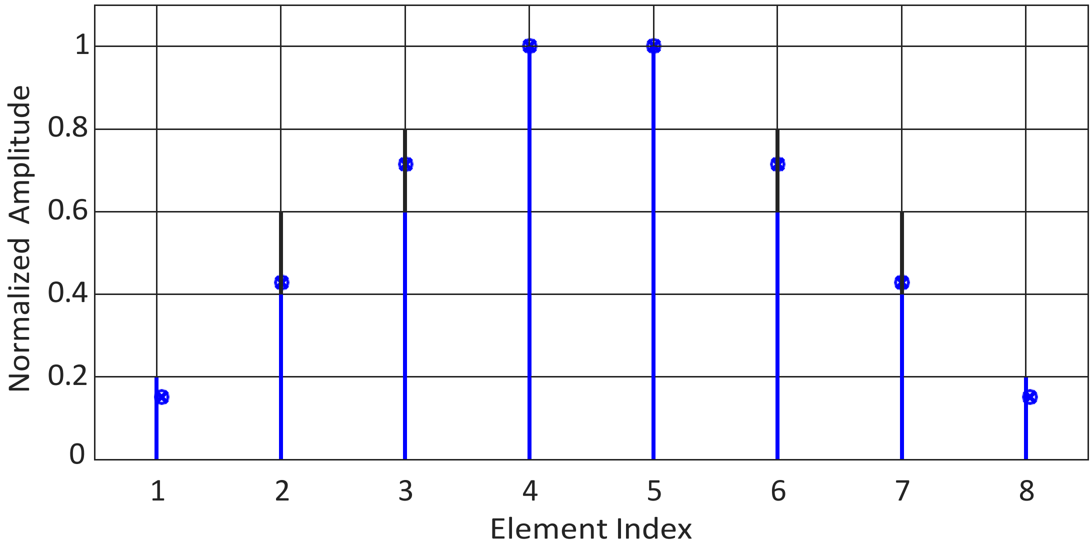

Source: Prepared by the author, 2025.

Figure 12. Normalized array factor (dB) for triangular distribution ($N = 8$, $d = \lambda/2$).

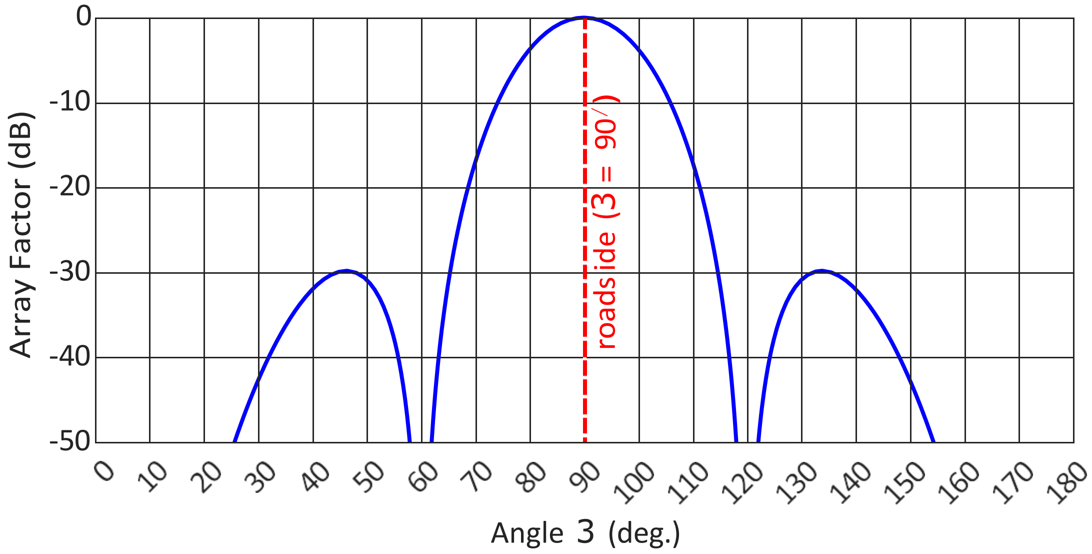

Source: Prepared by the author, 2025.

2.1.5 Hamming Distribution

The Hamming distribution, derived from signal processing, uses a cosine taper to achieve very low side-lobes (Harris, 1978). For $N = 8$:

$$a_n = 0.54 - 0.46 \cos \overset{\text{A}}{} \frac{2\pi(n-1)}{N-1} \overset{\text{B}}{}, \quad n = 1, \dots, 8, \tag{2.65}$$

yielding

$$a_n = [0.0800, 0.2529, 0.6971, 0.9899, 0.9899, 0.6971, 0.2529, 0.0800], \tag{2.66}$$

Figure 13. Normalized amplitude distribution for Hamming distribution ($N = 8$).

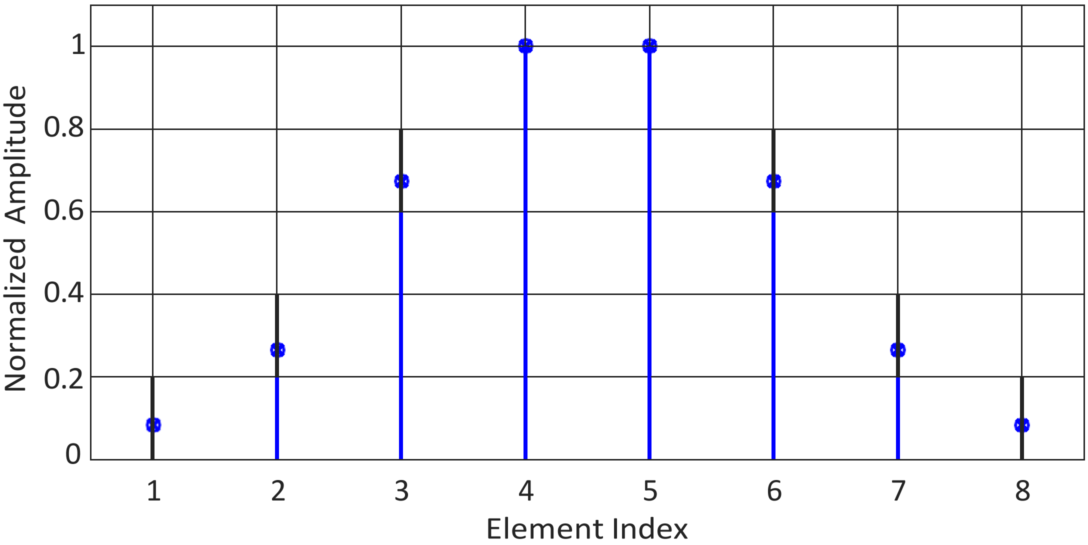

Source: Prepared by the author, 2025.

normalized as

$$a_n = [0.0808, 0.2554, 0.7039, 1.0000, 1.0000, 0.7039, 0.2554, 0.0808]. \tag{2.67}$$

This taper minimizes side-lobes by smoothing the amplitude transition. The amplitude distribution is shown in Fig. 13.

The array factor, in Fig. 14, achieves a SLL of −41.22 dB, HPBW of 10.63°, and directivity of 8.78 dB. Its ultra-low side-lobes make it ideal for 5G beamforming and high-fidelity systems where interference must be minimized, though its directivity is slightly lower than the uniform case (Harris, 1978).

2.1.6 Binomial Distribution

The binomial distribution uses Pascal's triangle coefficients to eliminate side-lobes (Balanis, 2016). For $N = 8$:

$$a_n = \binom{N-1}{n-1}, \quad n = 1, \ldots, 8, \tag{2.68}$$

yielding

$$a_n = [1, 7, 21, 35, 35, 21, 7, 1], \tag{2.69}$$

normalized as

$$a_n = [0.0286, 0.2000, 0.6000, 1.0000, 1.0000, 0.6000, 0.2000, 0.0286] \tag{2.70}$$

.This steep taper theoretically nulls side-lobes by mimicking a polynomial expansion. The amplitude distribution is shown in Fig. 15.

Figure 14. Normalized array factor (dB) for Hamming distribution ($N = 8$, $d = \lambda/2$).

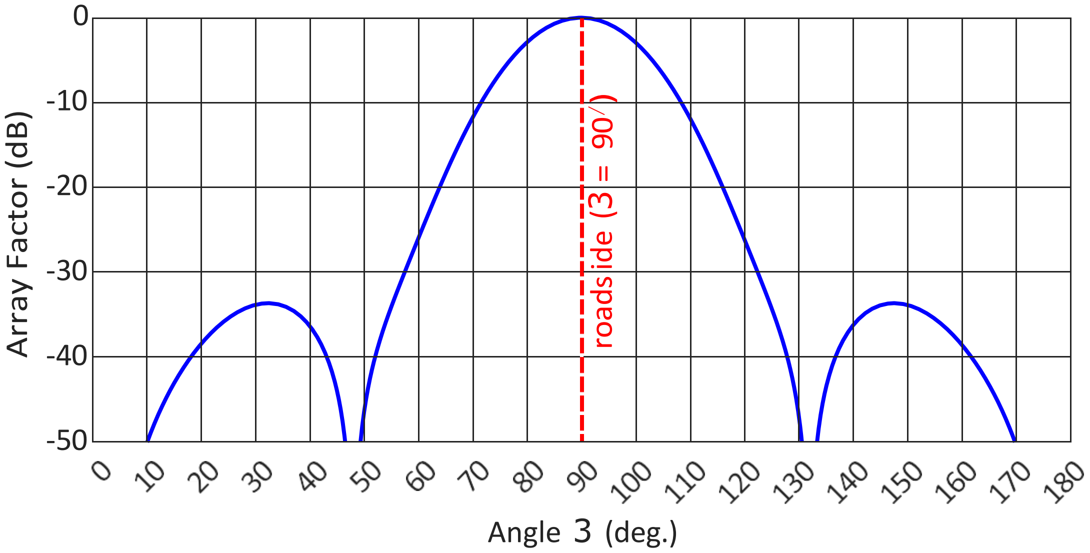

Source: Prepared by the author, 2025.

Figure 15. Normalized amplitude distribution for binomial distribution ($N = 8$).

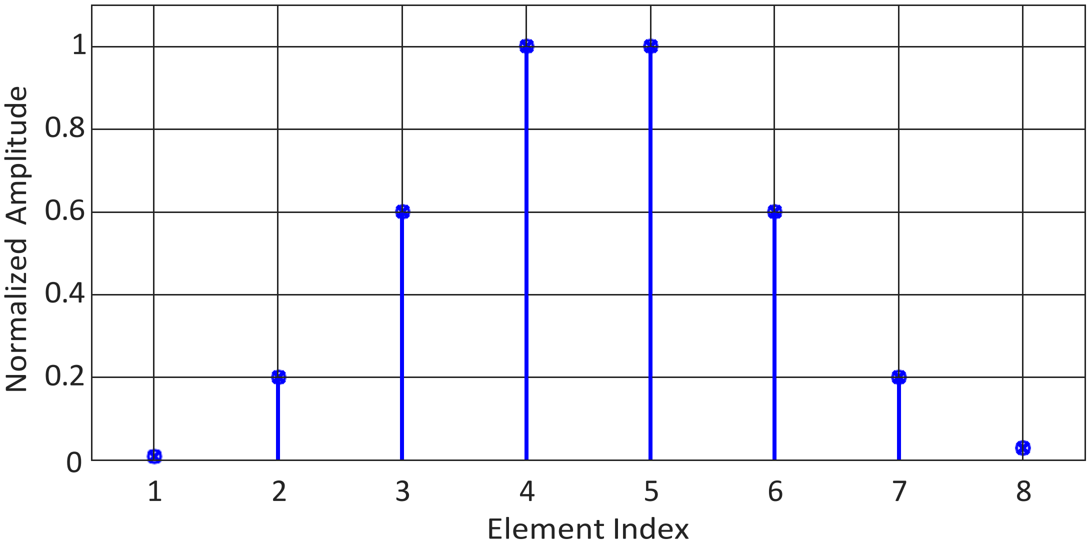

Source: Prepared by the author, 2025.

The array factor, in Fig. 16, has no side-lobes ($-\infty$ dB), an HPBW of 20.16°, and directivity of 7.51 dB. Its wide beam and low directivity limit its use to low-interference scenarios, such as broadcasting, where side-lobe elimination is critical (Balanis, 2016).

2.1.7 Blackman Distribution

The Blackman distribution, adapted from signal processing, uses a dual-cosine taper (Harris, 1978):

Figure 16. Normalized array factor (dB) for binomial distribution ($N = 8$, $d = \lambda/2$).

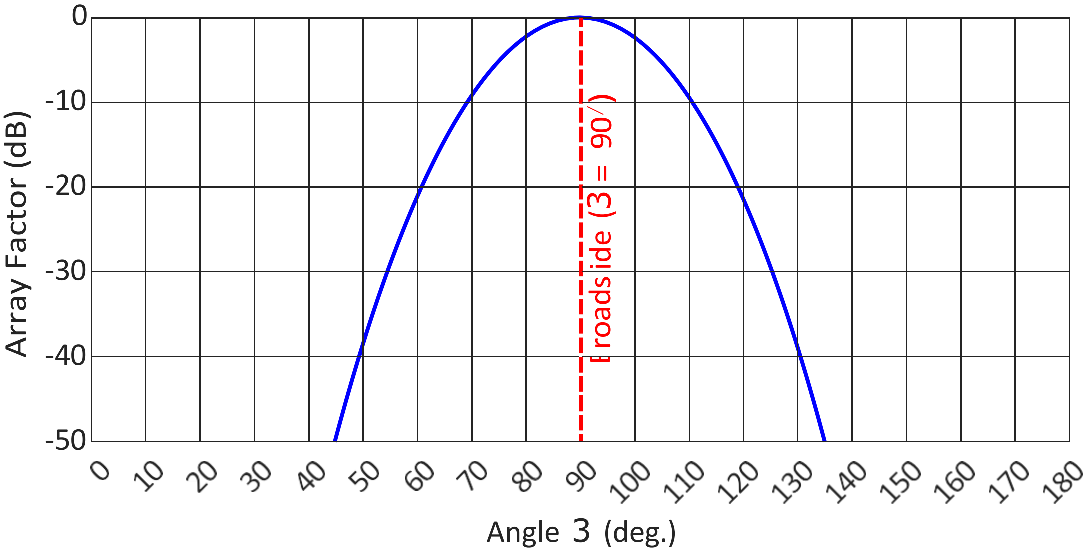

Source: Prepared by the author, 2025.

$$A_n = 0.42 - 0.5\cos\left(\frac{2\pi(n-1)}{N-1}\right) + 0.08\cos\left(\frac{4\pi(n-1)}{N-1}\right), \tag{2.71}$$

yielding

$$a_n = [0.0000, 0.1657, 0.6443, 0.9743, 0.9743, 0.6443, 0.1657, 0.0000], \tag{2.72}$$

normalized as

$$a_n = [0.0000, 0.1700, 0.6612, 1.0000, 1.0000, 0.6612, 0.1700, 0.0000]. \tag{2.73}$$

The dual-cosine terms enhance side-lobe suppression. The amplitude distribution is shown in Fig. 17.

The array factor, in Fig. 18, has a SLL of −20.85 dB, HPBW of 15.10°, and directivity of 7.84 dB. It is effective for mmWave systems requiring low side-lobes with moderate beamwidth, such as 5G networks (Rappaport et al., 2019).

2.1.8 Performance Comparison

Performance metrics for all distributions ($N = 8$, $d = \lambda/2$) are summarized in Table 6. Metrics include main beam direction ($\vartheta_0 = 90^\circ$), SLL (maximum gain outside $\vartheta \in [70^\circ, 110^\circ]$), HPBW, and directivity.

The uniform distribution maximizes directivity but has high side-lobes, suitable for satellite uplinks. Chebyshev distributions offer tunable side-lobe control, with $R_0 = 30$ dB balancing radar needs. Triangular and Hamming distributions provide cost-effective and

Figure 17. Normalized amplitude distribution for Blackman distribution ($N = 8$).

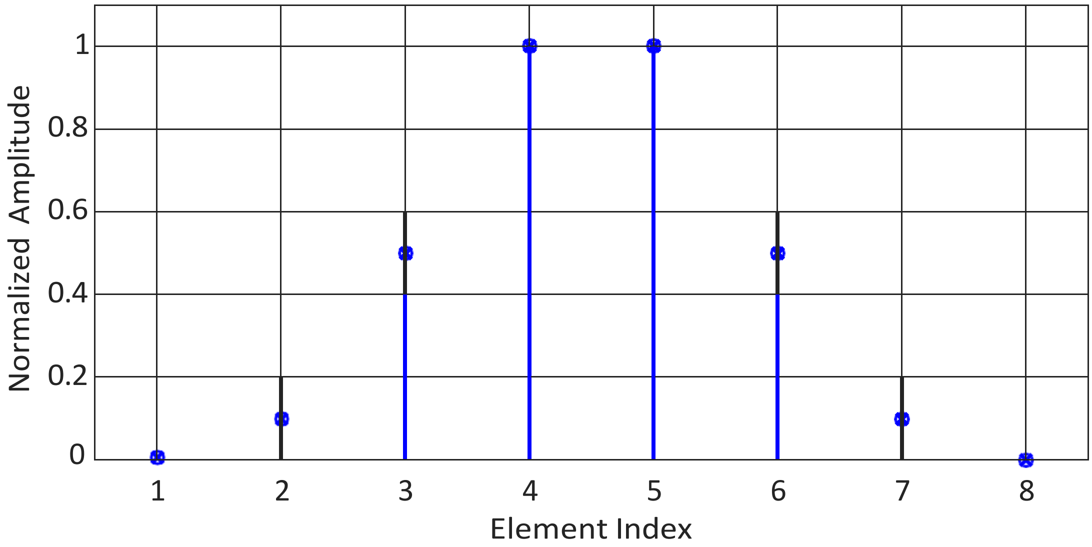

Source: Prepared by the author, 2025.

Figure 18. Normalized array factor (dB) for Blackman distribution ($N = 8$, $d = \lambda/2$).

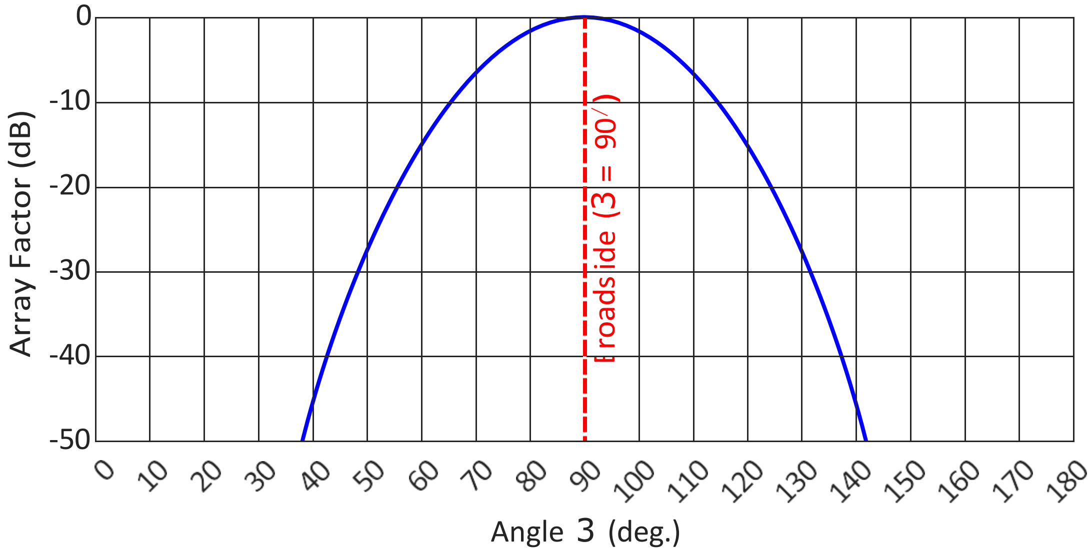

Source: Prepared by the author, 2025.

low-side-lobe solutions, respectively. Binomial eliminates side-lobes but is impractical for high-gain systems. Fig. 19 compares array factors, highlighting beam shape trade-offs.

This section investigated the array factor of linear antenna arrays through a detailed analysis of various amplitude distributions. The study focused on their impact on radiation pattern characteristics, particularly SLL and directivity. Among the distributions examined, the Dolph-Tschebyshev distribution demonstrated superior performance due to its ability to effectively control side-lobe levels while maintaining high directivity. This makes it particularly suitable for series-fed arrays, where amplitude tapering can significantly enhance radiation characteristics. Consequently, the Dolph-Tschebyshev distribution will

Table 4. Performance comparison of amplitude distributions ($N = 8$, $d = \lambda/2$).

Distribution	**Main Beam (deg.)**	**Side-lobe Level (dB)**	**HPBW (deg.)**	**Maximum Direct. (dB)**
Uniform	90.00	−13.20	10.26	9.03
Chebyshev (20 dB)	90.00	−20.00	11.02	8.92
Chebyshev (30 dB)	90.00	−29.98	12.49	8.65
Chebyshev (40 dB)	90.00	−40.00	14.08	8.37
Triangular	90.00	−26.40	13.69	8.35
Hamming	90.00	−41.22	10.63	8.78
Blackman	90.00	−∞	15.10	7.84
Binomial	90.00	−∞	20.16	7.51

Source: Prepared by the author, 2025.

Figure 19. Normalized array factors (dB) for all distributions ($N = 8$, $d = \lambda/2$).

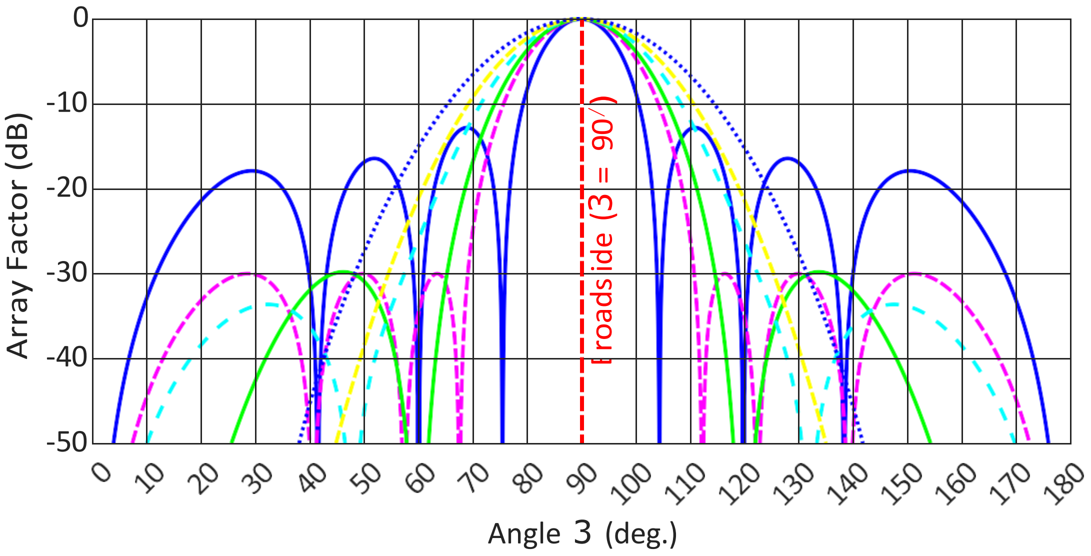

Source: Prepared by the author, 2025.

be employed in the design of the series-fed arrays proposed in this study to achieve improved radiation patterns.

2.2 Rectangular Patch Antenna Design

The rectangular patch antenna is a planar structure consisting of a metallic patch on a dielectric substrate backed by a ground plane, commonly used in microwave and millimeter-wave applications due to its simplicity, low profile, and ease of fabrication (Balanis, 2016) . The geometry, as shown in Figure 20, includes a rectangular patch with width W and length L, fabricated on a substrate with dielectric constant ε_r, height h, and loss tangent $\tan \delta$. The patch and feed line have a metal thickness t. Although various

Figure 20. Geometry of Microstrip Rectangular Patch Antenna.

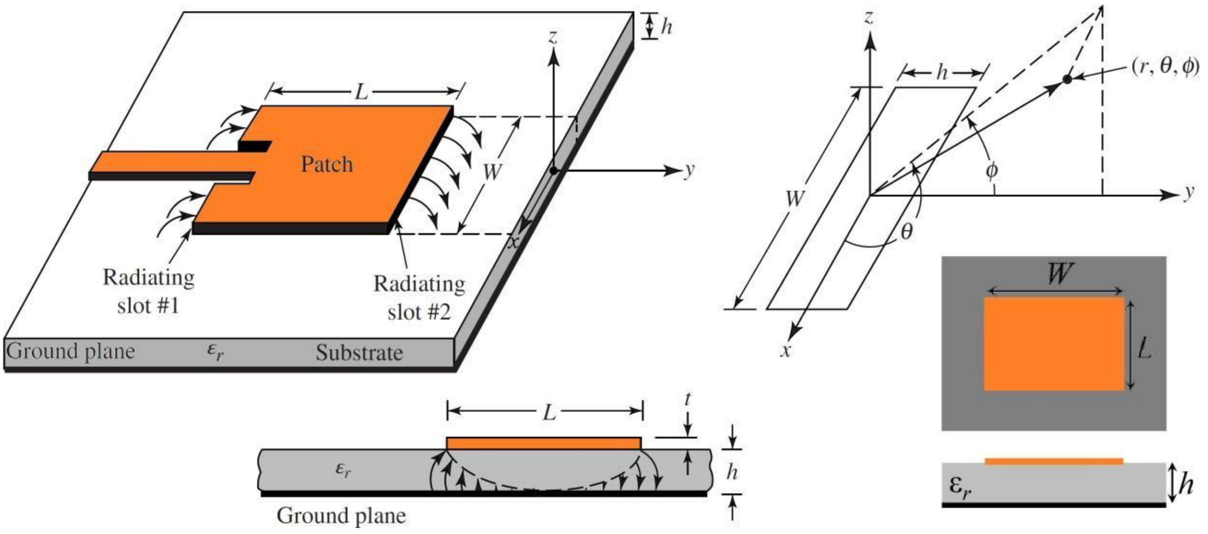

Source: adapted from (Balanis, 2016).

feeding techniques can be employed for microstrip antennas, such as coaxial probe feeding, aperture coupling, and proximity coupling, the microstrip line feed was adopted in this work due to its simplicity, ease of fabrication, and compatibility with planar circuits. The microstrip line width W_0 is designed to achieve the desired characteristic impedance, which is typically 50 Ω. In general, microstrip antennas exhibit high input impedance near the patch edges. For this reason, several techniques can be employed to match the impedance to 50 Ω when using microstrip line feeding. As illustrated in Fig. 21, the most common ones are the *inset feeding*, in which the feed point is shifted a distance y_0 from the radiating edge to achieve impedance matching, and the *quarter-wave transformer* technique. Both approaches are described in detail in the following sections.

2.2.1 Rectangular Patch Design

The patch width W of a rectangular microstrip antenna, depending on the operating mode, is directly related to both the resonant frequency and the antenna's input impedance (Gang, 2001). Typically, for conventional models operating in the fundamental mode, W is estimated based on the substrate's relative permittivity ε_r (Balanis, 2016):

$$W = \frac{c}{2f_r\sqrt{\frac{\varepsilon_r + 1}{2}}}, \tag{2.74}$$

where $c = 3 \times 10^8$ m/s is the speed of light in vacuum, f_r is the desired resonant frequency corresponding to the fundamental mode, and ε_r is the substrate's relative dielectric constant.

Rectangular microstrip antennas are typically modeled as resonant cavities with width W and length L to estimate their resonant frequencies (Gang, 2001). However, unlike an ideal cavity, the electromagnetic fields propagating in the dielectric substrate are not strictly confined within the physical dimensions defined by W and L, leading to a phenomenon known as *fringing*. As a result, the effective electrical length L_{eff} becomes larger than the physical length L and is calculated as follows:

$$L_{\text{eff}} = \frac{c}{2 f_r \sqrt{\varepsilon_{\text{eff}}}}, \tag{2.75}$$

where the fringing effects are initially accounted for by the effective dielectric constant ε_{eff}, which is calculated as

$$\varepsilon_{\text{eff}} = \frac{\varepsilon_r + 1}{2} + \frac{\varepsilon_r - 1}{2}\left[1 + 12\frac{h}{W}\right]^{-1/2}. \tag{2.76}$$

To compensate for the increase in electrical length caused by the fringing effect, the following formulation is applied:

$$L = L_{\text{eff}} - 2\Delta L. \tag{2.77}$$

where the extension length ΔL appears at each radiating edge of the patch, at the ends of L, and is calculated as

$$\Delta L = 0.412\,h\,\frac{(\varepsilon_{\text{eff}} + 0.3)\left(\frac{W}{h} + 0.264\right)}{(\varepsilon_{\text{eff}} - 0.258)\left(\frac{W}{h} + 0.8\right)}. \tag{2.78}$$

2.2.2 Microstrip Feed Line Design

For the antenna feeding system proposed in this work, it is necessary to determine the appropriate width W_0 of the microstrip line. Based on the desired characteristic impedance $Z_0 = 50\ \Omega$ and the parameters of the dielectric substrate, W_0 is determined according to (Balanis, 2016):

$$Z_0 = \begin{cases} \dfrac{60}{\sqrt{\varepsilon_{\text{reff}}}} \ln\left(\dfrac{8h}{W_0} + \dfrac{W_0}{4h}\right), & \text{for } W_0/h \leq 1. \\[2ex] \dfrac{120\pi}{\sqrt{\varepsilon_{\text{reff}}}\left[\dfrac{W_0}{h} + 1.393 + 0.667 \ln\left(\dfrac{W_0}{h} + 1.444\right)\right]}. & \text{for } W_0/h > 1. \end{cases} \tag{2.79}$$

It is noteworthy that, in this case, ε_{eff} must be calculated by considering the width W_0, so that its expression becomes

$$\epsilon_{\text{reff}} = \frac{\varepsilon_r + 1}{2} + \frac{\varepsilon_r - 1}{2}\left[1 + 12\frac{h}{W_0}\right]^{-1/2}, \quad \text{for } W_0/h > 1. \tag{2.80}$$

Figure 21. Feed methods for rectangular microstrip patch antennas.

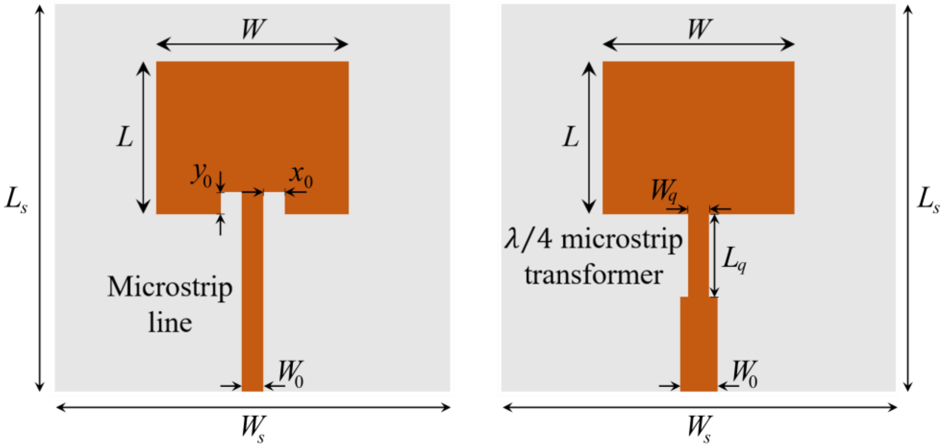

Source: adapted from (Balanis, 2016).

To determine the ratio W_0/h as a function of Z_0, the above impedance equations must be inverted. Since $\varepsilon_{\text{reff}}$ depends on W_0/h, the equations are transcendental, requiring numerical or iterative solutions. The synthesis formulas distinguish between narrow and wide strips based on the impedance condition. For narrow strips, high impedance, i.e., when $Z_0 > (44 - 2\epsilon_r)\ \Omega$ (Edwards; Steer, 2016; Hammerstad, 1975):

$$\frac{W_0}{h} = \left(\frac{\exp\tau}{8} - \frac{1}{4\exp\tau}\right)^{-1}, \tag{2.81}$$

where

$$\tau = \frac{Z_0\sqrt{2(\epsilon_r+1)}}{119.9} + \frac{1}{2}\left(\frac{\epsilon_r-1}{\epsilon_r+1}\right)\left(\ln\frac{\pi}{2} + \frac{1}{\epsilon_r}\ln\frac{4}{\pi}\right). \tag{2.82}$$

The effective relative permittivity, under the slightly different condition, $W_0/h < 1.3$ is calculated as

$$\varepsilon_{\text{reff}} = \frac{\epsilon_r+1}{2}\left[1 - \frac{1}{2\tau}\left(\frac{\epsilon_r-1}{\epsilon_r+1}\right)\left(\ln\frac{\pi}{2} + \frac{1}{\epsilon_r}\ln\frac{4}{\pi}\right)\right]^{-2}, \tag{2.83}$$

where τ is given by equation (2.82). For wide strips, low impedance, i.e., when $Z_0 <$ $(44 - 2\epsilon_r)\ \Omega$ (Edwards; Steer, 2016; Hammerstad, 1975):

$$\frac{W_0}{h} = \frac{2}{\pi}\left[(\chi-1) - \ln(2\chi-1)\right] + \frac{\epsilon_r-1}{\pi\epsilon_r}\left[\ln(\chi-1) + 0.293 - \frac{0.517}{\epsilon_r}\right], \tag{2.84}$$

where

$$\chi = \frac{59.95\pi^2}{Z_0\sqrt{\varepsilon_r}}, \tag{2.85}$$

The effective relative permittivity, again with the slightly different condition, $W_0/h > 1.3$:

$$\varepsilon_{\text{eff}} = \frac{\epsilon_r+1}{2} + \frac{\epsilon_r-1}{2}\left(1 + 10\frac{h}{W_0}\right)^{-0.555}. \tag{2.86}$$

2.2.3 Impedance Matching

Impedance matching between the feed line and the antenna input is essential to minimize transmitted power loss caused by signal reflections. Since the feed line is typically a microstrip line designed to have a characteristic impedance of 50 Ω, and the antenna input impedance can assume much higher values, impedance matching techniques become necessary. Two common techniques for matching the microstrip patch antenna to the feed line are the inset feed and the quarter-wave transformer, each presenting distinct characteristics, advantages, and limitations.

2.2.3.1 *Inset Feed Method*

The inset feed technique (see Fig. 21) consists of offsetting the feed point along the patch length to adjust the input impedance for matching with the feed line. In this configuration, a microstrip line is connected to the patch at a distance y_0 from the radiating edge, where the input impedance Z_{in} can be approximated as:

$$Z_{in}(y_0) = Z_{edge}\cos^2\left(\frac{\pi y_0}{L}\right) \tag{2.87}$$

where Z_{edge} is the edge impedance of the patch, typically high (200–300 Ω), due to the resonant nature of the patch (Balanis, 2016).

The input impedance at the patch edge for the fundamental mode (TM_{10}) can be calculated using the transmission-line model (Balanis, 2016). In this analysis, for the TM_{10} mode, the antenna is approximated by two radiating slots located at the edges along the length L. Therefore, the edge input impedance of the patch can be calculated by considering the two radiating slots connected in parallel. Thus, the following expression is obtained:

$$Z_{edge} = R_{in} = \frac{1}{2(G_1 + G_{12})}. \tag{2.88}$$

where G_1 is the conductance of each slot, which can be expressed as:

$$G_1 = \frac{W}{120\lambda_0}\left[1 - \frac{(k_0 h)^2}{24}\right], \tag{2.89}$$

where $\lambda_0 = c/f_r$ is the free-space wavelength, $k_0 = 2\pi/\lambda_0$ is the free-space wavenumber, and G_{12} is the mutual conductance between the two slots:

$$G_{12} = \frac{1}{120\pi^2}\int_0^\pi \left[\frac{\sin\left(\frac{k_0 W}{2}\cos\vartheta\right)}{\cos\vartheta}\right]^2 J_0(k_0 L\sin\vartheta)\sin^3\vartheta\, d\vartheta, \tag{2.90}$$

where $J_0(\cdot)$ is the zeroth-order Bessel function of the first kind.

To match the feed line impedance Z_0, the inset depth y_0 is calculated as

$$y_0 = \frac{L}{\pi}\arccos\left(\sqrt{\frac{Z_0}{Z_{edge}}}\right). \tag{2.91}$$

Table 5. Comparison of Inset Feed and Quarter-Wave Transformer Methods

Aspect	**Inset Feed**	**Quarter-Wave Transformer**
Implementation	Cutout in patch	Additional transmission line
Substrate Area	Minimal (compact)	Requires extra space
Bandwidth	Narrower	Wider
Radiation Pattern	May be affected	Preserved
Advantages	Simple, compact, cost-effective	Better bandwidth, no patch alteration
Disadvantages	Pattern distortion, sensitive to tolerances	Larger footprint

Source: Prepared by the author, 2025.

A more precise formula, accounting for the input resistance at resonance Z_{edge}, is

$$y_0 = \frac{L}{2}\left(1 - \frac{Z_0}{R_{edge}}\right). \tag{2.92}$$

The inset feed technique is simple to implement, as it requires only a cutout in the patch, making it a compact and cost-effective solution, particularly suitable for single-layer printed circuit board (PCB) fabrication. It does not require any additional substrate area beyond the patch itself. However, this technique has certain limitations: the inset cut can perturb the current distribution on the patch, potentially affecting the radiation pattern, especially for deeper inset positions. Moreover, precise fabrication is essential to achieve the desired impedance, since small variations in y_0 can significantly alter Z_{in}. The technique also becomes less effective for substrates with high dielectric constants or for thick substrates, where the edge impedance may vary considerably.

2.2.3.2 *Quarter-Wave Transformer*

The QWT method (see Fig. 21) employs a transmission line section of length $\lambda_g/4$ (where λ_g is the guided wavelength) and characteristic impedance Z_q to match the patch's edge impedance Z_p to the feed line impedance Z_0. The transformer impedance is

$$Z_q = \sqrt{Z_0 Z_p}. \tag{2.93}$$

The length of the quarter-wave section L_q is

$$L_q = \frac{\lambda_g}{4} = \frac{c}{4 f_r \sqrt{\varepsilon_{\text{eff}}}} \tag{2.94}$$

where ε_{eff} is the effective dielectric constant of the substrate defined at equation 2.80.

As illustrated in Table 5, the inset feed and QWT methods exhibit significant differences in their implementation and performance characteristics. The inset feed is integrated directly into the patch antenna, eliminating the need for additional substrate area, thus making it well-suited for compact designs. However, this approach may introduce distortions in the radiation pattern and is highly sensitive to fabrication tolerances. In contrast, the QWT, adopted in this work, preserves the patch geometry and provides superior bandwidth performance, albeit at the cost of requiring additional substrate area and precise transmission line design.

2.3 Series-Fed Microstrip Antenna Arrays

A single microstrip patch antenna typically exhibits a broad radiation pattern with low directivity, yielding a gain of approximately 5–7 dBi (Balanis, 2016, Ch. 6). To enhance performance, antenna arrays combine multiple radiating elements to increase the electrical size of the aperture, achieving higher gain and tailored radiation characteristics. The aperture distribution, defined by the amplitude and phase excitation of each element, governs the array's radiation pattern, enabling applications such as low side-lobe beams or beam steering (Balanis, 2016, Ch. 14). At millimeter-wave frequencies, such as 60 GHz, series-fed microstrip patch arrays are advantageous due to their reduced feed network losses and simplified fabrication, making them suitable for automotive radar and high-data-rate communications (Metz; Eberhardt; Bangert, 2004).

This section compares parallel- and series-fed array configurations, evaluates their suitability for high-frequency applications, and classifies series-fed arrays into traveling-wave and resonant types. A detailed design methodology for a resonant series-fed array with open-circuit termination is provided, focusing on geometry, impedance modeling, and radiation characteristics for a generic N-element array operating at 60 GHz.

2.3.1 Parallel- vs. Series-Fed Arrays

Microstrip patch antenna arrays can be configured using either parallel-fed (corporate-fed) or series-fed topologies (Balanis, 2016, Ch. 14). Parallel-fed arrays employ a single input port that distributes power through a corporate feed network, typically comprising Wilkinson power dividers or T-junctions, with each branch line terminating at an individual patch. This configuration facilitates independent amplitude control at each element, enabling low SLL (e.g., with Chebyshev tapering). It also allows moderate bandwidths (typically 10–20%) due to reduced mutual coupling and relatively uniform excitation, although frequency-dependent phase errors are not entirely eliminated (Bhartia et al., 2000). The parallel structure's amplitude control is achieved through fixed-ratio power dividers, ensuring stable pattern performance across the band. However, at millimeter-wave frequencies, the extended feed network introduces significant conductor and dielectric losses due to high attenuation constants, exacerbated by multiple junctions with inser-

Table 6. Comparative Analysis of Parallel- and Series-Fed Microstrip Patch Arrays

Parameter	**Parallel-Fed**	**Series-Fed**
Bandwidth	Wider (10–20%, isolated feeds)	Moderate (5–10%, cascaded)
Efficiency	Moderate	High
Complexity	High (multiple dividers)	Low (continuous line)
Beam Squint	Low (independent phases)	High ($\Delta\vartheta$ a Δf)
Side-lobe Control	Excellent	Good
mm-Wave Suitability	Limited	Preferred (low loss, compact)

Source: Prepared by the author, 2025.

tion losses (Park et al., 2019; Hu; Hong, 2018). These losses degrade efficiency and limit scalability, as the feed network increases parasitic radiation and cross-polarization.

Series-fed arrays connect patches along a continuous microstrip line, with power coupled progressively via direct inset, proximity, or aperture coupling (Metz; Eberhardt; Bangert, 2004). They require fewer feed lines, reducing ohmic losses and parasitic effects, achieving efficiencies >90% and simplifying fabrication for monolithic integration with linewidth tolerances of ±5 μm (Hu; Hong, 2018). The single-line topology minimizes junction discontinuities, yielding reflection coefficients and enabling compact layouts for conformal applications. However, the cascaded excitation results in narrower bandwidths (5–10%) and beam squint due to dispersive phase progression $\phi_n = \beta(f)d_n$, where

$$\beta(f) = \frac{2\pi f\sqrt{\epsilon_{eff}}}{c} \tag{2.95}$$

causing main beam deviation (Metz; Eberhardt; Bangert, 2004; Hu; Hong, 2018)

$$\Delta\vartheta \approx (\Delta f/f) \tan \vartheta_0. \tag{2.96}$$

Sensitivity to element mismatches propagates reflections, increasing VSWR. Table 6 summarizes these trade-offs, highlighting series-fed designs' superiority in loss-critical mm-wave scenarios (Hu; Hong, 2018; Metz; Eberhardt; Bangert, 2004). At 60 GHz and 79 GHz, series-fed arrays are preferred due to minimized feed losses and compatibility with compact layouts, essential for millimeter-wave systems where parallel networks suffer from accumulated attenuation in extended branches (Park et al., 2019; Hu; Hong, 2018).

2.3.2 Traveling-Wave vs. Resonant Series-Fed Arrays

Series-fed microstrip patch antenna arrays are categorized into traveling-wave and resonant configurations based on their termination and excitation mechanisms (Hansen, 2007, Ch. 7). In traveling-wave arrays, the feed line is terminated with a matched load (typically 50 Ω), establishing a unidirectional propagating wave along the array. The phase progression between elements is governed by the propagation constant $\beta = 2\pi/\lambda_g$, where $\lambda_g = \lambda_0/\sqrt{\varepsilon_{\text{eff}}}$ is the guided wavelength in the substrate with effective permittivity ε_{eff}. This configuration enables flexible beam shaping by controlling the coupling coefficients at each element through inset depth or proximity gaps, facilitating low SLL and beam tilting for scanning applications (Zhang; Mao, 2017). The power decay along the line follows

$$P(z) = P_0 e^{-2\alpha z}, \tag{2.97}$$

where α is the attenuation constant (including conductor and dielectric losses), leading to 10–20% power dissipation in the load for $N > 4$ elements, reducing radiation efficiency (Balanis, 2016). The broader bandwidth results from the non-resonant nature, where the input impedance remains stable over a wider frequency range due to minimal reflections from the matched load (Zhang; Mao, 2017). However, beam squint is significant, as the phase shift varies linearly with frequency f, altering the main lobe direction (Lee; KIM, 2016; Park et al., 2019).

Resonant series-fed arrays employ an open- or short-circuit termination, creating a standing wave that equalizes amplitudes across elements for broadside radiation. The open-circuit termination reflects all incident power, achieving high efficiency by ensuring complete re-radiation without load dissipation, as the voltage standing wave ratio (VSWR) is optimized for constructive interference at resonance (Wang; Li; Zhang, 2016). Short-circuit terminations suppress end-fire lobes but may excite higher-order modes, degrading pattern symmetry due to non-uniform current distributions (Wang; Li; Zhang, 2016). The narrower bandwidth stems from the resonant condition, where the input impedance Z_{in} exhibits a high-Q response, sensitive to frequency deviations that detune the phase alignment $\phi_n = n\pi$ required for broadside summation (Bhartia et al., 2000).Beam squint is reduced compared to traveling-wave designs due to bidirectional wave interference stabilizing the phase center, though it persists due to dispersive $\varepsilon_{\text{eff}}(f)$ (Balanis, 2016). The amplitude distribution is inherently uniform, yielding higher SLL (−13 dB for uniform excitation), unless tapered via patch width variations, which complicates impedance matching (Metz; Eberhardt; Bangert, 2004). The standing wave in resonant arrays results from total reflection ($\Gamma \approx 1$), with Z_{in} governed by the recursive interaction of patch admittances $Y_p = 1/Z_p$ and line impedances, leading to a multi-resonator network (Hansen, 2007). This high-Q behavior limits bandwidth but enhances efficiency, making resonant arrays ideal for fixed-beam applications (Hu; Hong, 2018). Table 7 summarizes these trade-offs, highlighting the suitability of traveling-wave arrays for wideband, scanning applications and resonant arrays for high-efficiency, fixed-beam systems.

Table 7. Traveling-Wave vs. Resonant Series-Fed Arrays

Type	**Termination**	**Pros**	**Cons**
Traveling-Wave	Matched Load	Wide BW ; Low VSWR; Beam scanning	Load loss; High squint
Resonant (Open)	Open Circuit	High efficiency; Simple matching	Narrow BW ; Moderate squint
Resonant (Short)	Short Circuit	Low endfire; Stable phase	Higher-order modes; Narrow BW

Source: Prepared by the author, 2025.

Figure 22. Equally spaced series-fed array of rectangular microstrip patch antennas.

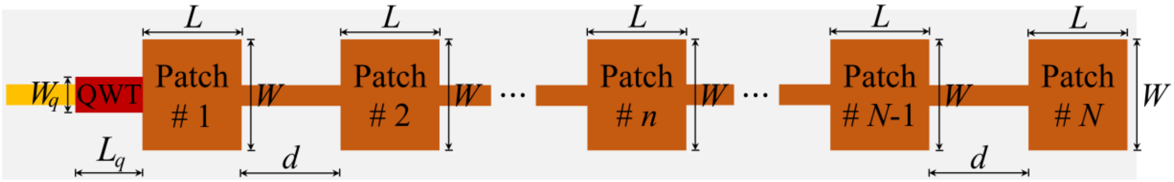

Source: Prepared by the author, 2025.

2.3.3 Design of Resonant Series-Fed Array

The design of an N -element resonant series-fed array with open-circuit termination follows an iterative methodology integrating transmission-line theory, cavity model approximations, and full-wave validation, optimized for 60 GHz operation (Metz; Eberhardt; Bangert, 2004). Initial patch dimensioning ensures resonance at the center frequency, followed by feed-line synthesis for phase alignment, and impedance optimization accounting for mutual coupling. This approach leverages the standing-wave excitation to achieve uniform amplitudes while mitigating bandwidth limitations through proximity coupling enhancements (Hu; Hong, 2018).

The array comprises N rectangular patches of dimensions $L \times W$ aligned along the E-plane (length parallel to H-field), interconnected by microstrip lines of length d and width W_f (characteristic impedance $Z_0 \approx 50\ \Omega$), as shown in Fig. 22. The patch length L and patch width W are given by equations (2.74) and (2.77).

Element spacing is set to $d = \lambda_g/2$, where $\lambda_g = \lambda_0/\sqrt{\varepsilon_{\text{eff}}}$, ensuring in-phase broadside radiation due to 180° phase reversal from mutual coupling in the E-plane, which aligns the TM_{10} mode fields without grating lobes for scan angles $|\vartheta| < 60^\circ$ (Bhartia et al., 2000). Transposed arrays, alternating patch orientations every element, reduce spacing to $d = \lambda_g/4$ by exploiting the 180° field inversion, enabling wider instantaneous scan ranges (up to ±45°) while preserving boresight gain, though increasing cross-polarization by 3–5 dB (Zhang; Mao, 2017). Coupling is controlled via proximity gaps or inset feeds, with coefficients derived from induced EMF theory to achieve uniform excitation in resonant mode (Metz; Eberhardt; Bangert, 2004). The open-circuit termination at the distal end induces the standing wave, with post-patch stub length $l_N \approx \lambda_g/4$ fine-tuned to minimize end-fire radiation.

The array is modeled as a cascaded transmission-line network with shunt patch admittances $Y_p = 1/Z_p$, where $Z_p \approx 200\text{–}300\ \Omega$ at resonance for edge-fed patches, incorporating cavity model susceptance (Balanis, 2016). For an open-circuit termination, the impedance at the N-th element is purely reactive:

$$Z_{in,N} = jZ_0 \tan(\beta l_N), \tag{2.98}$$

where l_N is the stub length (negligible for direct connection, $\beta l_N \approx 0$). For preceding elements $n = N - 1, \ldots, 1$, the recursive formulation is:

$$Z_{in,n} = Z_0 \frac{Z_{in,n+1} + jZ_0 \tan(\beta d_n)}{Z_0 + jZ_{in,n+1} \tan(\beta d_n)} + Z_{p,n}, \tag{2.99}$$

with $Z_{p,n} = R_p + jX_p$, where real part $R_p = R_{edge} \cos^2(ky_0)$ ($k = 2\pi/\lambda_g$, $R_{edge} \approx 1/(2G_{edge})$, G_{edge} from edge admittance), and $X_p \approx 0$ at resonance via inset depth y_0 (Balanis, 2016). This cascade reflects the standing-wave interaction, where mismatches amplify VSWR, limiting bandwidth to $\Delta f/f_0 \approx 1/(2Q)$, with $Q \approx Q_s/N$ for large N due to multi-resonator detuning (Metz; Eberhardt; Bangert, 2004).

The far-field radiation pattern is the product of the single-element pattern $E_{\mathrm{elem}}(\vartheta)$ (broadside-directed for TM_{10}, half-power beamwidth $\approx 80^\circ$ in E-plane) and the array factor $\mathrm{AF}(\vartheta)$:

$$E_{\mathrm{total}}(\vartheta) = E_{\mathrm{elem}}(\vartheta) \times \mathrm{AF}(\vartheta), \tag{2.100}$$

where

$$\mathrm{AF}(\vartheta) = \sum_{n=1}^{N} a_n e^{j(n-1)k_0 d \sin\vartheta + \phi_n}, \tag{2.101}$$

with a_n the excitation amplitude, $\phi_n = \beta d_n + \Delta\phi_{coup}$ (coupling phase), and $k_0 = 2\pi/\lambda_0$ (Balanis, 2016, Ch. 6). For resonant arrays, the standing wave yields uniform $a_n \approx a_0$ and $\phi_n \approx n\pi$ (odd multiples for broadside), producing a directive pattern with directivity

$$D \approx 2N \left(\frac{L}{\lambda_0}\right), \tag{2.102}$$

and SLL of -13 dB (uniform) or <-20 dB (tapered via W_n variation) (Wang; Li; Zhang, 2016). Mutual coupling distorts the pattern in side-lobes due to embedded element patterns shifting with position (n), more pronounced in E-plane (Deshmukh; Ray, 2019). Beam squint, less then 5°/GHz, arises from $\beta(f)$ dispersion but is reduced in resonant designs by symmetric forward/reflected waves averaging phase errors (Park et al., 2019).

2.4 Fabrication on MnM Technology

The continuous advancement of printed circuit board (PCB) fabrication and complementary metal–oxide–semiconductor (CMOS) integration technologies has sustained decades of progress in both digital and analog electronic systems, enabling compact, low-cost, and energy-efficient implementations across diverse applications. Nevertheless, the increasing demand for high-gain and highly directive antennas—particularly within the millimeter-wave (mmWave) and sub-terahertz frequency ranges—has driven the widespread adoption of antenna array architectures. These arrays inherently require larger physical apertures to maintain element spacing proportional to the operating wavelength, as well as complex feeding networks to ensure precise phase and amplitude control. As a result, conventional fabrication approaches encounter substantial limitations when applied to mmWave circuits, where extreme miniaturization and elevated operating frequencies exacerbate transmission losses, parasitic coupling, and manufacturing tolerances, ultimately increasing design complexity and production costs.

In CMOS-based platforms, the implementation of antenna arrays is inherently constrained by the physical and electrical limitations of the silicon substrate, including substantial area requirements for feed networks and increased fabrication costs associated with high-density integration. As mmWave electronics evolve toward 5G and beyond, the demand for innovative integration strategies has intensified, emphasizing three-dimensional (3D) heterogeneous systems that co-package active and passive components. Over the past decade, research has increasingly focused on 3D integration paradigms, in which active CMOS dies are interfaced with a passive interposer layer that connects to the primary PCB, hosting transmission lines, filters, and radiating elements (Pelegrini et al., 2016a). The reduced fabrication cost results from the fact that the membrane is produced through low-temperature, solution-based processes and does not require multilayer lamination, chemical plating steps, or precision-controlled subtractive etching. As a consequence, its manufacturing workflow is significantly simpler than that of conventional PCB technologies. This approach not only optimizes area utilization but also improves signal integrity through vertical interconnections, enabling compact, multifunctional modules suitable for high-frequency applications.

This section provides a detailed overview of Metallic-Nanowire-Membrane (MnM) technology as an emerging interposer platform for 3D heterogeneous integration in millimeter-wave systems. MnM employs a nanoporous anodic aluminum oxide (AAO) membrane as a low-cost, low-loss substrate that inherently supports high-density vertical interconnects. By electrodepositing metallic nanowires into the membrane pores, MnM enables through-substrate vias (TSVs) with superior performance compared to conventional silicon or glass interposers, allowing non-planar crossovers and compact passive components critical for beamforming networks, such as Butler matrices (Pinheiro, 2020).

Figure 23. Manufacturing steps to build a device on MnM substrate, including a TSV.

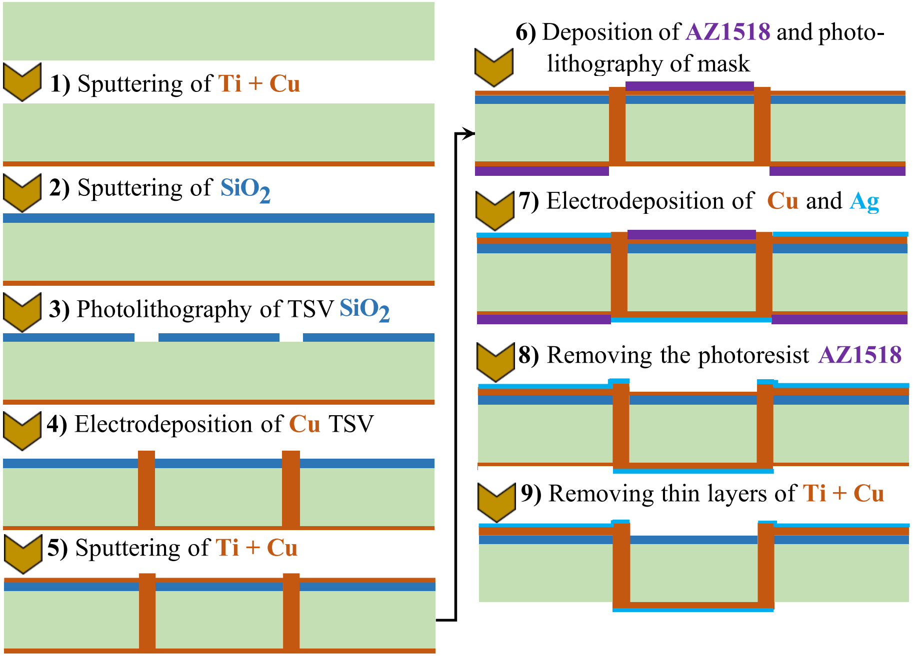

Source: adapted from (Verona et al., 2024).

The MnM platform leverages electrochemical fabrication techniques, notably the controlled anodization of aluminum foils—a method systematically explored since the mid-1990s. Pioneering work by Masuda and Fukuda introduced a two-step anodization process that produces highly ordered, honeycomb-like nanopore arrays in anodic aluminum oxide (AAO). By adjusting anodization voltage and electrolyte composition, they achieved pore diameters ranging from 20 nm to 400 nm and interpore distances spanning tens to hundreds of nanometers (Masuda; Fukuda, 1995). Post-anodization annealing at elevated temperatures, such as 600°C for four hours, refines the pore morphology, enhancing mechanical stability and uniformity. These AAO membranes, typically 50–300 µm thick, exhibit a relative permittivity of approximately 6.7 and a loss tangent of about 0.015 at millimeter-wave frequencies, making them suitable for low-loss dielectric applications in high-frequency interconnects (Pelegrini et al., 2016a).

In this work, the adopted MnM substrate consists of a 50 µm-thick nanoporous anodic aluminum oxide (AAO) membrane with 40 nm-diameter pores and an interpore spacing of 107 nm, sourced from the commercial supplier InRedox. This configuration provides a high via density of approximately 95 pores per square micrometer, while maintaining controllable electrodeposition conditions. The employed membrane, shown in Fig. 23, has a diameter of 25 mm and was annealed at 600 °C for four hours to enhance mechanical stability. The high-density nanopores enable the fabrication of through-substrate vias (TSVs) connecting the top and bottom metallization layers, achieving low insertion losses (Pelegrini et al., 2016a).

The fabrication of through-membrane interconnects using MnM (Membrane nanoMetallization) technology involves a multi-step process combining surface preparation, thin-film deposition, patterning, and selective electrodeposition to produce high-aspect-ratio copper nanowires. This methodology ensures robust adhesion, selective growth, and corrosion resistance, supporting applications in microsystems and flexible electronics. The process proceeds as follows (Verona et al., 2024):

1. The backside of the membrane is coated with thin titanium (Ti, < 20 nm) and copper (Cu, < 50 nm) layers via RF magnetron sputtering. Titanium provides adhesion for the copper seed layer, which facilitates the electrodeposition of copper nanowires through the nanopores.
2. A silicon dioxide SiO_2, 200 nm) layer is deposited on the front side via reactive sputtering, acting as a mask to restrict copper nanowire growth to designated regions.
3. The through-substrate via (TSV) pattern is transferred to the SiO_2 mask using photolithography followed by etching with buffered oxide etchant (BOE) to define precise growth sites.
4. Copper nanowires are selectively grown by electrodeposition in a cupric sulfate solution until a continuous copper film is formed on the front side.
5. Thin Ti/Cu films are sputtered on the front side to provide symmetric metallization and prepare the surface for subsequent processing.
6. Device features and crossovers are defined using AZ1518 photoresist on the front side, followed by selective copper thickening up to 3 μm via electrodeposition. The same procedure is repeated on the backside to define the complementary metallization.
7. Selective copper electrodeposition (3 μm) is performed in regions not covered by photoresist.
8. Photoresist is removed from both the front and back sides.
9. Residual thin Ti and Cu layers are removed by chemical etching using a solution of ceric ammonium nitrate in acetic acid.

All antennas presented in this work were fabricated at the Millimeter-Wave Laboratory of Poli-USP, under the supervision of Professors Gustavo Pamplona Rehder and Ariana Serrano. The experimental characterization of the prototypes was also conducted at the same facility. Chapter 3 provides a detailed description of the characterization procedures.

3 Numerical and Experimental Results

This chapter presents and discusses the simulation results, including the reflection coefficient ($|S_{11}|$), impedance matching (Z), and radiation patterns in the E- and H-planes. The key design parameters of the developed antenna are summarized in Table 8.

Table 8. Rectangular Patch Antenna Design Parameters

Parameter	Symbols	**Value**
Frequency	f_r	60 GHz
Dielectric Constant	ϵ_r	6.7
Substrate Height	h	50 µm
Metal Thickness	t	3 µm
Loss Tangent	$\tan\delta$	0.015

Source: Prepared by the author, 2025.

Each patch element, either isolated or part of a series-fed array, is excited through a CPW-G probe connected to a microstrip feed line, as illustrated in Figure 24. Vertical interconnections between the radiating elements and the ground plane were implemented using through-substrate vias (TSVs) formed within the nanoporous alumina membrane acting as the MnM interposer. The TSVs, with a diameter of approximately 25 µm, are uniformly distributed beneath each patch element to ensure stable grounding and to minimize parasitic inductance. The nanoporous alumina structure is filled with electroplated copper nanowires, providing vertical electrical conduction through the dielectric thickness. These nanowires establish a dense conductive network that enables high-frequency operation of the array. The total membrane thickness is approximately 50 µm, offering mechanical flexibility while maintaining low insertion loss at mmWave frequencies.

Arrays composed of two, four, and eight microstrip patch elements were implemented using the MnM technique (see Figure 25) to investigate the minimum number of elements required to ensure that the frequency spacing between successive resonances is sufficiently small to form a continuous operating band. Each patch element was patterned on the top surface of a dielectric membrane, while a continuous copper layer on the bottom side served as the ground plane.

In order to characterize the fabricated antenna, the measurement setup shown in Fig. 26 was assembled. A standard gain horn antenna was positioned above the array under test and used as the transmitting element in a near-field measurement configuration. The reflection coefficient S_{11} and the radiation pattern of the fabricated array were measured to evaluate its performance.

Figure 24. Photograph of the fabricated MnM-based microstrip transmission line with pads at different scales.

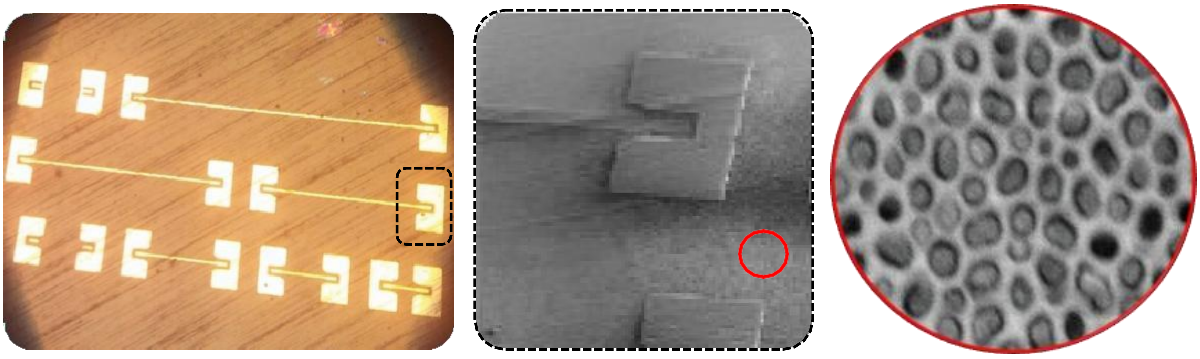

Source: Prepared by the author, 2025.

3.1 Fed-Series Array Operating at 60GHz

This section details the design and optimization of a single-element rectangular microstrip patch antenna intended for use as a radiating element within a series-fed array. The antenna geometry, as depicted in Figure 20, was modeled and simulated using Ansys HFSS. The primary objective was to determine the optimal dimensions for resonant operation at 60 GHz, while simultaneously evaluating key performance metrics such as input impedance, reflection coefficient (S_{11}), and radiation efficiency. The findings from this initial single-element analysis will serve as the foundation for the subsequent design and development of the complete series-fed array, assessing the feasibility of its fabrication and performance at mmW frequencies.

3.1.1 Single Rectangular Microstrip Antenna

Consider a rectangular patch antenna designed for an operating frequency f_r = 60 GHz, with a substrate having dielectric constant $\epsilon_r = 6.7$, height h = 50 µm, metal thickness t = 3 µm, and loss tangent $\tan\delta = 0.015$ (see Table 8) . The speed of light is $c = 3 \times 10^8$ m/s. The feed line impedance is $Z_0 = 50\ \Omega$. The width W of the patch is calculated using the classical formula:

$$W = \frac{c}{2f_r}\sqrt{\frac{2}{\epsilon_r + 1}} \approx 1.274 \text{ mm.}$$

The effective dielectric constant is estimated as

$$\epsilon_{\text{eff}} = \frac{\epsilon_r + 1}{2} + \frac{\epsilon_r - 1}{2}\left(1 + 12\frac{h}{W}\right)^{-1/2} \approx 6.1999.$$

The fringing extension length ΔL is

$$\Delta L = 0.412h\frac{(\epsilon_{\text{eff}} + 0.3)\left(\frac{W}{h} + 0.264\right)}{(\epsilon_{\text{eff}} - 0.258)\left(\frac{W}{h} + 0.8\right)} \approx 0.0221 \text{ mm.}$$

Figure 25. Photograph of the fabricated MnM-based alumina membrane with uniform microstrip patch arrays of two, four, and eight elements.

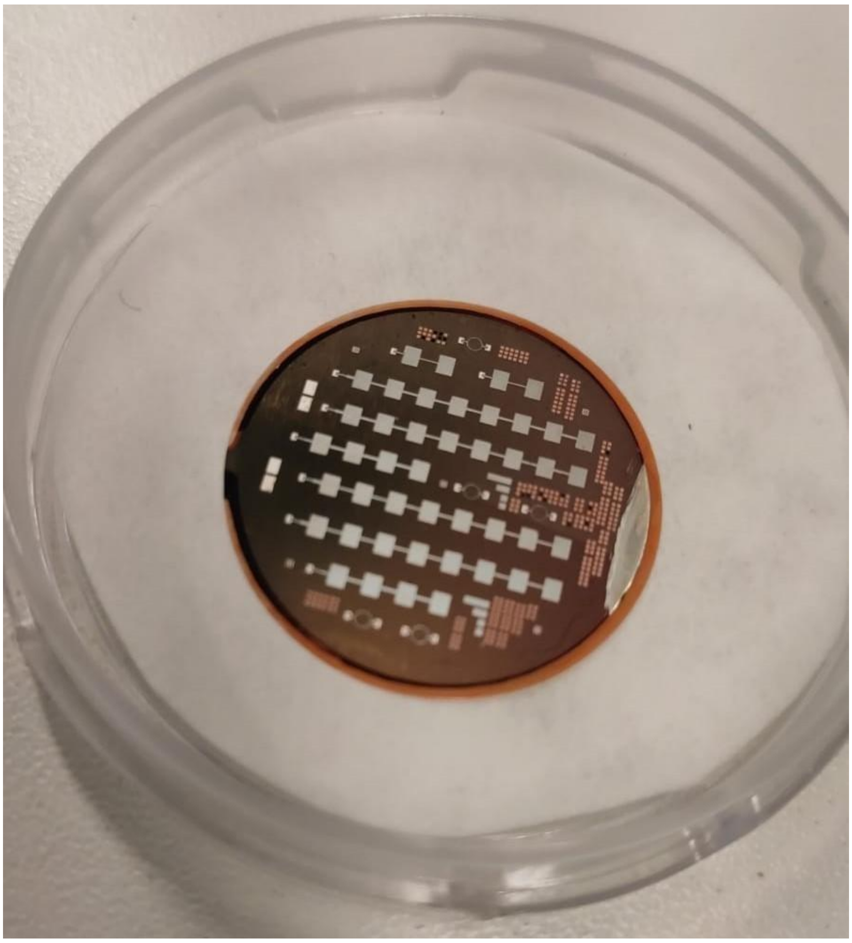

Source: Prepared by the author, 2025.

The effective length is

$$L_{\text{eff}} = \frac{c}{2f_r\sqrt{\epsilon_{\text{eff}}}} \approx 1.0040 \text{ mm.}$$

The actual patch length is

$$L = L_{\text{eff}} - 2\Delta L \approx 0.96 \text{ mm.}$$

The microstrip line was implemented on the MnM alumina substrate considered in this work was designed to achieve a characteristic impedance of Z_0 = 50 Ω, corresponding to a line width of approximately W_0 = 68.6 µm. Full-wave electromagnetic simulations performed in Ansys HFSS yielded a slightly smaller width of W_0 = 67.8 µm. Figure 27 presents a comparison between the theoretical and simulated results.

For the designed example in Section 2.2.1, a rectangular patch antenna on the MnM substrate operating at f_r = 60 GHz results in a patch width of $W \approx$ 1.274 mm and

Figure 26. Configuration of the test setup for measuring the built antenna.

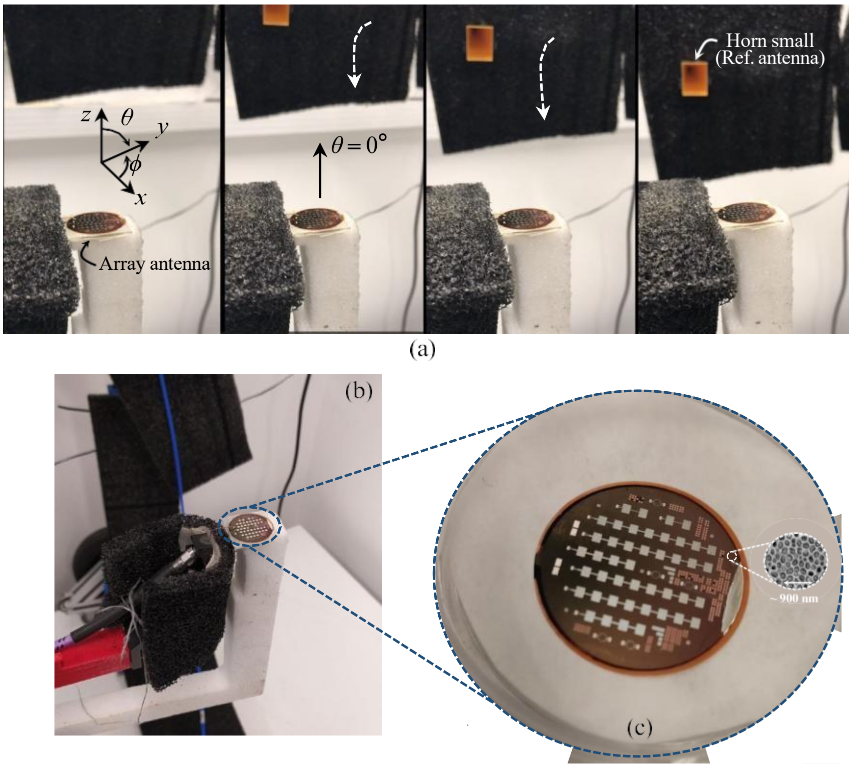

Source: Prepared by the author, 2025.

an actual length of $L \approx 0.960$ mm. The self-conductance of a single slot is expressed as

$$G_1 = \frac{0.001274}{120 \times 0.005}\left[1 - \frac{(1256.64 \times 50 \times 10^{-6})^2}{24}\right] = 0.002123 \times 0.99986 \approx 0.002123 \text{ S}.$$

The mutual conductance (eq.(2.90)) between the two radiating slots numerical evaluation gives

$$G_{12} \approx 5.034710 \times 10^{-4} \text{ S}.$$

The input edge impedance is determined as

$$Z_{edge} = \frac{1}{2\,(G_1 + G_{12})} = \frac{1}{2(0.00212 + 0.000503)} \approx 190,36\ \Omega.$$

Finally, the inset depth y_0 can be calculated using

$$y_0 = \frac{0.960 \text{ mm}}{2}\left(1 - \sqrt{\frac{50}{190.35}}\right) = 0.480 \text{ mm} \cdot 0.4875 \approx 0.234 \text{ mm}.$$

The parametric analysis performed in Ansys HFSS investigates the impact of the inset feed distance on the antenna’s input impedance. Figures 28 and 29 illustrate the real and imaginary parts of the impedance Z, respectively, as a function of frequency for various inset distances. A precise control of the inset distance is critical for achieving optimal impedance matching to a 50 Ω source. A small variation in this parameter can

Figure 27. Theoretical (eqs. (2.81) and (2.84)) and Simulated (Ansys HFSS) microstrip width vs Z_0 for $\varepsilon_r = 6.7$, $h = 50$ µm.

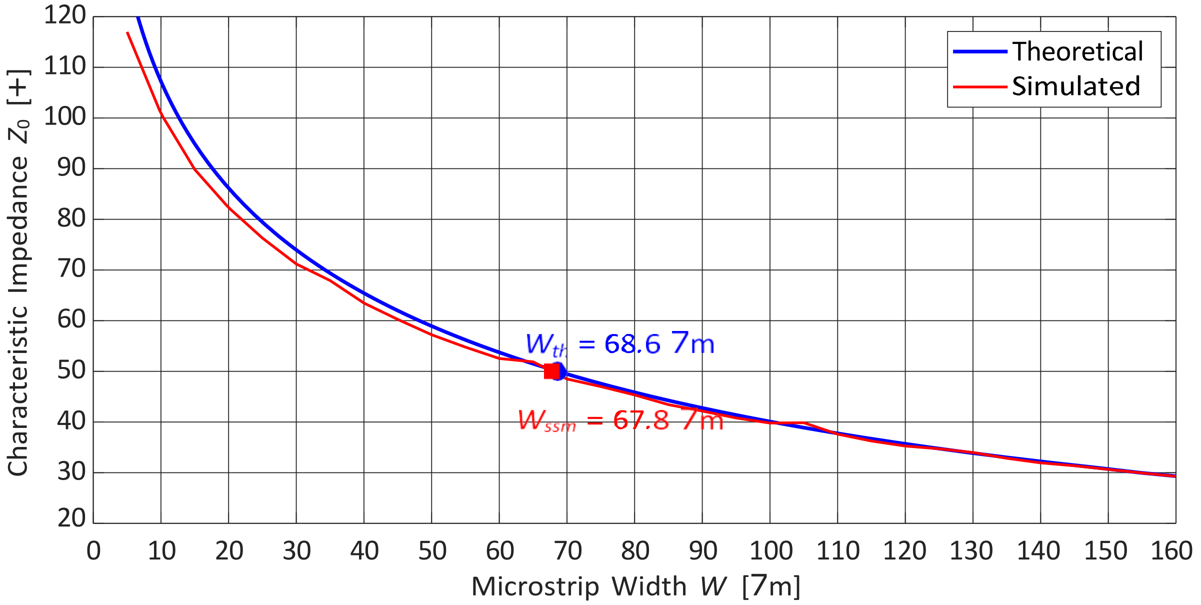

Source: Prepared by the author, 2025.

significantly alter the antenna’s matching characteristics. As observed in Figure 28, the real part of the impedance approaches the desired 50 Ω value for inset distances within the narrow range of 0.05 mm to 0.15 mm. However, the corresponding imaginary part, shown in Figure 29, does not resonate at the target frequency of 60 GHz for these same dimensions.

Conversely, the inset distances of 0.23 mm and 0.25 mm demonstrate a more favourable behaviouri. The imaginary part of the impedance for these values crosses the zero-level precisely at or very near 60 GHz, indicating a resonant condition at the operational frequency.

Figure 28. Real part of Impedance Z with parametric analysis in inset GAP distance.

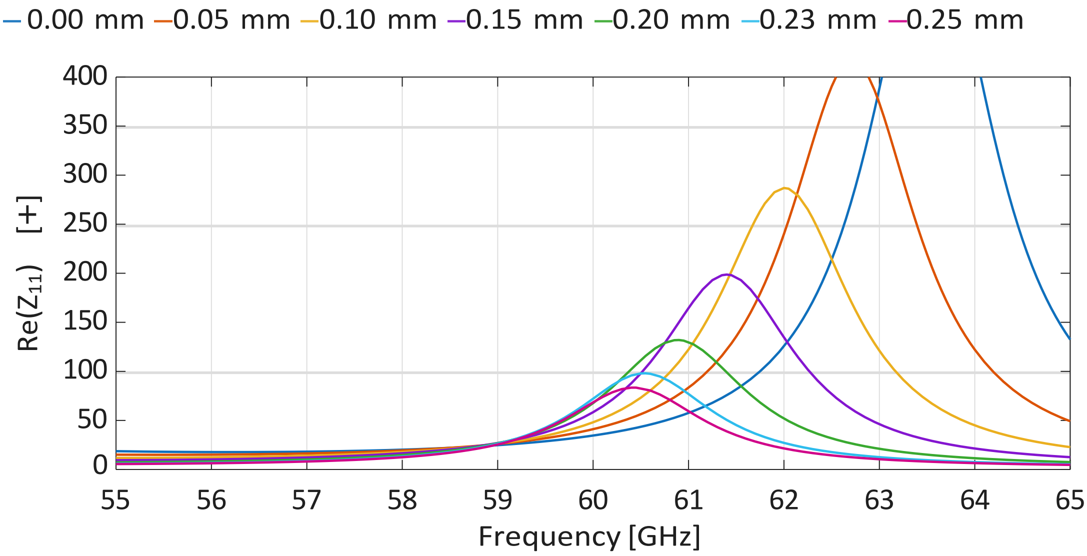

Source: Prepared by the author, 2025.

Figure 29. Imaginary part of Impedance Z with parametric analysis in inset GAP distance.

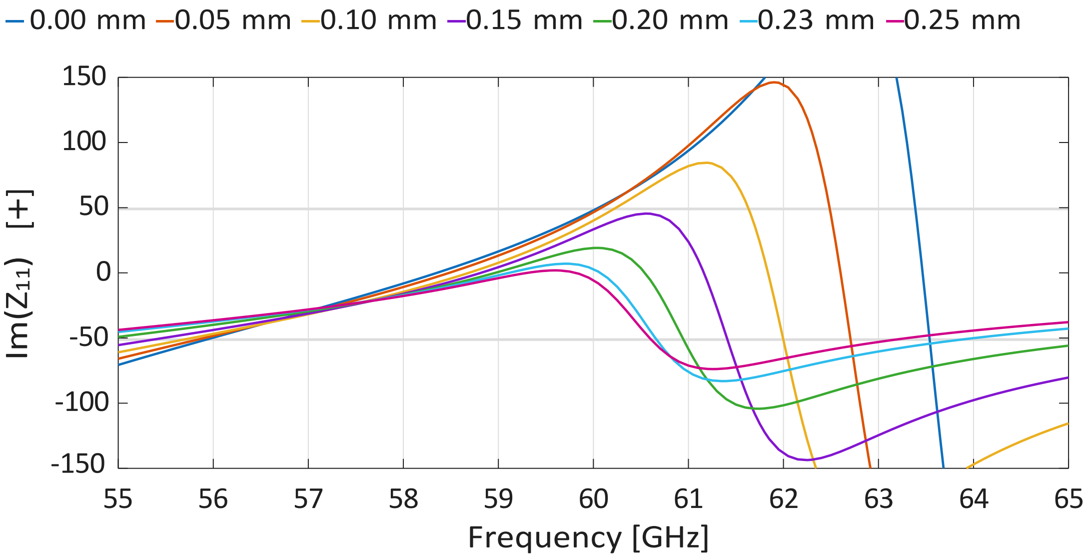

Source: Prepared by the author, 2025.

The parametric analysis of the inset feed distance also directly impacts the reflection coefficient (S_{11}) of the antenna. The optimization of this parameter is crucial for achieving the best possible impedance match at the desired frequency. As shown in Figure 30, the yellow curve, corresponding to a gap distance of 0.234 mm, demonstrates optimal matching behavior close to the central frequency of 60 GHz.

To match the feed line impedance $Z_0 = 50\ \Omega$ to the patch input resistance $Z_{edge} = 190.35\ \Omega$, a QWT is used. The characteristic impedance of the transformer is

Figure 30. Reflection coefficient with parametric analysis in inset GAP distance.

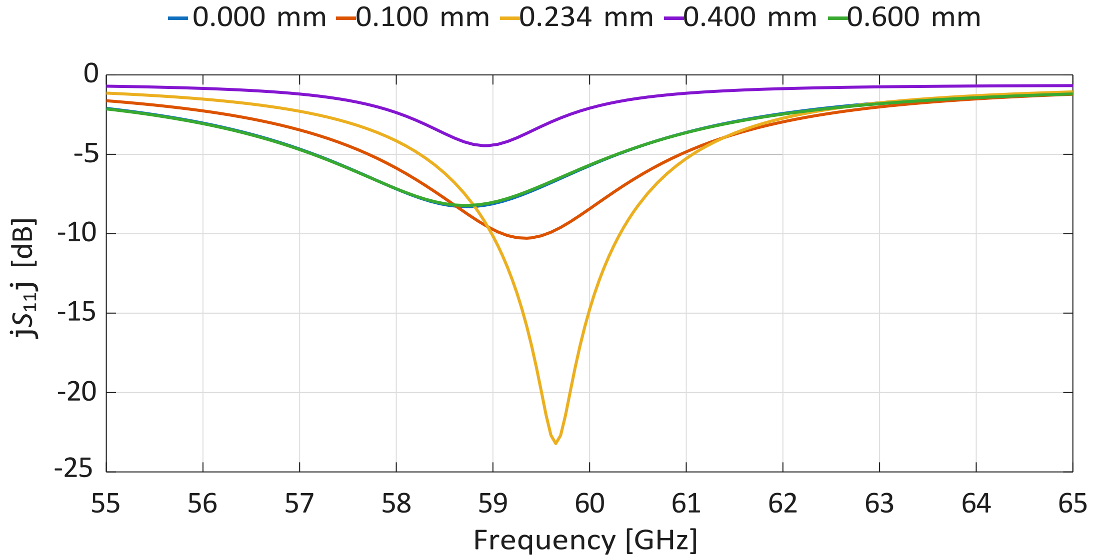

Source: Prepared by the author, 2025.

$$Z_q = \sqrt{Z_0 Z_{edge}} = \sqrt{50 \times 190.35} \approx 97.57\ \Omega. \tag{3.1}$$

The physical length of the QWT is

$$L_q = \frac{\lambda_g}{4} = \frac{c}{4 f_r \sqrt{\varepsilon_{\text{eff}}}} = \frac{3 \times 10^8}{4 \times 60 \times 10^9 \sqrt{6.1999}} \approx 0.000502 \text{ m} = 0.502 \text{ mm}. \tag{3.2}$$

Based on the previous analysis, the final dimensions of the rectangular microstrip antenna with a QWT are summarized in Table 9. The initial step in the design process was to optimize the impedance matching between the antenna and the feed line, similar to the methodology described in the previous subsection.

A parametric analysis was performed on the width of the QWT to determine the optimal geometric parameters for achieving the best performance. Unlike the previous analysis, which focused on the inset feed distance, this study specifically investigates the effect of the QWT width.

As illustrated in Figure 31, the real and imaginary part of the input impedance Z are presented as a function of frequency. The QWT parametrization is instrumental in determining the impedance matching characteristics. This behavior is also dependent on the feed line width. The optimal QWT width is found to be in the interval of 50 μm to 70 μm, where the antenna exhibits a resonance region within the desired 60 GHz frequency range.

In Figure 32, the imaginary part of the input impedance Z is displayed. For the same parametric values (50 μm to 70 μm), the imaginary part of the impedance crosses the zero level, confirming the resonant condition near 60 GHz. This optimization, based

Table 9. Output Parameters of the Rectangular Patch Antenna

Parameter	**Symbols**	**Value**
Microstrip Charac. Imped.	Z_0	50 Ω
Microstrip Width	W_0	67.8 µm
Rectangular Patch Width	W	1.274 mm
Rectangular Patch Length	L	0.96 mm
Effective Dielectric	ε_{eff}	6.1999
Extension Length	ΔL	0.0221 mm
Effective Length	L_{eff}	1.0040 mm
Edge Impedance	Z_{edge}	190.36 Ω
Inset Depth	y_0	0.234 mm
Transformer Impedance	Z_q	97.57 Ω
Transformer Length	L_q	0.502 mm
Transformer Width	W_q	12.40 µm

Source: Prepared by the author, 2025.

on the QWT width, directly leads to a significant improvement in the reflection coefficient, allowing for the identification of the most suitable geometric dimensions.

Figure 31. Impedance Z Real and Imaginary parts with parametric analysis in QWT width.

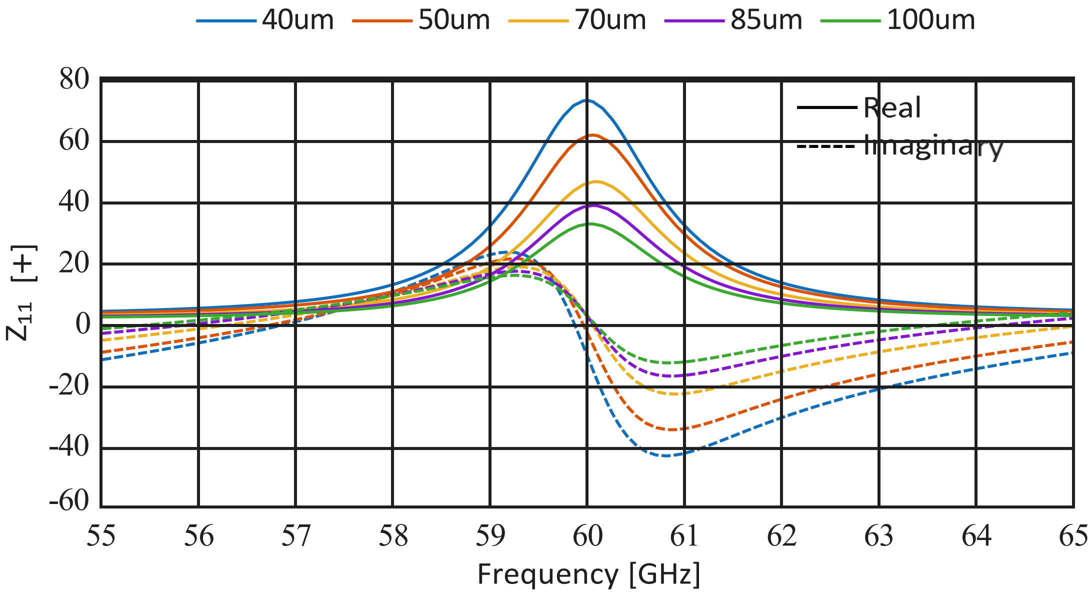

Source: Prepared by the author, 2025.

Building upon the initial model, two additional single-element antenna configurations were designed to optimize performance: one using a PAD probe and another incorporating a QWT in the feed line. The primary objective of these variations was to assess the impact of these impedance-matching techniques on the antenna's overall perfor-

Figure 32. Reflection coefficient with parametric analysis in QWT width.

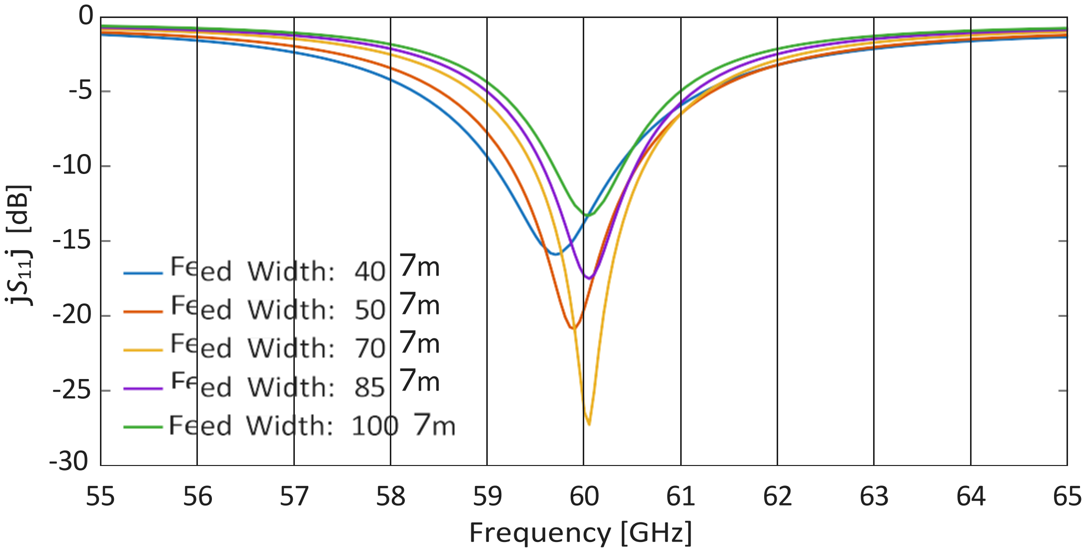

Source: Prepared by the author, 2025.

mance. Figures 33 and 34 show the simulated input impedance and reflection coefficient of the rectangular microstrip antenna element.

Figure 33. Impedance Z for simple rectangular microstrip antenna.

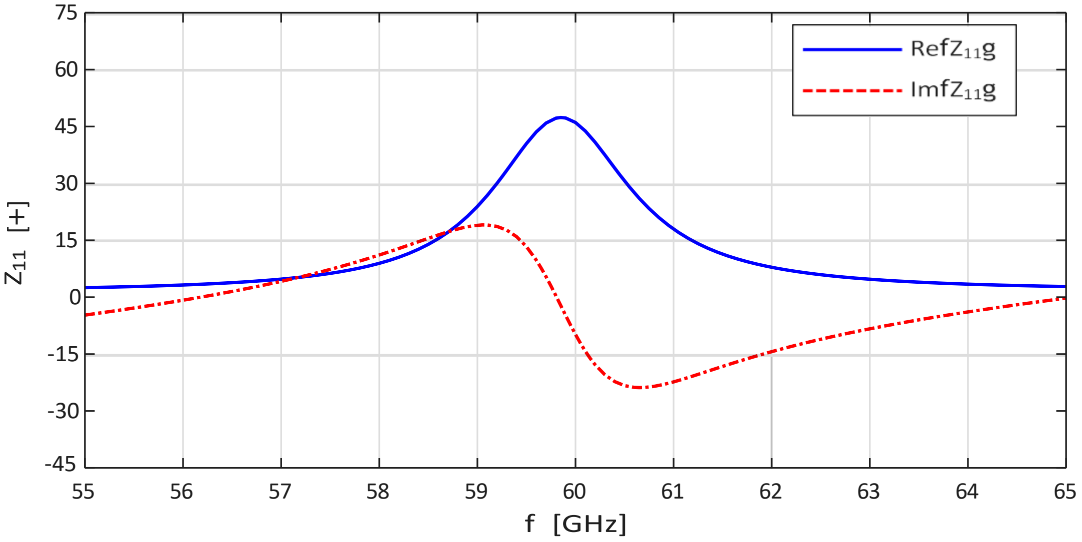

Source: Prepared by the author, 2025.

Figure 34. Reflection coefficient for simple rectangular microstrip antenna.

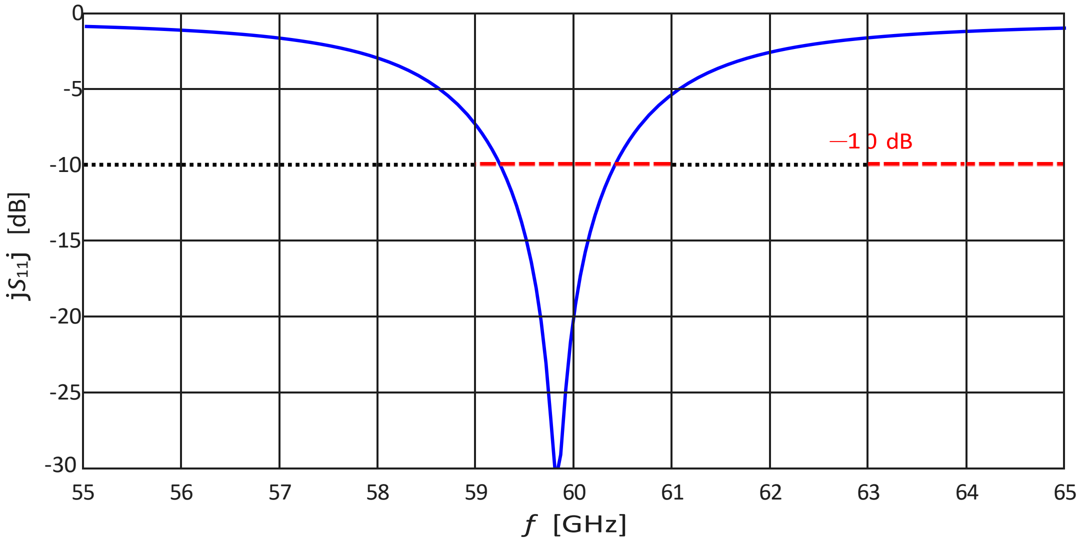

Source: Prepared by the author, 2025.

Figure 35 compares the initial simulation results for all three configurations. The direct 50 Ω transmission line and the PAD-probed configurations exhibited similar results, indicating that the PAD does not significantly affect the antenna's performance. The optimized design, utilizing a QWT, demonstrates the lowest reflection coefficient among the single-element configurations. The result presented in Figure 35 shows the final simulated S_{11} for the single radiating element.

Figure 35. Comparative between microstrip antenna with Direct Transmission Line, PAD probe, QWT.

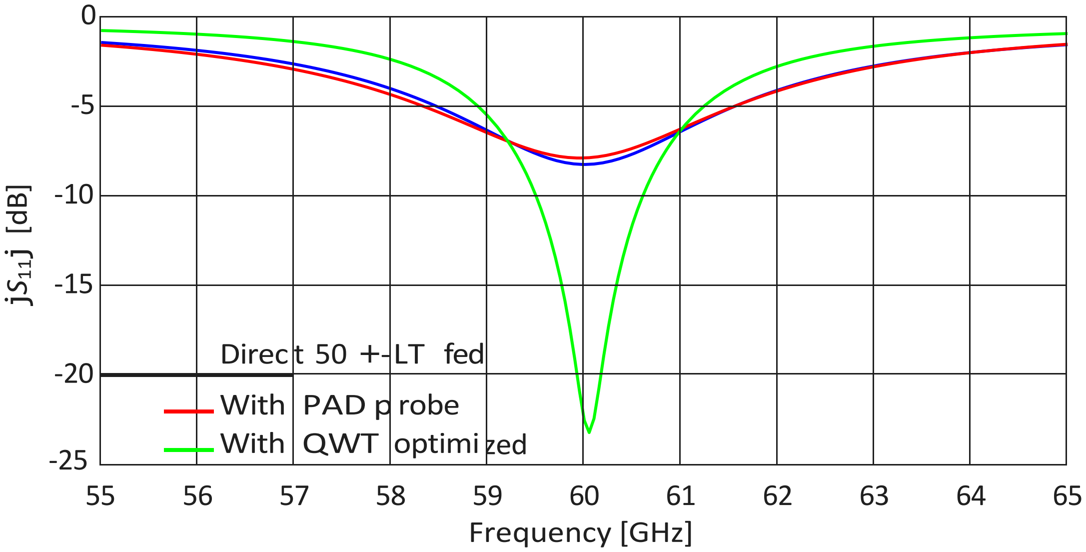

Source: Prepared by the author, 2025.

The radiation pattern of the antenna, depicted in Figure 36, shows that the main lobe in the E-plane is shifted from the boresight axis (90°). This asymmetry and the

Figure 36. Radiation Pattern for ±90°.

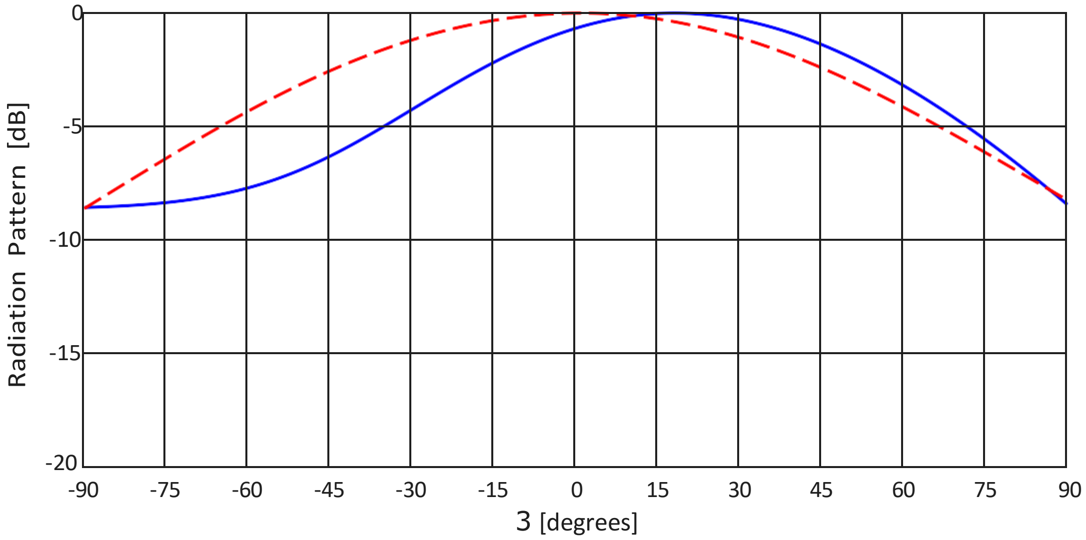

Source: Prepared by the author, 2025.

angular displacement toward to 45°, are attributed to the coupling aperture, which acts as a secondary radiating source. In aperture-coupled microstrip antennas, the radiating slot on the ground plane behaves as a dipole radiator.

3.1.2 Uniform Array with Two Elements

Now, starting the array design, one more element is inserted to the previous model to generate the first array proposed, with two series elements, as we see in the Figure 37. The distance used between the elements is calculated with 3.3.

Figure 37. Designed two elements array in Ansys HFSS.

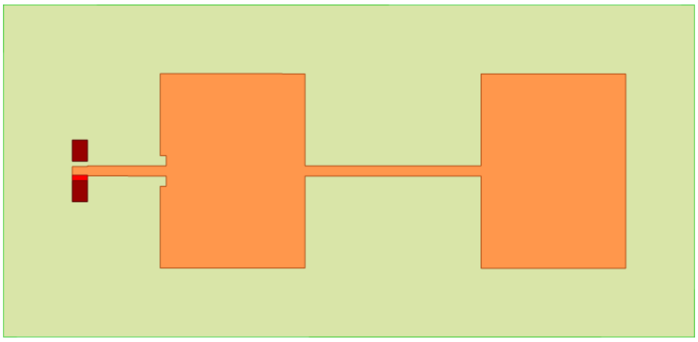

Source: Prepared by the author, 2025.

$$d = \frac{\lambda}{2} \tag{3.3}$$

The value is equivalent to half a wavelength, enabling operation in the same phase in both elements of the array and improving impedance matching. In other words, the wave can travel along the array, with a new period beginning at the start of each element.

Figure 38. Imaginary part of Impedance Z with parametric analysis in inset GAP distance.

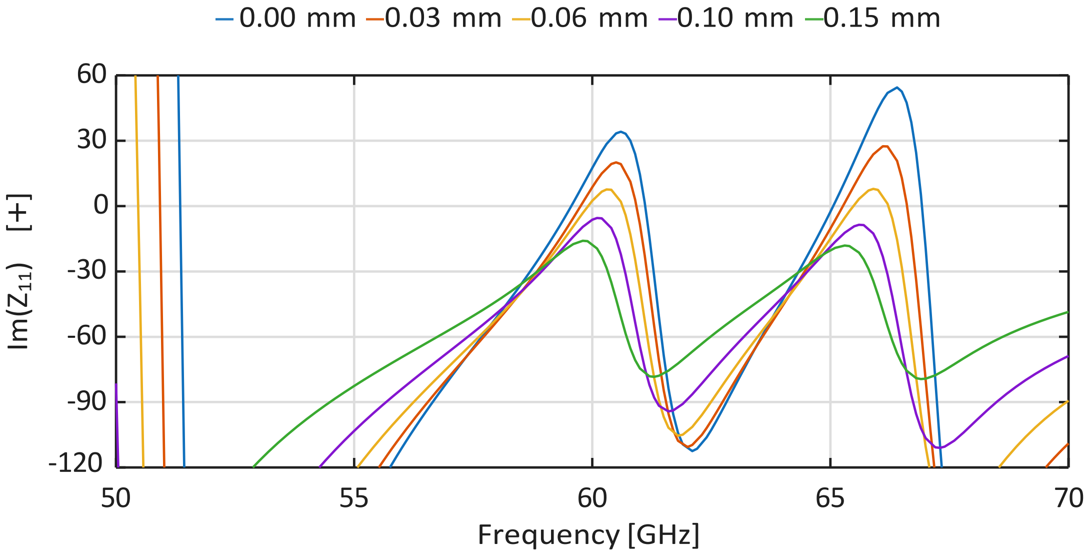

Source: Prepared by the author, 2025.

As the number of radiating elements in the array increases, an interesting behavior is presented in the imaginary part of the input impedance demonstrates a progressive shift in its zero-crossing point toward higher frequencies. This behavior is evident in Figure 38, where each curve corresponds to a different value of inset gap distance. The observation indicates a direct relationship between the array size and the gap size adopted.

Further analysis reveals that the best value for the gap size is 0.06 mm, that yields the imaginary part of the impedance closest to zero at the target frequency of 60 GHz. This result is crucial as it signifies an optimal resonant condition for the array.

Complementing this finding, Figure 39 shows the real part of the input impedance, which presents a peak value in the ideal impedance value of 50 Ω, precisely at 60 GHz. This simultaneous occurrence of a real impedance peak and an imaginary impedance zero-crossing confirms that the array design is fully optimized, providing an excellent impedance match at the operating frequency with gap size in 0.06mm.

Before the final inset distance was determined, reflection coefficient S_{11} was analysed to validate the selected inset gap. Figure 40 illustrates how variations in this parameter directly impact the antenna's operational characteristics, with the objective of achieving optimal impedance matching at the desired frequency. Similar to the impedance plots, the analysis of the S_{11} curves shows the appearance of multiple resonance zones across the frequency spectrum. This behavior is directly linked to the parametric variations adding one radiating element in the array, highlighting the sensitivity of the antenna's performance to those parameters. With this additional analysis, it is possible to confirm that an inset-distance gap of 0.06 mm yields the most favorable performance. This condition

Figure 39. Real part of Impedance Z with parametric analysis in inset GAP distance.

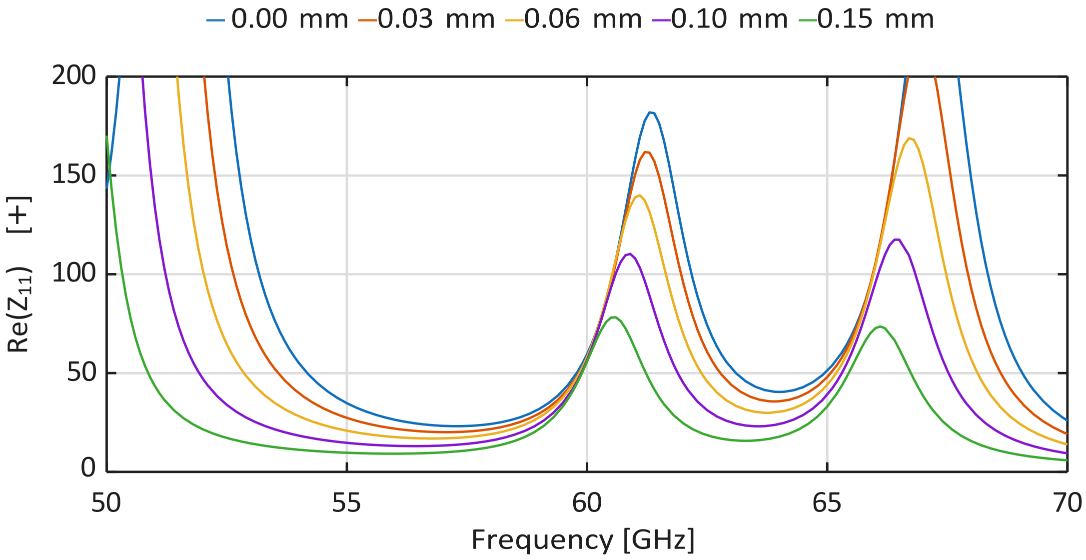

Source: Prepared by the author, 2025.

corresponds to the yellow curve, associated with a 50μm offset.

Figure 40. Reflection coefficient with parametric analysis in inset GAP distance.

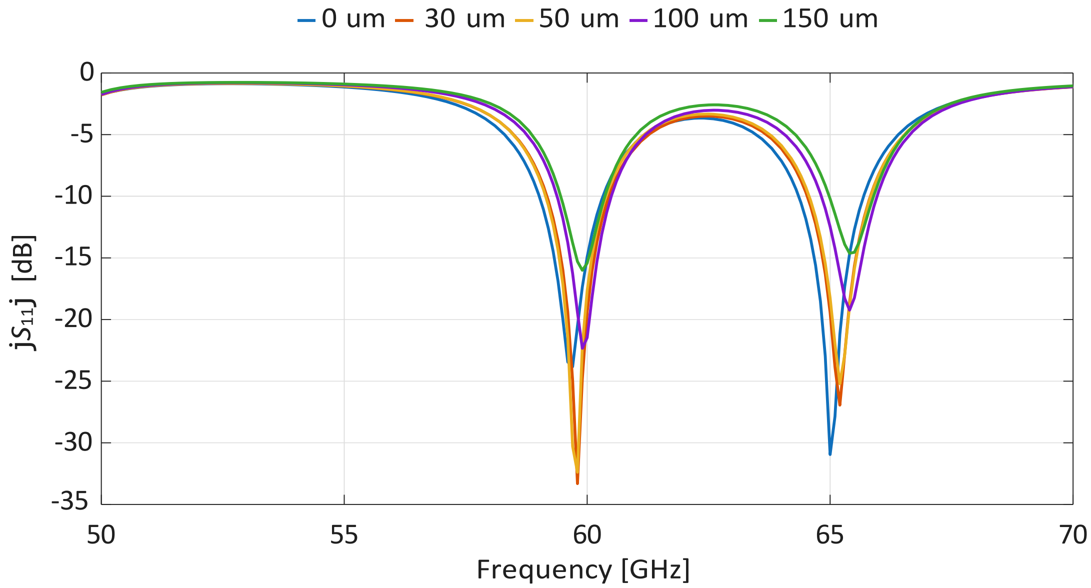

Source: Prepared by the author, 2025.

Then, Figures 41 and 42 show the final results reached after find the best measures values granted by parametrizations.

With the new model design, Figure 43 illustrate the first calculated reflection coefficient in comparison with the fabricated two elements array. The results obtained in the fabricated device with the QWT was as expected in the simulations.

Figure 44 shows the normalized directivity radiation pattern of the array. The

Figure 41. Reflection coefficient for two antenna array.

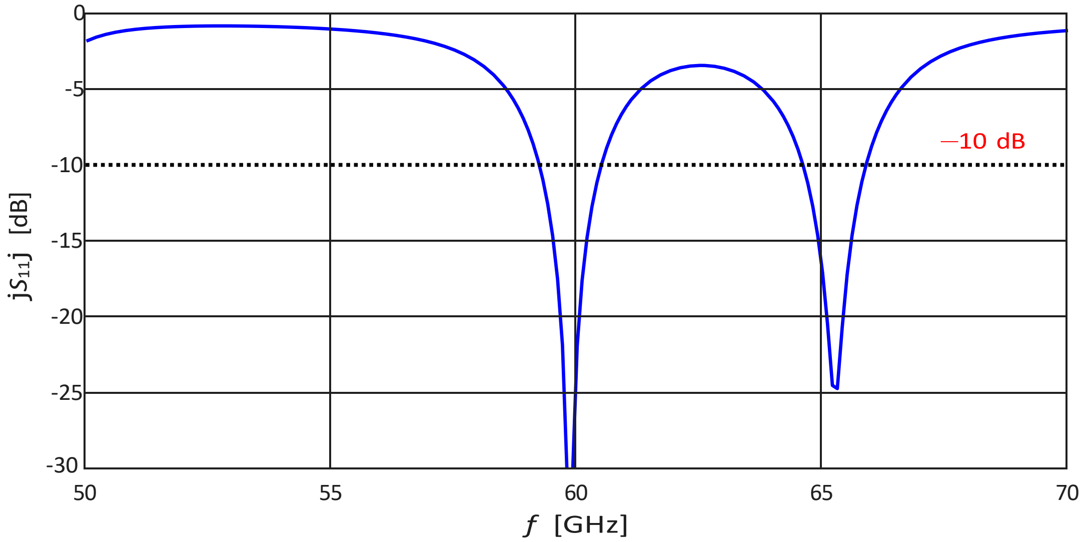

Source: Prepared by the author, 2025.

Figure 42. Impedance Z for two antenna array

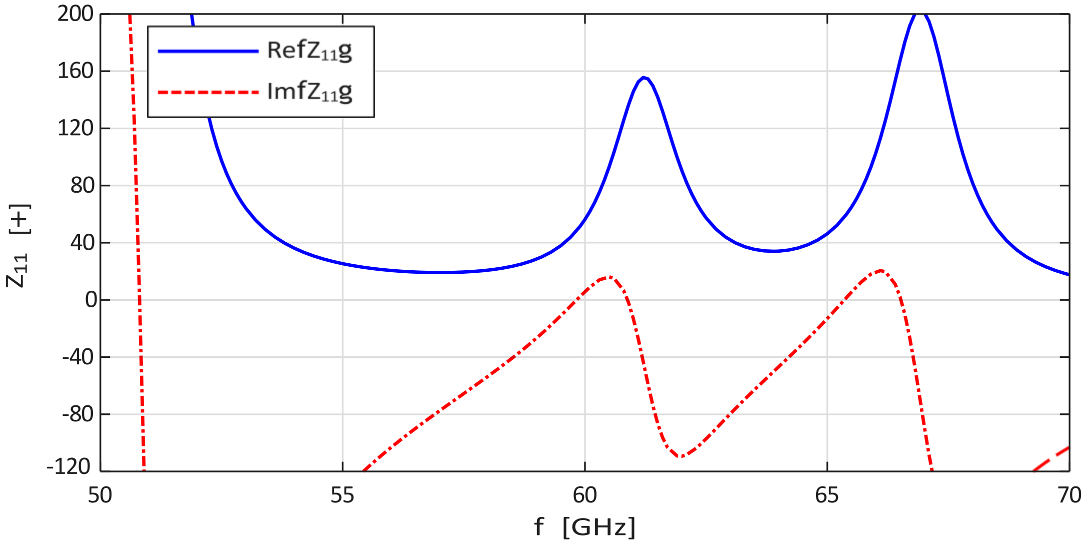

Source: Prepared by the author, 2025.

H-plane pattern is represented by the blue curve, while the E-plane pattern is shown in red, and the measured results are shown in dashed. The primary radiation is directed towards the broadside, as indicated by the main lobe at 0°. However, the pattern clearly shows that a portion of the radiated energy is dissipated in directions other than the main lobe. This is evident from the presence of side lobes (for the E and H planes) and potential grating lobes. The existence of these lobes is a direct consequence of the periodic spacing of the array elements and their individual radiation characteristics.

The fabricated device's measured performance exhibits excellent agreement with the simulation results. The experimental radiation behavior confirms the predicted charac-

Figure 43. Measured and simulated reflection coefficient for two elements array.

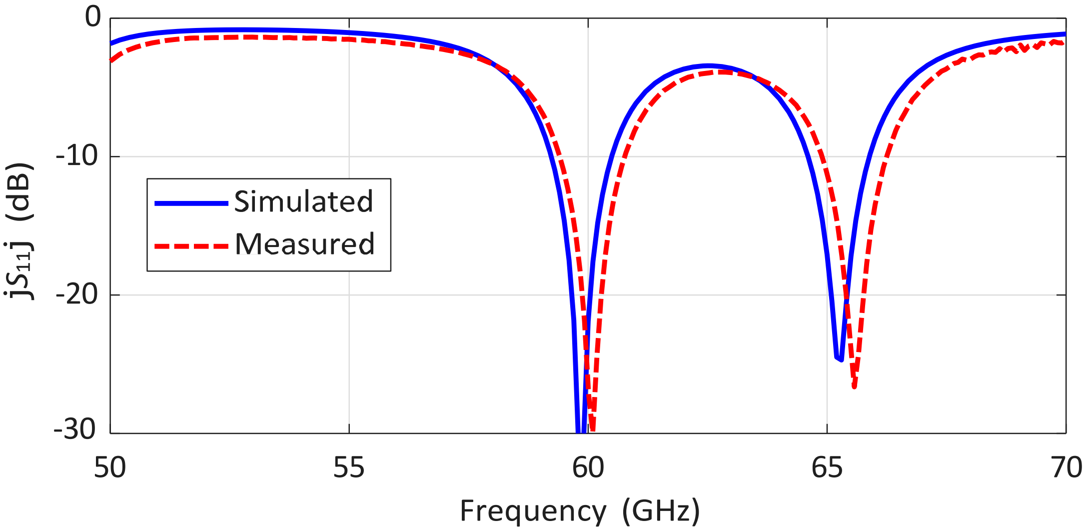

Source: Prepared by the author, 2025.

Figure 44. Radiation Pattern for ±90° in plan E and H for two antenna array.

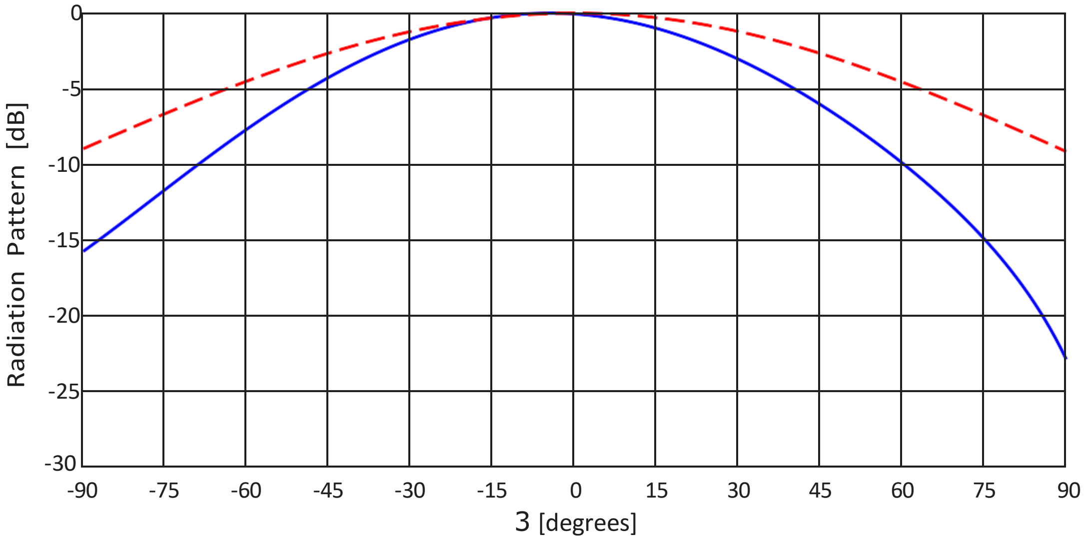

Source: Prepared by the author, 2025.

teristics, validating the effectiveness of the design methodology. Finally, Fig. 45 presents the array directivity as a function of frequency, reaching approximately 7 dB at the center frequency.

3.1.3 Uniform Array with Four Elements

Continuing the array development, the number of series-fed elements was increased to four. The total length of the designed array elements is now 7.688 mm. As depicted in next figures, the simulated input characteristics ($|S_{11}|$, Z_{11}) of the uniform 4-element series-fed microstrip array antenna are presented.

Figure 45. Simulated directivity of the uniform 2-element series-fed microstrip array antenna as a function of frequency.

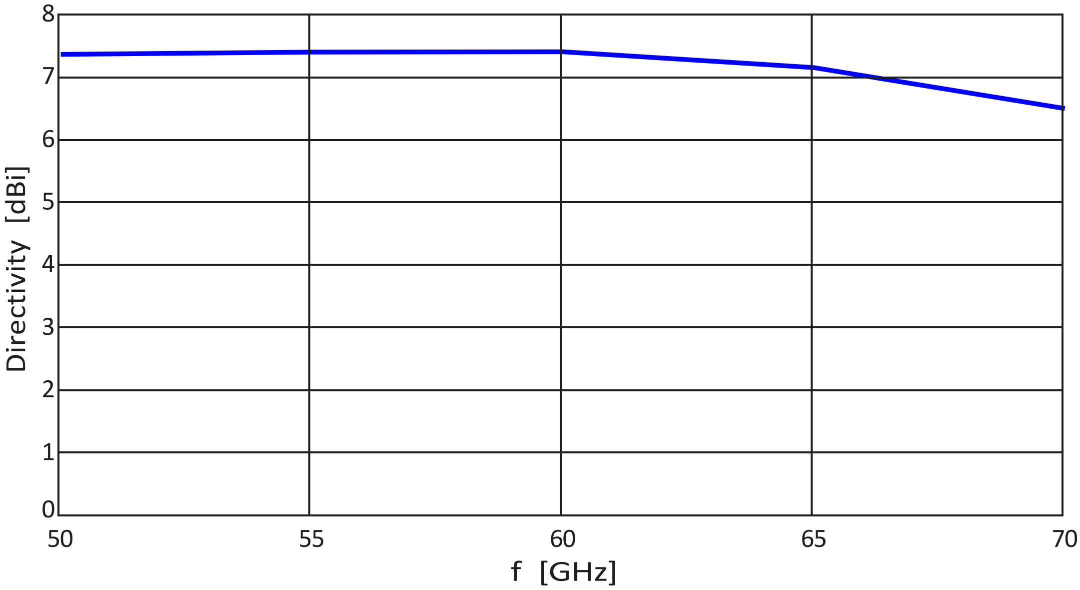

Source: Prepared by the author, 2025.

Figure 46. Real part of Impedance *Z* with parametric analysis in QWT width.

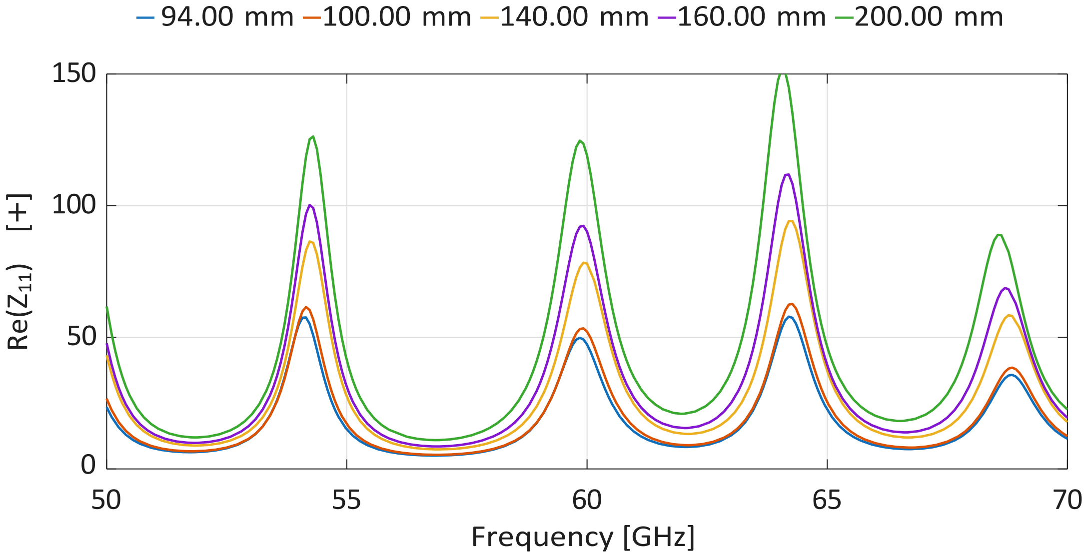

Source: Prepared by the author, 2025.

Through additional simulations and parametric analysis, it is possible to manipulate the resonance in the frequency spectrum to optimize the system's performance based on the necessary requirements. Figures 46 and 47 shows the real and imaginary parts of the input impedance Z, respectively, for a parametric analysis of the QWT width. As the QWT width increases, the real part of the impedance reaches higher values, moving significantly away from the ideal 50 Ω impedance matching point. By examining both figures, the most suitable behavior is observed for values within the 94–100 mm interval.

Figure 47. Imaginary part of Impedance Z with parametric analysis in QWT width.

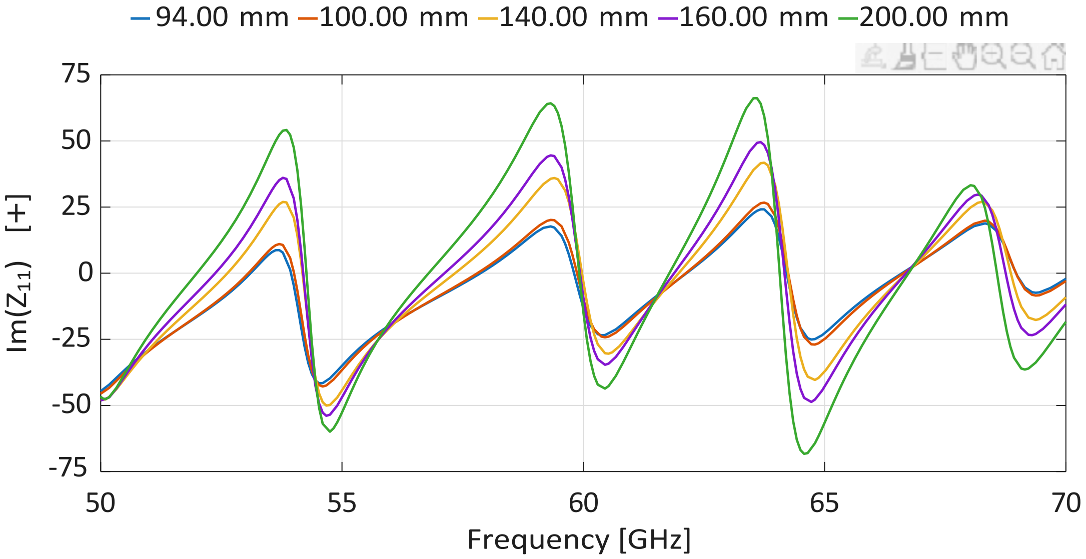

Source: Prepared by the author, 2025.

Figure 48. Four-element array QWT_W reflection coefficient parametrization.

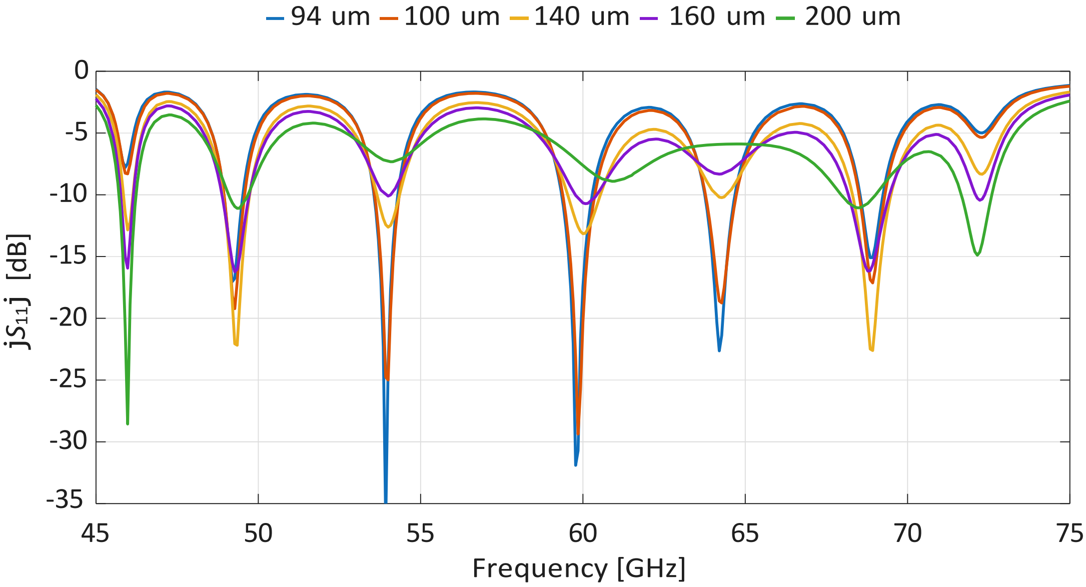

Source: Prepared by the author, 2025.

To define the best measure, this parametric analysis of the QWT width also significantly impacts the reflection coefficient S_{11}. Similar to previous cases, varying the QWT width provides a direct means to control the magnitude of the reflection coefficient, as shown in Figure 48. The S_{11} behavior observed in the two-element array is repeated here. However, with four elements, the array now exhibits more than four distinct resonance zones within the 60 GHz spectrum. Here, it can be observed that the blue curve corresponding to the 94-µm configuration provides the best performance, as it minimizes the reflection coefficient within the 55–65 GHz frequency range.

The parametric analysis of the transmission line width, illustrated in Figure 49, demonstrates its effect on the array's resonant frequency. Differently from the QWT width parametrization, increase the transmission line width causes a notable shift of the operational frequency toward higher values, specifically into the 50 GHz and 55 GHz zones, possibiliating move the antenna resonance zone to configure the central frequency operation, as well. In this case, increasing the value of W_t produces a more suitable response by positioning the reflection coefficient near the 60-GHz region; thus, the optimal value is 130 μm.

Figure 49. Four-element array W_l reflection coefficient parametrization.

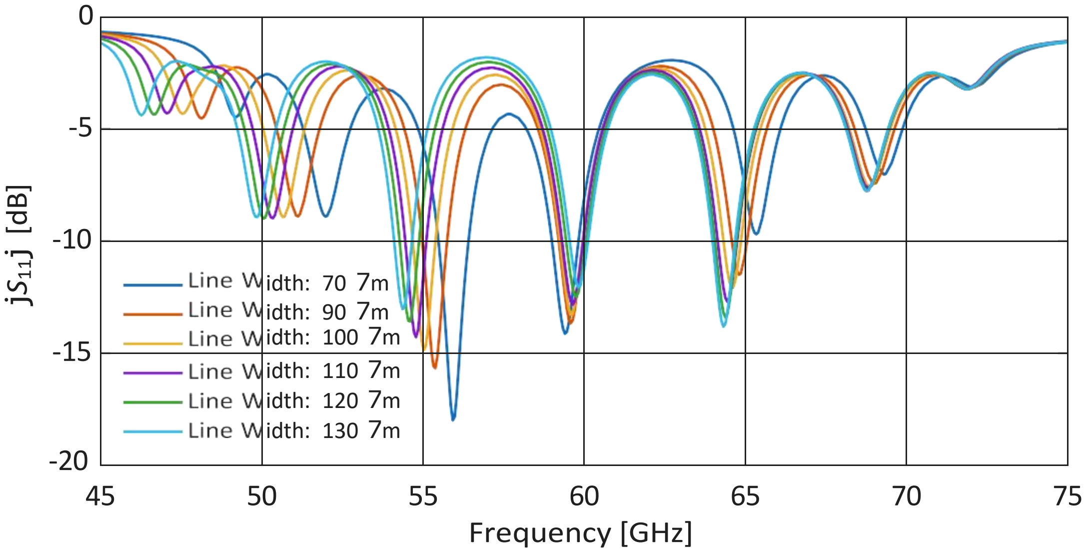

Source: Prepared by the author, 2025.

Figure 50 show the final Impedance Z for this array. And in the next Figure 51, final S_{11} of the optimized four-elements array is shown, with a comparative with the final fabricated device. The measurement indicate that the simulation value expected was maintained in the constructed device. The reflection coefficient exhibits an impedance bandwidth (for −10 dB) in several regions between 55 GHz and 65 GHz.

The simulated and measured E-plane radiation patterns for the uniform four-element series-fed microstrip array are presented in Fig. 52. The blue curve present the H plan. Note that the main lobe is oriented toward broadside, and the measured SLL is approximately −13 dB. The discrepancies observed between the simulated and measured results are primarily attributed to measurement uncertainties and limitations in the experimental setup.

Additionally, Fig. 54 presents the array directivity magnitude as a function of frequency. The results indicate the presence of directivity peaks within the 50–70 GHz band, with a maximum value of approximately 10 dB at the center frequency.

Figure 50. Impedance Z Real and Imaginary parts for four-element array.

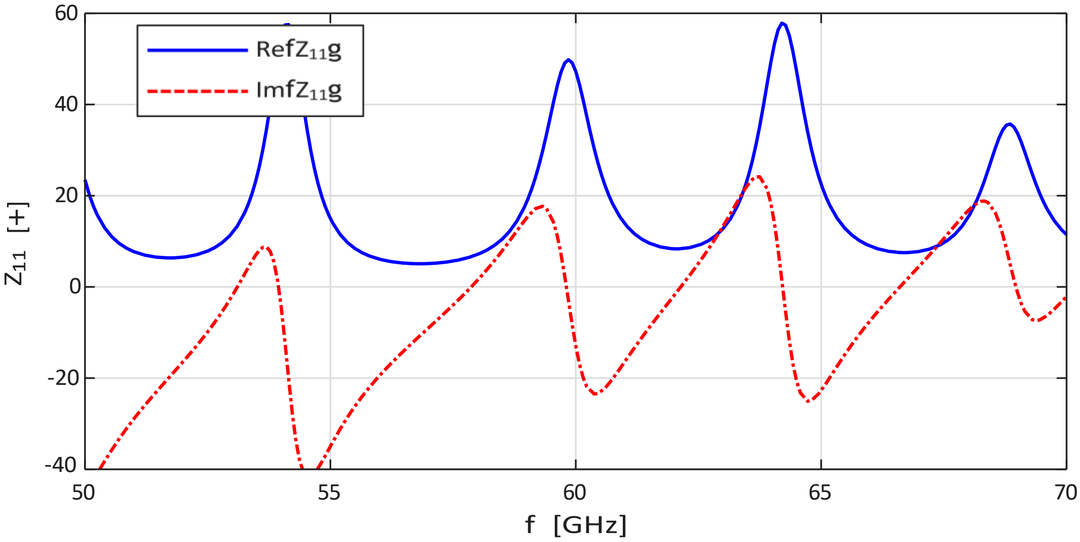

Source: Prepared by the author, 2025.

Figure 51. Measured and simulated reflection coefficient for four-element array.

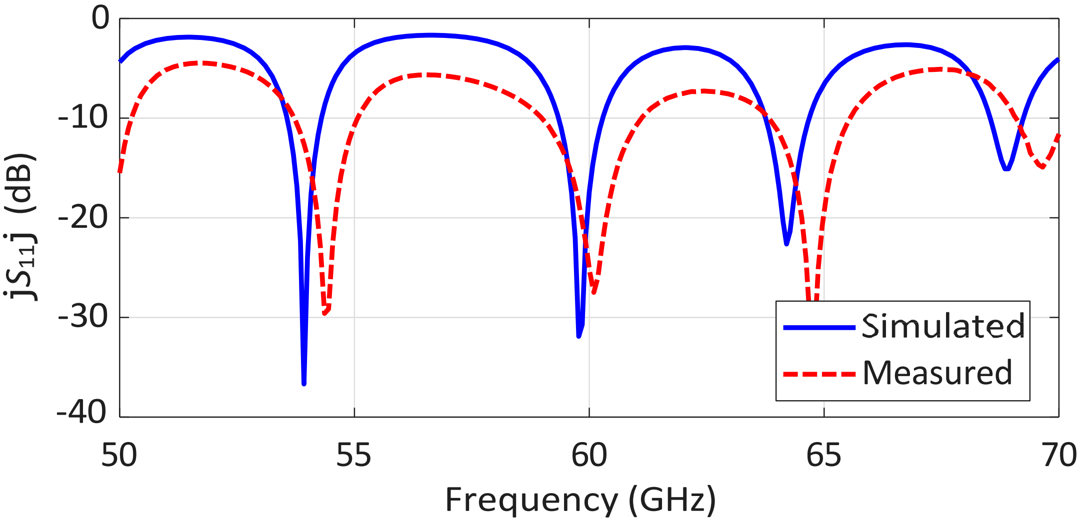

Source: Prepared by the author, 2025.

3.1.4 Uniform Array with Eight Elements

The final device designed, a series-fed antenna array with eight patch elements is developed and fabricated on a MnM interposer, with 15.37 mm of series patch length, all of them operating in the same phase, during the impedance matching applied using a QWT.

Through software simulations, and the parametric analysis applied previously, the S_{11} and Z impedance, shown in Figure 55 and 56, respectively, are optimized to coverage to the expected operation characteristics. It is notable that a largest number of resonance zones in the interval of 50 GHz until 70 GHz is obtained.

Figure 52. Radiation Pattern in plan E and H.

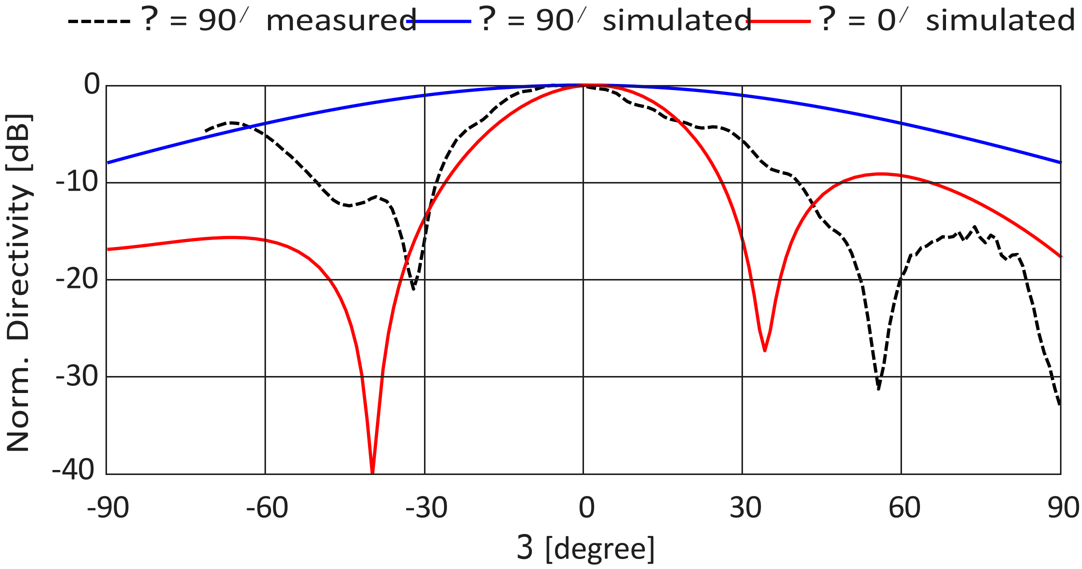

Source: Prepared by the author, 2025.

Figure 53. Radiation Pattern in plan E and H.

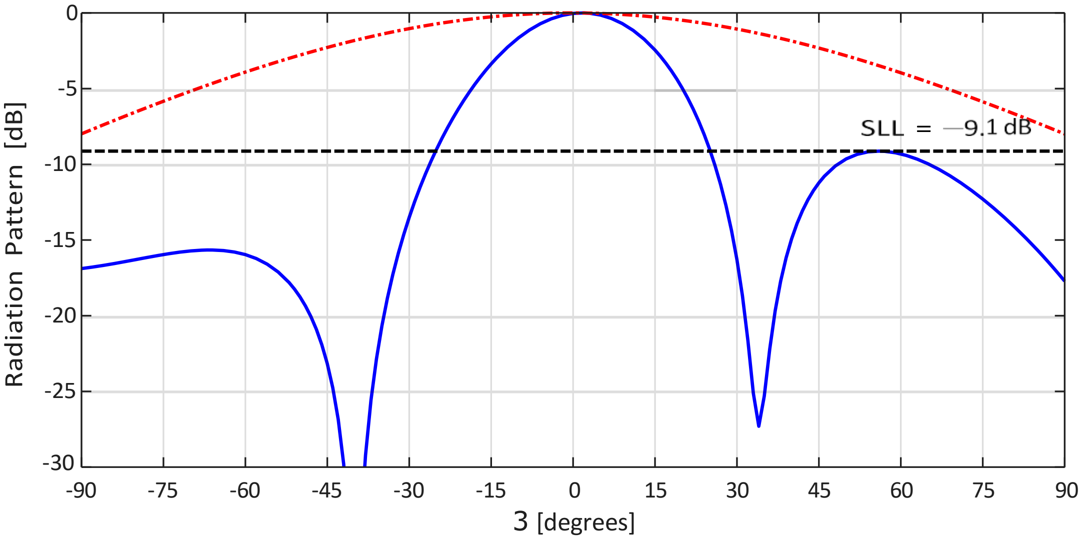

Source: Prepared by the author, 2025.

Figure 55 shows the real and imaginary parts of the input impedance (Z_{11}) with parametrization of QWT width. The best results are between 160 μm and 180 μm. While the imaginary part varies from about −40 Ω to 50 Ω, crossing zero multiple times, indicating the presence of several resonant conditions within the operating band.

Same parametrization is applied for S_{11}, and the array performance, can be optimized to exhibits an impedance bandwidth (for −10 dB), selecting values between 140 μm and 200 μm for the QWT width, as shown in Figure 56. The optimal value corresponds to the green curve, which represents $W_q = 200$ μm.

Figure 54. Simulated directivity of the uniform 4-element series-fed microstrip array antenna as a function of frequency.

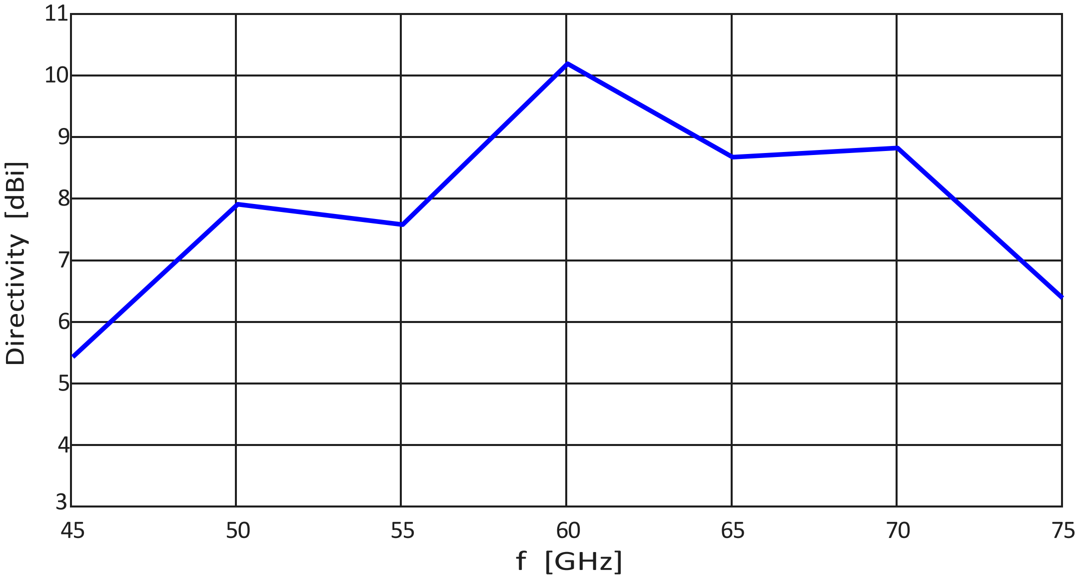

Source: Prepared by the author, 2025.

Figure 55. Impedance Z Real and Imaginary parts with parametric analysis in QWT width.

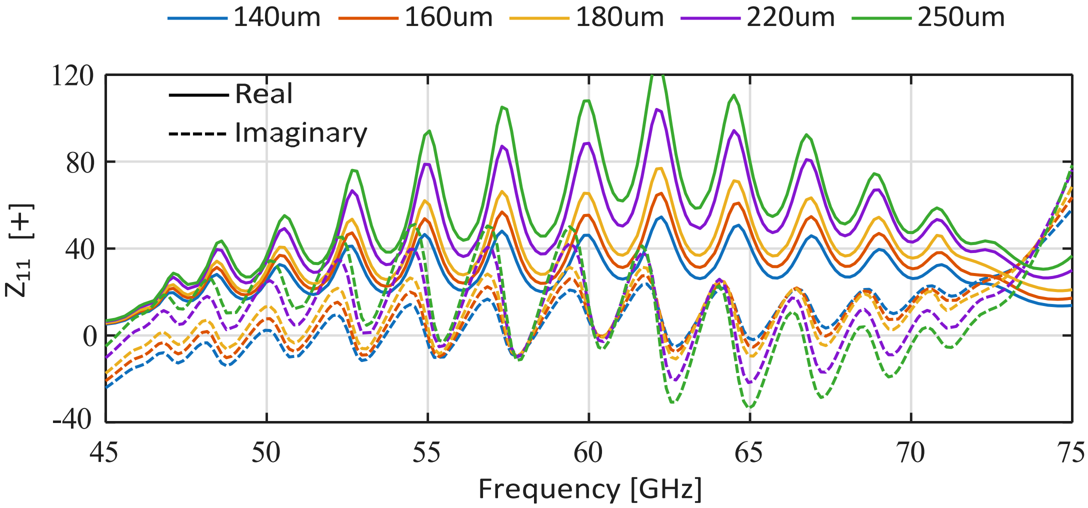

Source: Prepared by the author, 2025.

After the parametrizations the final measures adopted results in the Impedance Z and reflection coefficient displayes in Figures 57 and 58.

Then, the optimized eight-elements array reach an impedance bandwidth of approximately 22 GHz (50 GHz - 70 GHz), as the comparative curves of the simulated and measured results, present in Figure 59. It is important to note that while a wide impedance bandwidth is achieved, the array's effective operational bandwidth is limited by the gain performance. The maximum gain is concentrated in the main lobe at a specific frequency,

Figure 56. Eight-element array QWT_W reflection coefficient parametrization.

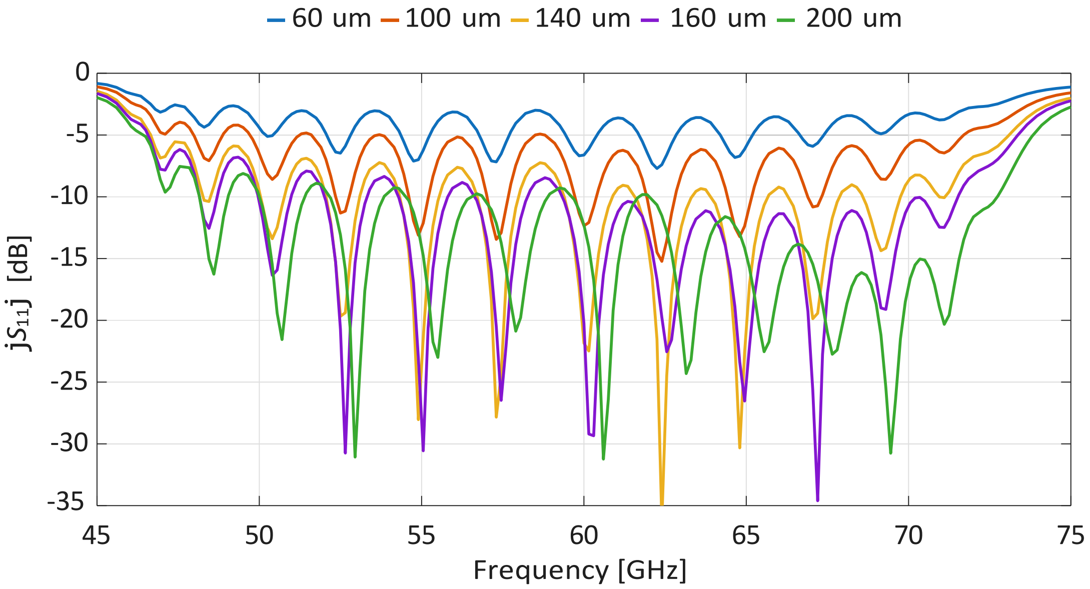

Source: Prepared by the author, 2025.

Figure 57. Impedance Z Real and Imaginary parts for eight-element array.

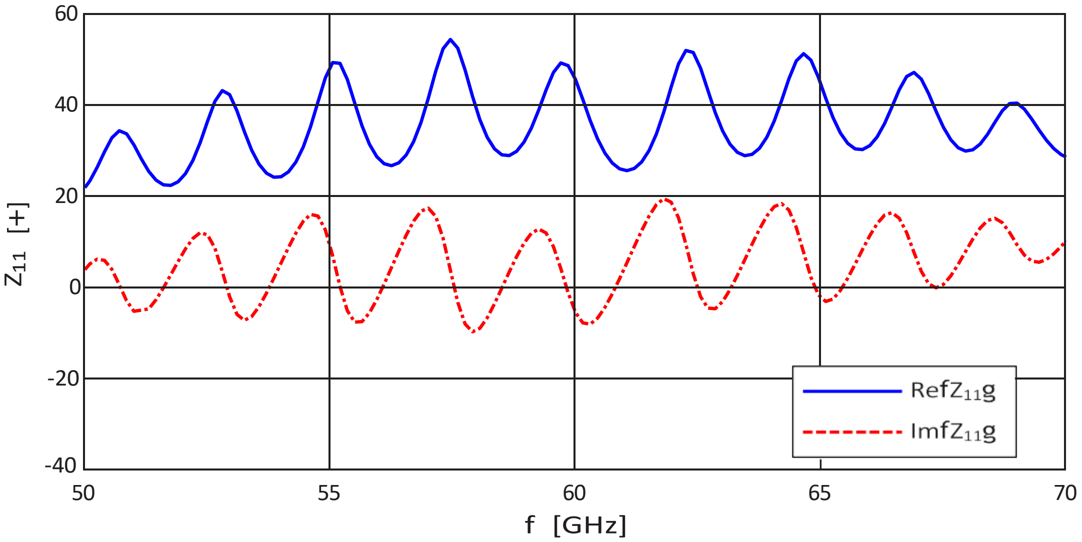

Source: Prepared by the author, 2025.

and it progressively decreases at frequencies further from this central point. Additionally, along this bandwidth, S_{11} overtake the ideal -10 dB, like in 48 GHz, 54 GHz, and 60 GHz.

In terms of directivity magnitude, Figure 60 shows that the eight-element array exhibits approximately 13 dB of directivity at the center frequency. This result indicates an incremental increase of about 3 dB with each doubling of the number of radiating elements, consistent with the behavior observed when comparing the two-, four-, and eight-element arrays.

The radiation pattern of the E-plane for the uniform 8-element series-fed microstrip

Figure 58. Reflection coefficient for eight-element array.

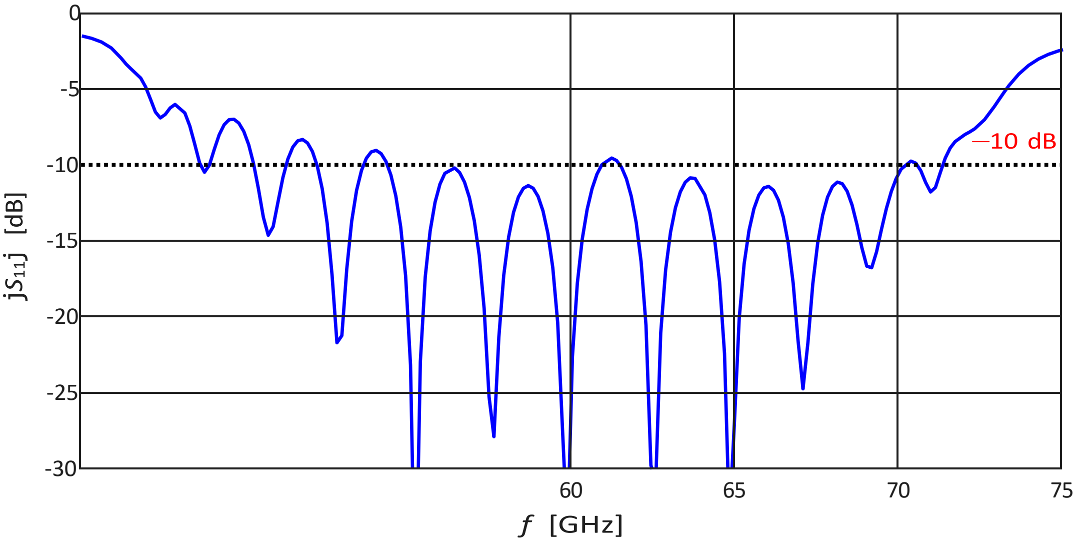

Source: Prepared by the author, 2025.

Figure 59. Measured and simulated reflection coefficient for eight-element array.

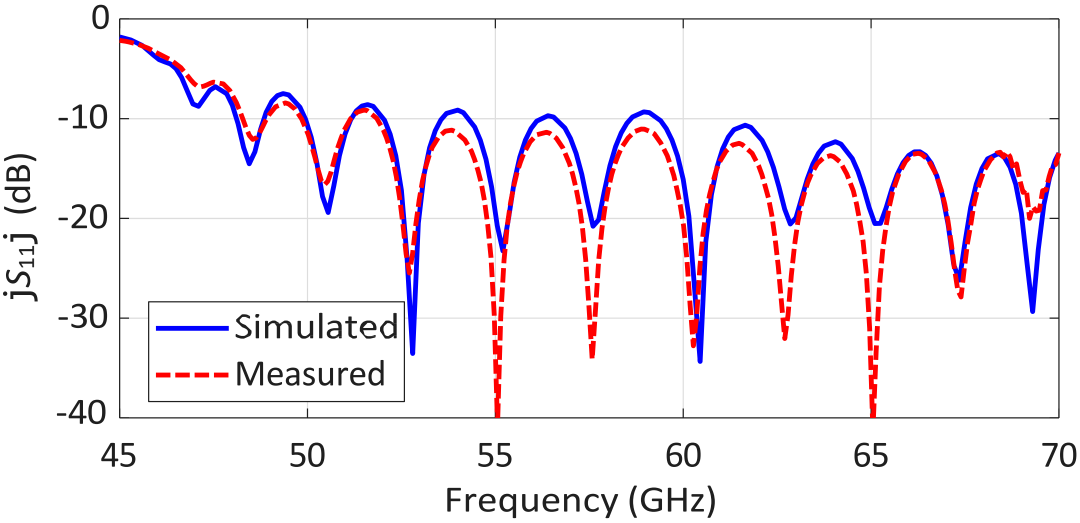

Source: Prepared by the author, 2025.

array are shown in Figure 61. The main lobe is directed toward broadside, and the measured SLL is approximately −12 dB. Figure 62 presents a comparison between the simulated and measured radiation patterns. The results exhibit close agreement, indicating that the experimental measurements accurately validate the simulated behavior.

The array supports applications that requiring beamforming and beam-streaming capabilities. As illustrated in Figure 63, the antenna exhibits high levels of gain and directivity at different frequencies around the central frequency of 60 GHz. This enables the antenna to adjust the transmission direction of its beams to various targets, as required by the application.

Figure 60. Simulated directivity of the uniform 8-element series-fed microstrip array antenna as a function of frequency.

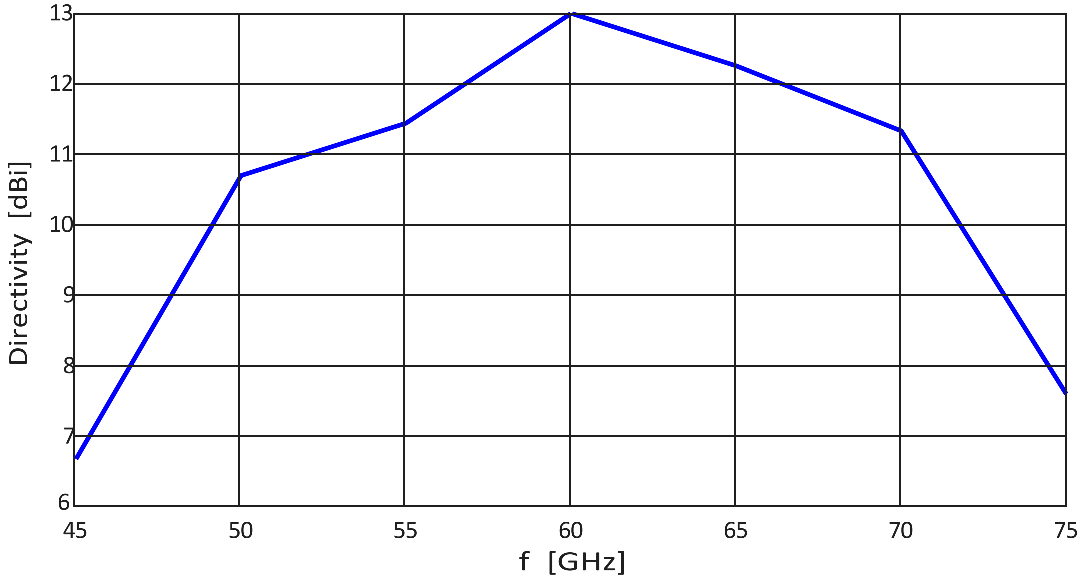

Source: Prepared by the author, 2025.

Figure 61. Radiation Pattern in plan E and H.

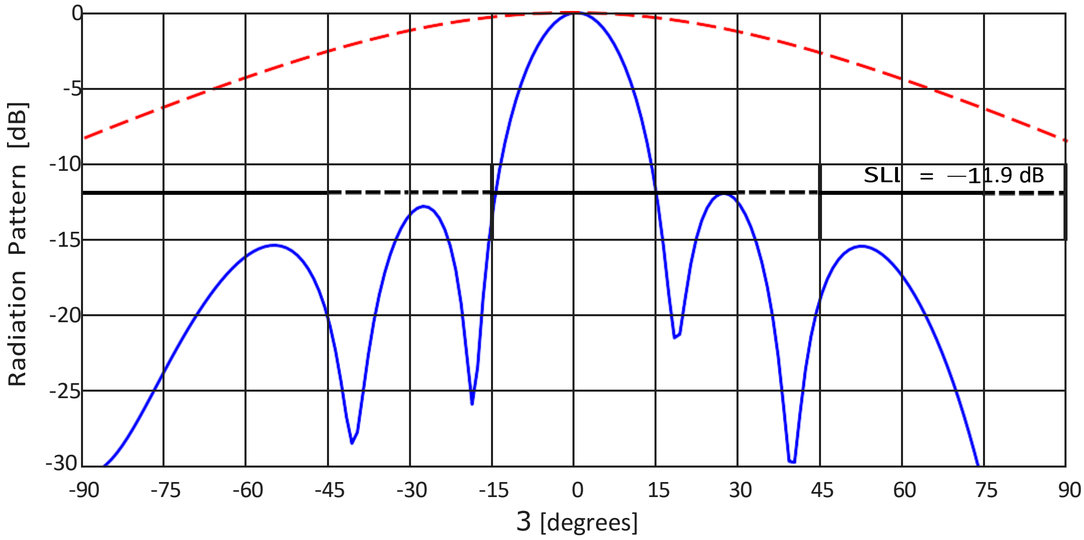

Source: Prepared by the author, 2025.

The analysis of this plot reveals a significant enhancement in the operational bandwidth as the number of elements in the array increases (Fig. 62 and 63). Furthermore, the array radiation pattern exhibits a monotonic increase with the addition of elements in a series configuration. However, the inclusion of additional elements also leads to the emergence of more pronounced side-lobes, which introduce potential interference in the antenna's radiation pattern. For the four element array, the SLL was close to −15dB. Now, with eight element, the SLL has increased to approximately −12dB. This phenomenon highlights for the next steps in this project necessities, optimizing array configurations to

Figure 62. Radiation Pattern in plan E and H.

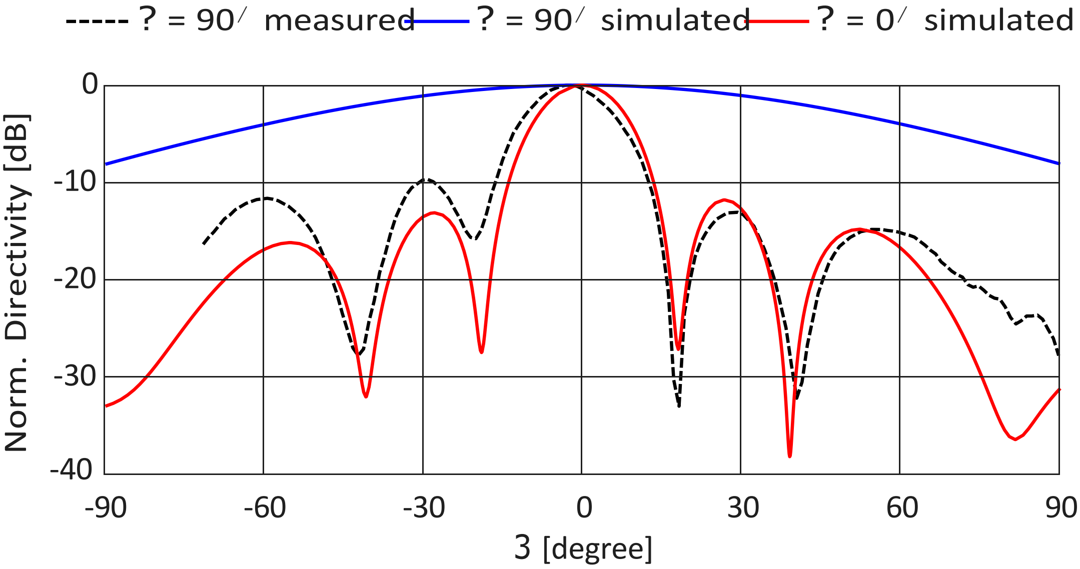

Source: Prepared by the author, 2025.

Figure 63. Measured gain plot for different frequencies.

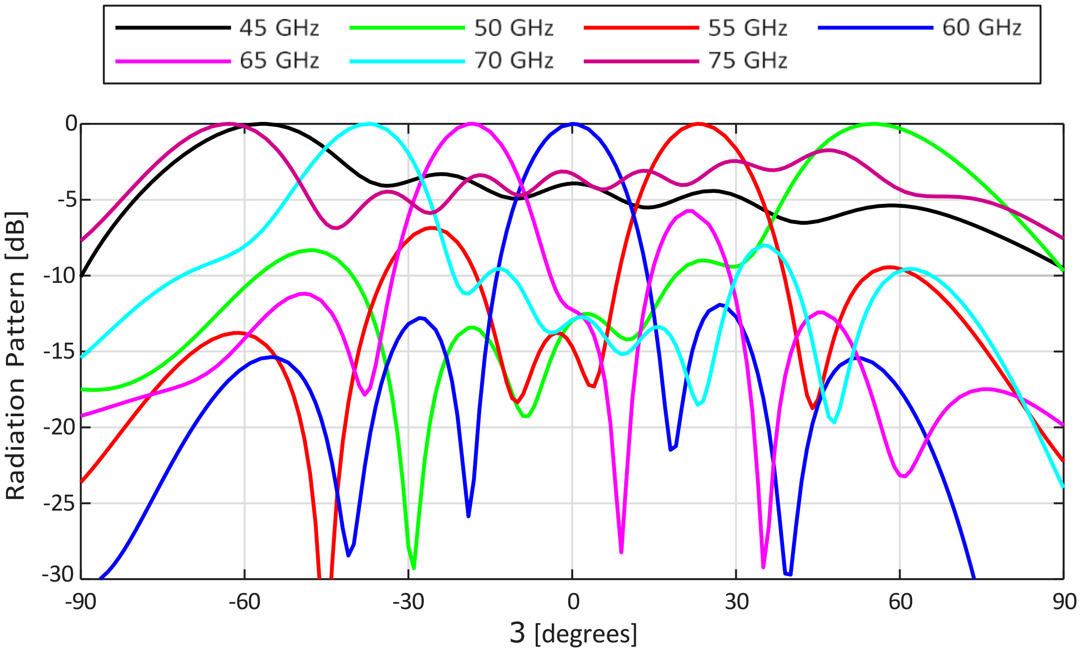

Source: Prepared by the author, 2025.

mitigate this SLL using techniques discussed in Chapter 2.

3.1.5 Taper for Side-Lobe Level of 20 dB

The array depicted in Figure 64 employs a Dolph–Chebyshev amplitude distribution to synthesize a target SLL of −20 dB below the main beam. The normalized excitation coefficients used for the eight-element configuration are $a_1 = 1.000$, $a_2 = 0.8751$, $a_3 =$

0.6603, and a_4 = 0.5799, exhibits in Table 2, are applied symmetrically with respect to the center of the array to maintain uniformity in radiation characteristics.

Figure 64. Eight-element array configuration for SLL = 20 dB at 60 GHz.

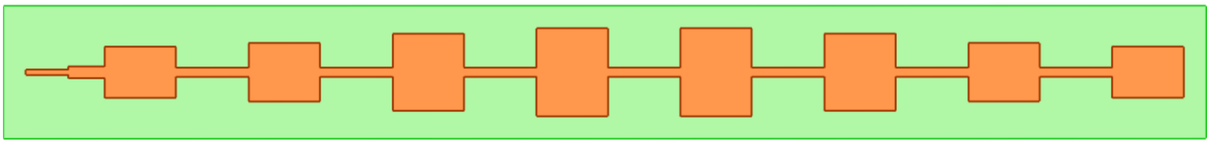

Source: Prepared by the author, 2025.

Figure 65(a) presents the simulated E-plane and H-plane radiation patterns for the non-uniform eight-element series-fed microstrip array. After optimization by simulations and parametric analysis, the SLL is reduced to −16.8 dB, from the initial value of −12 dB obtained with uniform excitation (see Figure 62). Although the design does not fully reach the intended −20 dB, the reduction in unwanted radiation represents a significant enhancement in pattern performance. A slight asymmetry is also observed, with the main beam deviating by approximately 0.6° from the boresight. To provide a more detailed view of the main-lobe behavior, Fig. 65(b) restricts the angular range to ±60°, highlighting the amplitude taper effect.

After that, to evaluate the effect of inter-element spacing on the radiation behavior, a parametric analysis was conducted, varying the spacing d between 0.93 mm and 0.98 mm. Figure 66 shows the resulting patterns over an angular range of ±90°. It is observed that reductions in d lead to a beam shift toward positive angles, exceeding +1°, while increases in spacing cause the beam to deflect toward negative directions. At the nominal value of d = 0.96 mm, the main lobe peak is located at ϑ = −0.6°, indicating a minor deviation from the array axis.

In addition to steering effects, variations in spacing also influenced side-lobe behavior. For the right-hand side-lobe, an improvement was observed as d increased, with the level improving from approximately −15 dB with nominal value to −16.8 dB for d = 0.98 mm. Conversely, the left-hand side-lobe slightly degraded, increasing from −24 dB to approximately −22 dB. Although the target value of −20 dB was not achieved, the adjustment proved beneficial in improving the overall radiation performance of the array.

The input reflection performance and impedance behavior of the array are presented in Figs. 67a and 67b, respectively. The simulated results show that the array achieves a reflection coefficient below −10 dB over a frequency range extending approximately from 45 GHz to 75 GHz, suggesting an operational bandwidth of about 20 GHz. However, localized peaks in the S_{11} response exceed the −10 dB threshold at specific frequency points, limiting the effective bandwidth for certain applications. Thus, the reported bandwidth should be regarded as an estimate rather than an absolute specification.

Figure 65. Simulated radiation patterns for the non-uniform eight-element array at 60 GHz.

(a) Radiation pattern for ±90°.

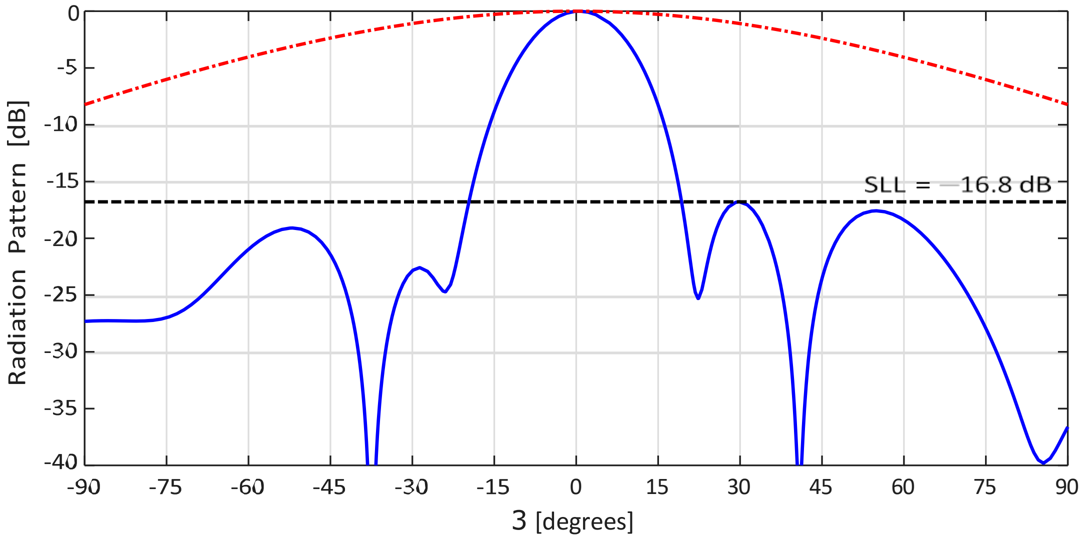

(b) Radiation pattern for ±60°.

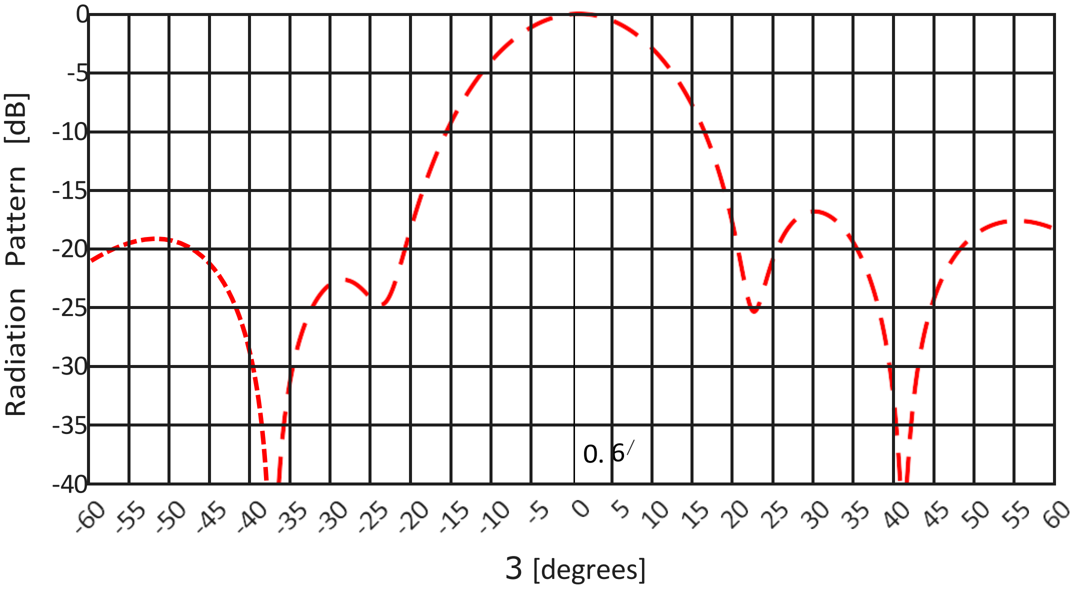

Source: Prepared by the author, 2025.

3.1.6 Taper for Side-Lobe Level of 30 dB

Now, in this case, the array configuration shown in Figure 68 employs a Dolph–Chebyshev amplitude taper to synthesize a SLL of 30 dB below the main beam. The corresponding normalized excitation coefficients are given by $a_1 = 1.000$, $a_2 = 0.8119$, $a_3 = 0.5187$, and $a_4 = 0.2622$, distributed symmetrically with respect to the center of the array to ensure balanced excitation.

Figure 69(a) presents the simulated E-plane and H-plane radiation patterns for the

Figure 66. Radiation patterns for the parametric analysis of inter-element spacing *d*.

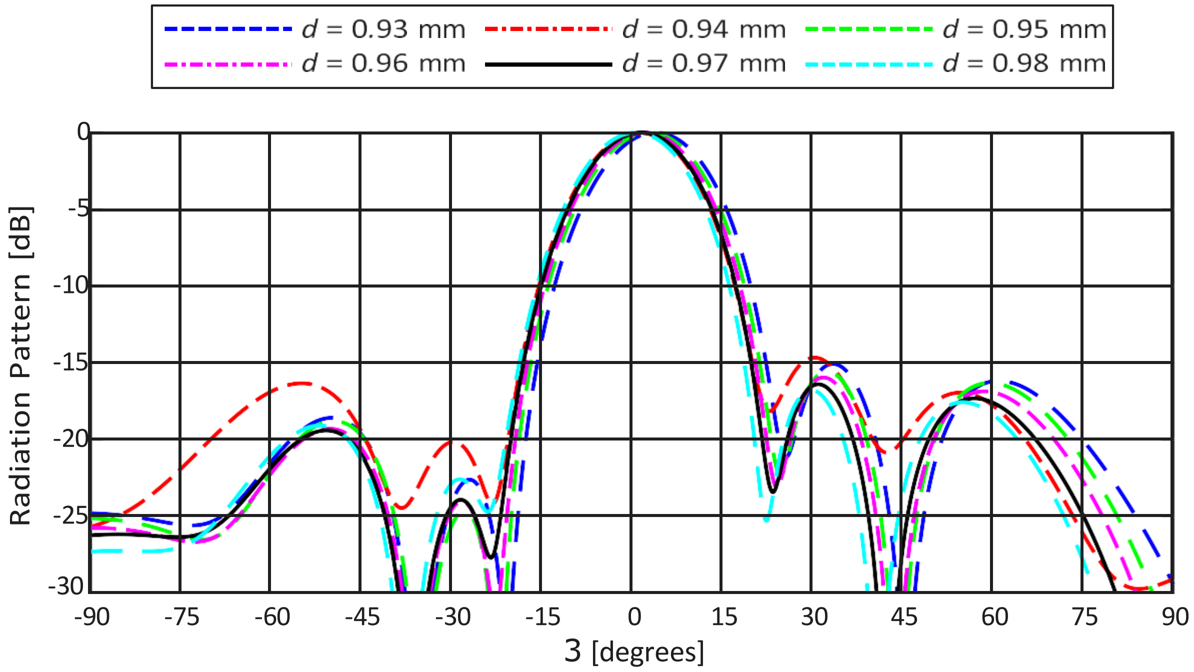

Source: Prepared by the author, 2025.

eight-element non-uniform series-fed microstrip array. The SLL is reduced to approximately 20 dB, improving over both the uniform excitation case and the 20 dB-tapered array. A slight asymmetry is observed in the radiation pattern, with the main beam shifting approximately 1.2° from broadside. Figure 69(b) presents the E-plane response limited to $\vartheta = \pm 60^\circ$, providing a detailed view of the main-lobe region and highlighting residual asymmetries and side-lobes, which may be attributed to feed line phase progression and mutual coupling effects between the elements in series.

Simillary to the previous case, to evaluate the impact of element spacing, a parametric sweep of the inter-element distance d was conducted between 0.958 mm and 0.963 mm. Figure 70 shows the radiation patterns across the range $\vartheta = \pm 90^\circ$. When d is smaller than the nominal value of 0.962 mm, the main beam shifts toward positive angles, exceeding $+1.2^\circ$, while increases in spacing result in a negative angular shift. For this case, even the parametrization, the best value found is the nominal one, that reach the smallest SLL. The beam is not fully aligned at broadside when $d = 0.962$ mm.

As observed, variations in spacing also affect side-lobe suppression. For instance, the SLL improves from approximately −17 dB in the last case discussed, to −20 dB in nominal $d = 0.962$ mm. Although the design does not meet the target SLL of −30 dB, these results demonstrate that fine-tuning of the spacing can enhance overall radiation characteristics without requiring major structural changes to the layout.

The reflection coefficient and input impedance characteristics for the array designed

Figure 67. Simulated reflection coefficient and input impedance of the non-uniform array with SLL = 20 dB.

(a) Reflection coefficient $|S_{11}|$

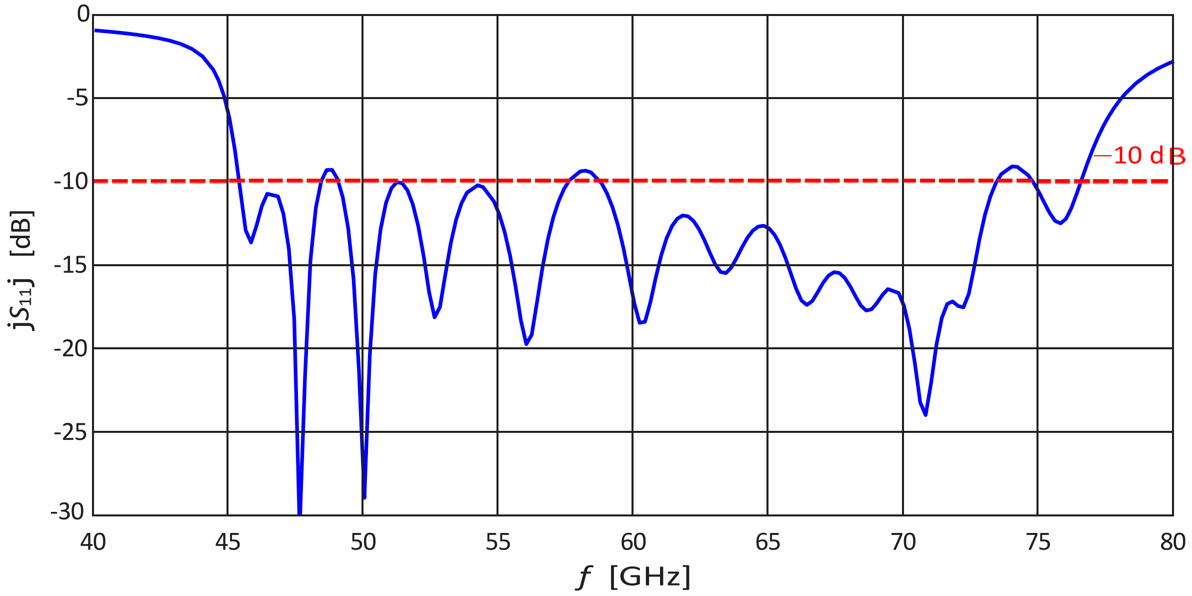

(b) Input impedance Z_{11} (real and imaginary components).

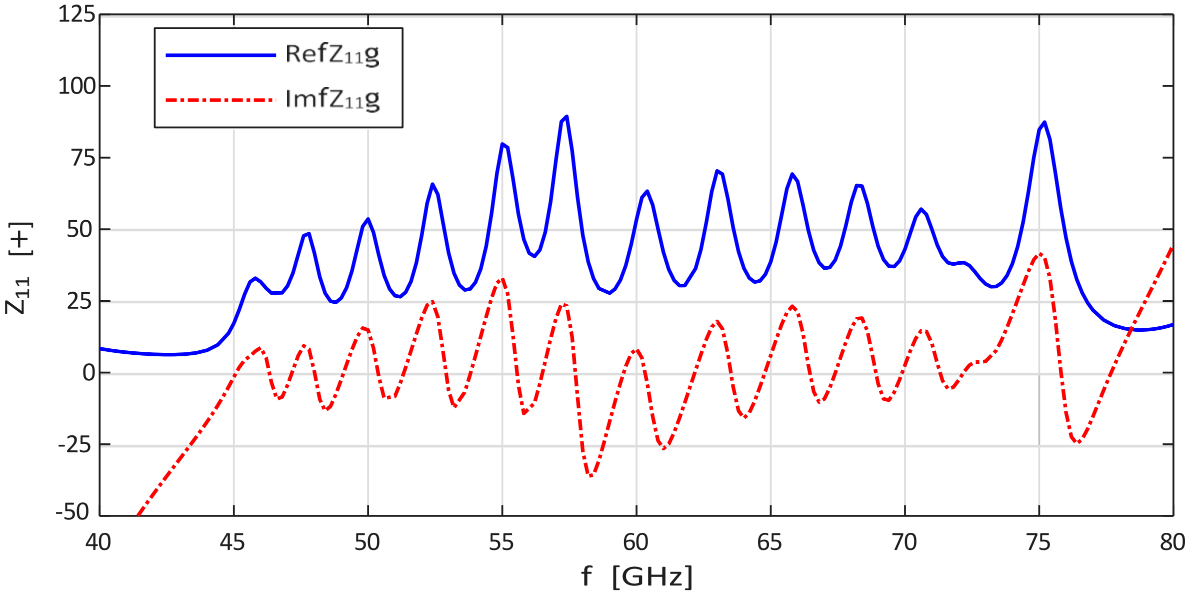

Source: Prepared by the author, 2025.

with −30 dB tapering are presented in Figure 71. As shown in Figure 71a, the $|S_{11}|$ remains below −10 dB across a wide frequency range, but exhibits three significant peaks that exceed this threshold. These deviations restrict the effective bandwidth, particularly for applications requiring tight impedance matching.

In Fig. 71b, the real part of the input impedance crosses the zero-axis multiple times over the 40–80 GHz band, suggesting multiple resonance points. These impedance

Figure 68. Eight-element array configured for SLL = 30 dB at 60 GHz.

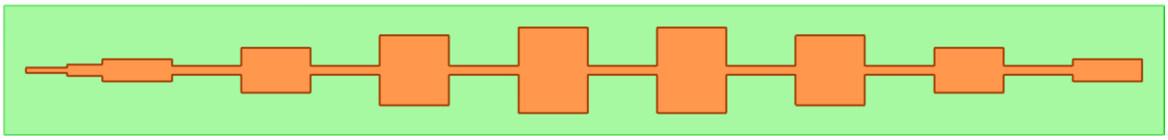

Source: Prepared by the author, 2025.

Figure 69. Simulated radiation patterns for the non-uniform eight-element array designed for SLL = 30 dB.

(a) Radiation pattern for ±90°.

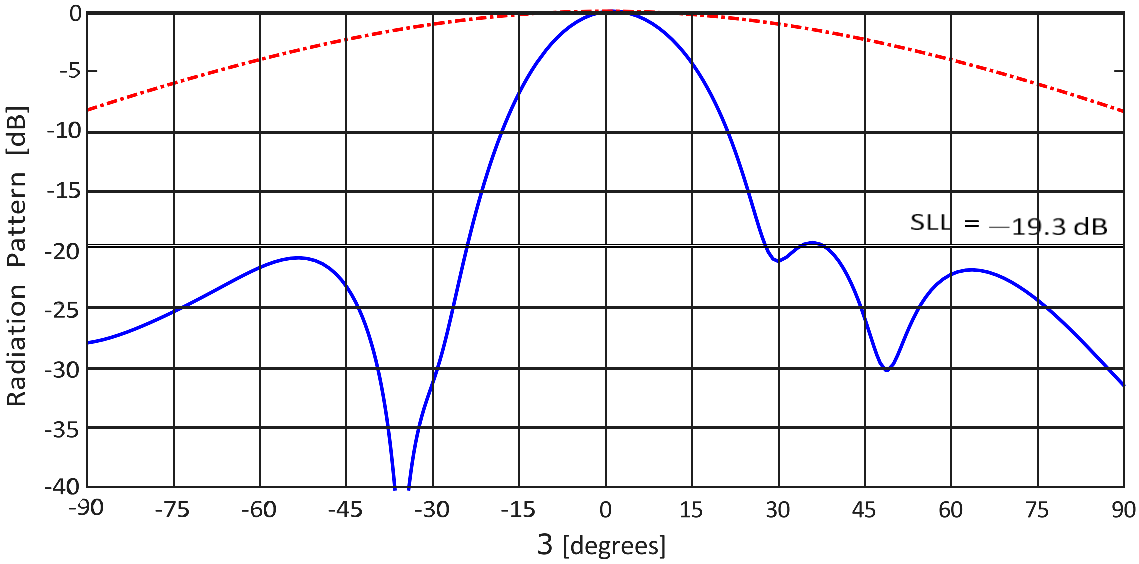

(b) Radiation pattern for ±60°.

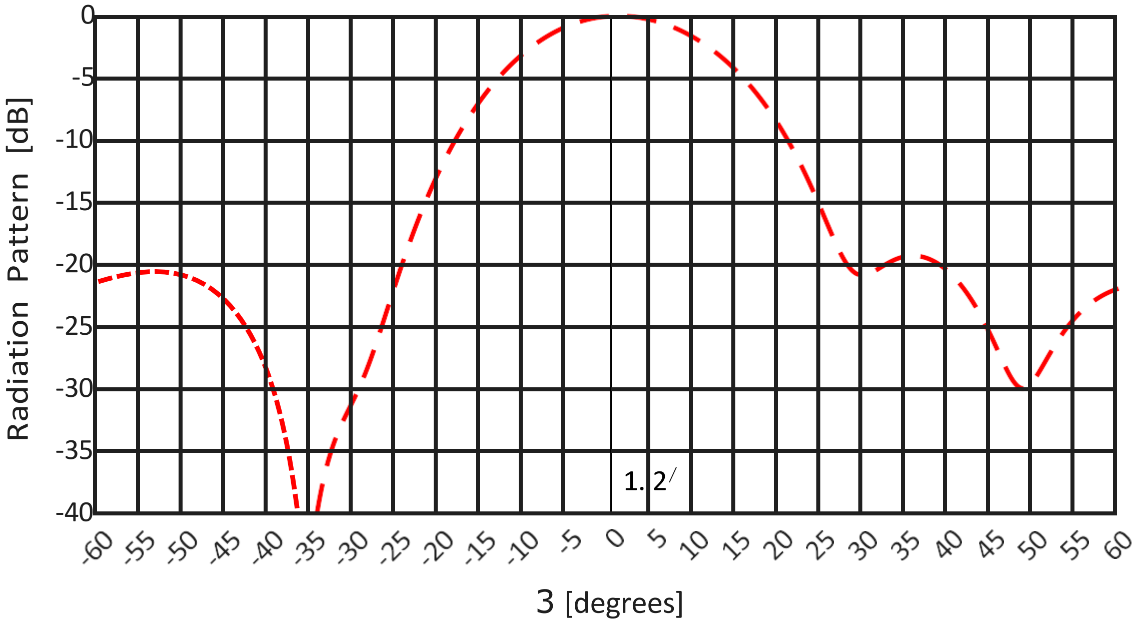

Source: Prepared by the author, 2025.

Figure 70. Radiation patterns for the parametric analysis of inter-element spacing *d*.

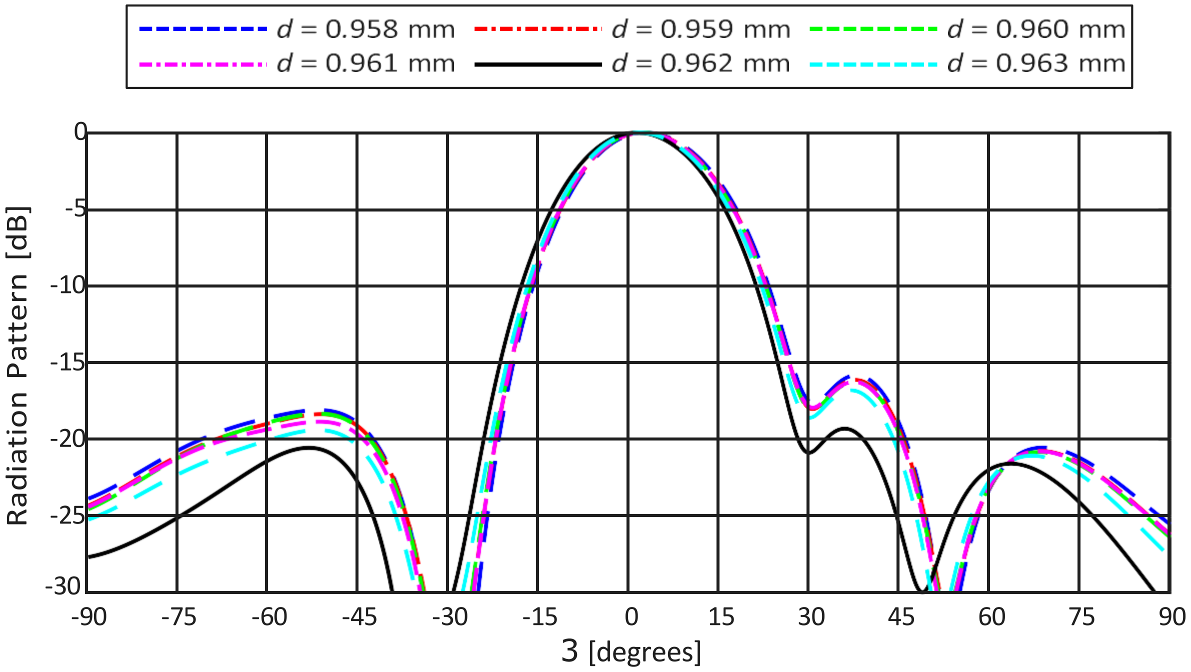

Source: Prepared by the author, 2025.

fluctuations are associated with variations in radiation efficiency and matching performance and may contribute to the degradation of $|S_{11}|$ at specific frequencies.

Figure 71. Simulated reflection coefficient and input impedance for the non-uniform array with SLL = 30 dB.

(a) Reflection coefficient $|S_{11}|$

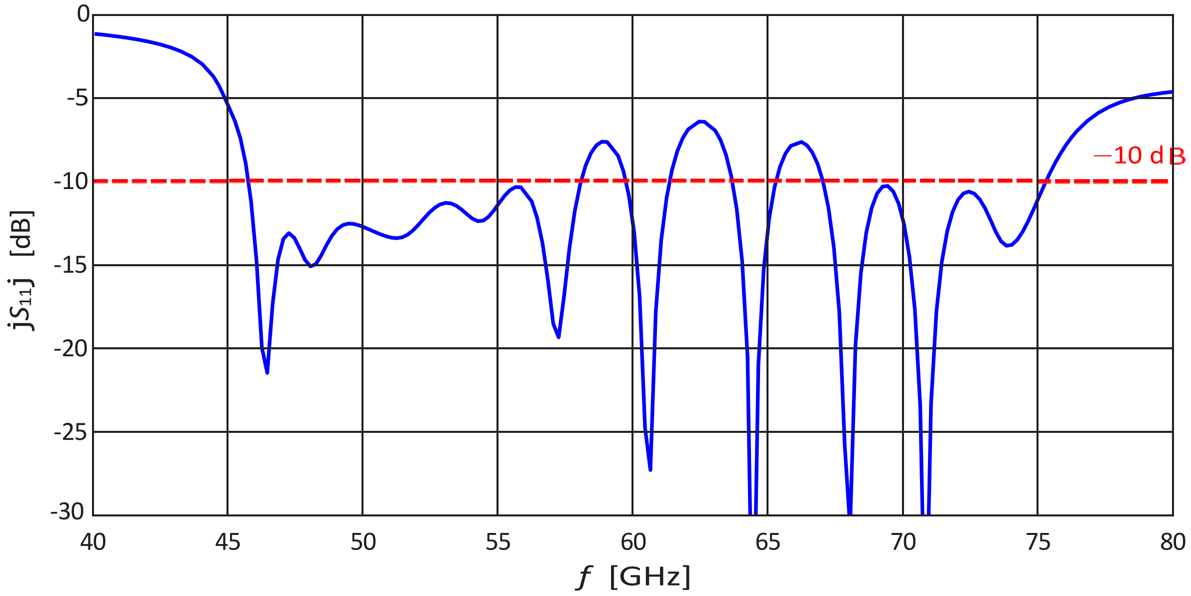

(b) Input impedance Z_{11} (real and imaginary parts).

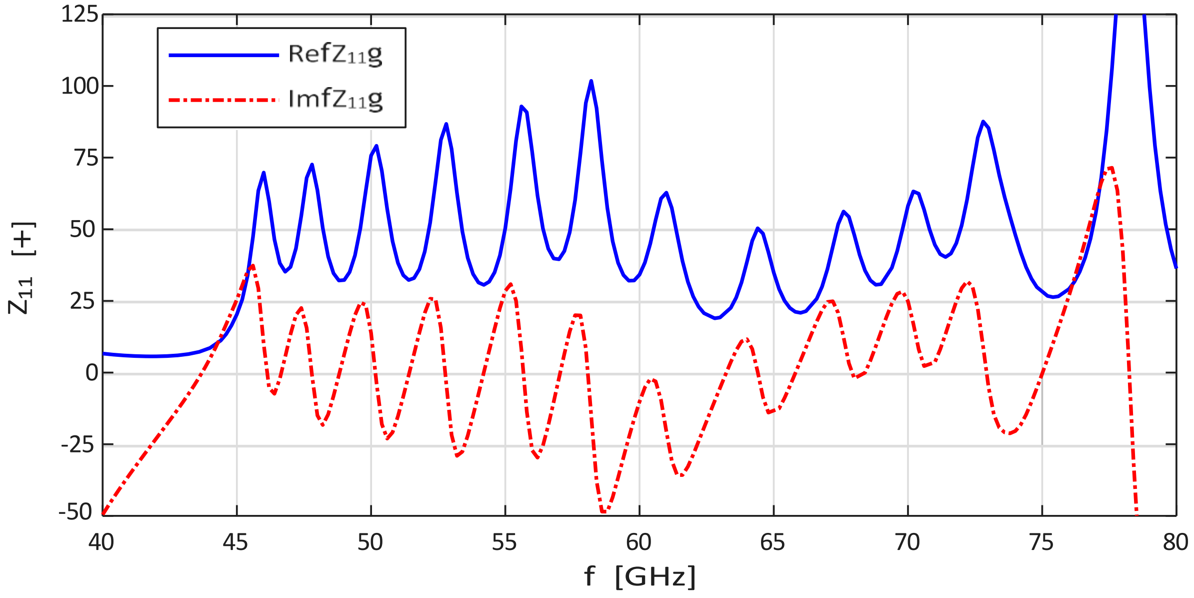

Source: Prepared by the author, 2025.

3.2 Fed-Series Array Operating at 79GHz

In this section, the studies previously conducted at 60 GHz are extended to 79 GHz, a frequency commonly used in automotive radar systems. The analysis focuses exclusively on the eight-element array configuration.

3.2.1 Single Rectangular Microstrip Antenna

Again consider a rectangular patch antenna designed for an operating frequency $f_r = 79$ GHz, with a MnM substrate having dielectric constant $\epsilon_r = 6.7$, height $h = 50$ µm, metal thickness $t = 3$ µm, and loss tangent $\tan\delta = 0.015$ (see Table 8). The feed line impedance is $Z_0 = 50\,\Omega$. The width W of the patch is calculated using the classical formula:

$$W = \frac{c}{2f_r}\sqrt{\frac{2}{\epsilon_r + 1}} \approx 0.9677\,\text{mm}.$$

The effective dielectric constant is estimated as

$$\epsilon_{\text{eff}} = \frac{\epsilon_r + 1}{2} + \frac{\epsilon_r - 1}{2}\left(1 + 12\frac{h}{W}\right)^{-1/2} \approx 6.089.$$

The fringing extension length ΔL is

$$\Delta L = 0.412h\,\frac{(\epsilon_{\text{eff}} + 0.3)\left(\frac{W}{h} + 0.264\right)}{(\epsilon_{\text{eff}} - 0.258)\left(\frac{W}{h} + 0.8\right)} \approx 0.022\,\text{mm}.$$

The effective length is

$$L_{\text{eff}} = \frac{c}{2f_r\sqrt{\epsilon_{\text{eff}}}} \approx 0.7695\,\text{mm}.$$

The actual patch length is

$$L = L_{\text{eff}} - 2\Delta L \approx 0.7255\,\text{mm}.$$

3.2.2 Uniform Array with Eight Elements

The uniform array illustrated in Fig. 72 with eight elements was designed for 79GHz. Figure 73 presents the simulated input characteristics ($|S_{11}|$, Z_{11}) of the uniform 8-element series-fed microstrip array antenna. Figure 73a(a) shows the reflection coefficient ($|S_{11}|$), which exhibits an impedance bandwidth (for −10 dB) from 63.1 GHz to 94.6 GHz, corresponding to a fractional bandwidth of approximately ≈ 40%. Figure 73b(b) shows the real and imaginary parts of the input impedance (Z_{11}). The real part oscillates between approximately 30 Ω and 60 Ω, while the imaginary part varies from about −20 Ω to 15 Ω, crossing zero multiple times, indicating the presence of several resonant conditions within the operating band.

Figure 72. Uniform eight-element series-fed microstrip array.

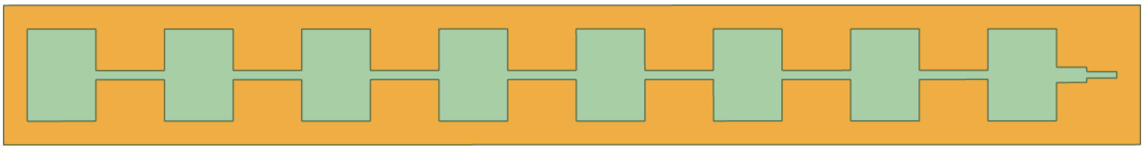

Source: Prepared by the author, 2025.

Figure 73. Simulated results for the uniform 8-element series-fed microstrip array antenna: (a) reflection coefficient (S_{11}) and (b) input impedance (Z_{11}).

(a) Reflection Coefficient $|S_{11}|$

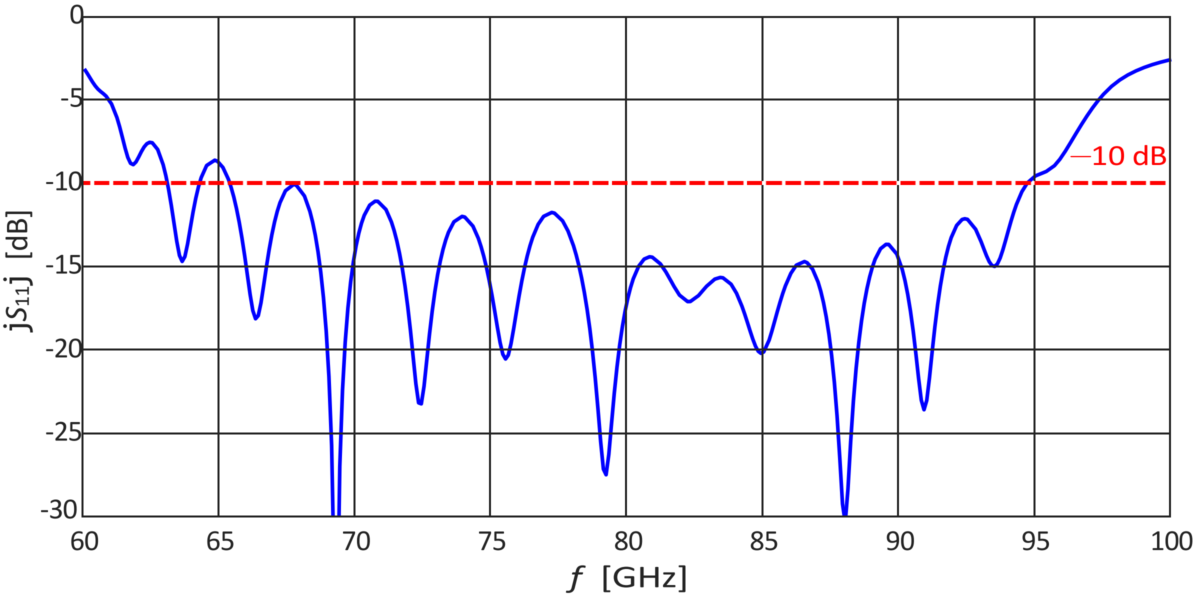

(b) Real and imaginary parts of the input impedance (Z_{11}).

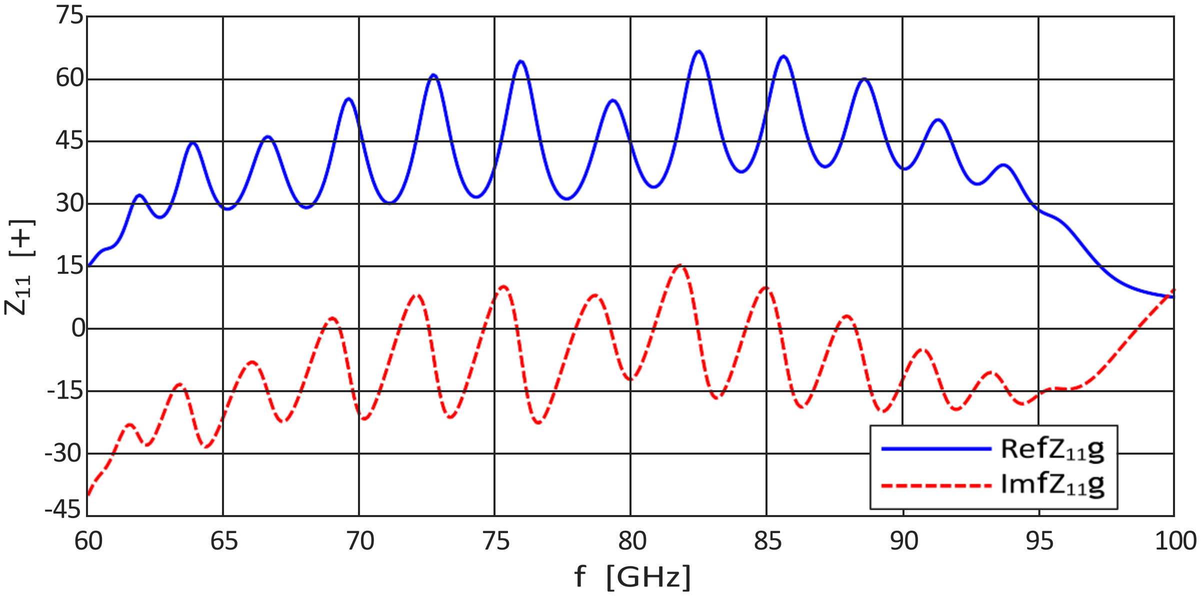

Source: Prepared by the author, 2025.

The radiation pattern of the E-plane for the uniform 8-element series-fed microstrip array are shown in Fig. 74. The main lobe is directed toward broadside, and the measured side-lobe level (SLL) is approximately −12.3 dB, similarly to the uniform array developed for 60 GHz.

Figure 76 presents the measured E-plane radiation patterns of the uniform eight-element series-fed microstrip array at 65, 70, 75, 80, 85, 90, and 95 GHz. As the frequency

Figure 74. Radiation patterns of the uniform 8-element series-fed microstrip array antenna.

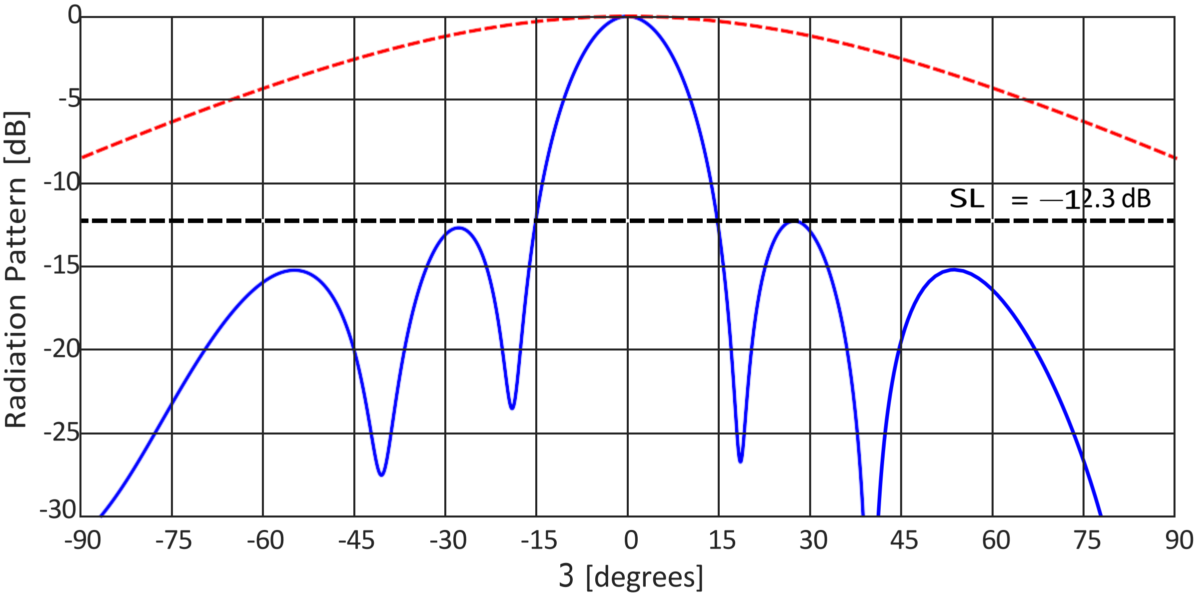

Source: Prepared by the author, 2025.

Figure 75. Simulated directivity of the uniform 8-element series-fed microstrip array antenna as a function of frequency.

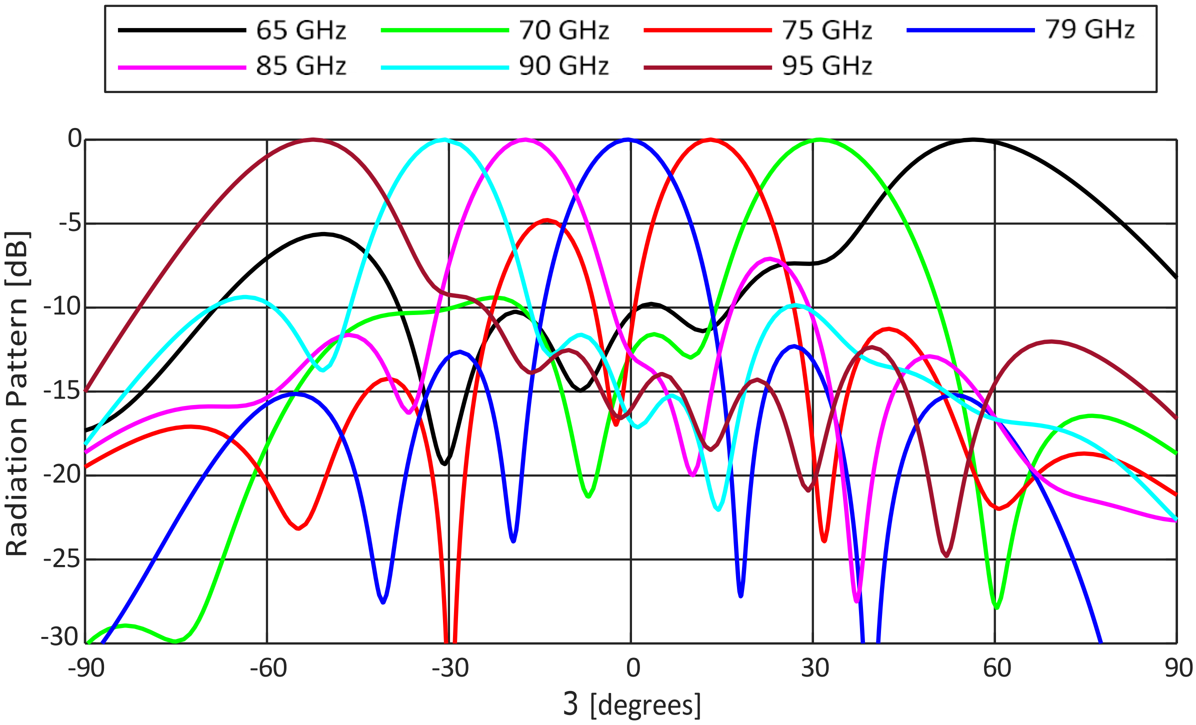

Figure 76. E-plane radiation patterns of the uniform 8-element series-fed microstrip array antenna at different frequencies.

varies, the main beam exhibits a noticeable squint, moving from 56.5° at 65 GHz toward −62.5° at 95 GHz. Intermediate directions of maximum radiation occur at −31.6°, −13.2°, −0.3°, −17.2°, and −30.1° for 70, 75, 80, 85, and 90 GHz, respectively. This pronounced

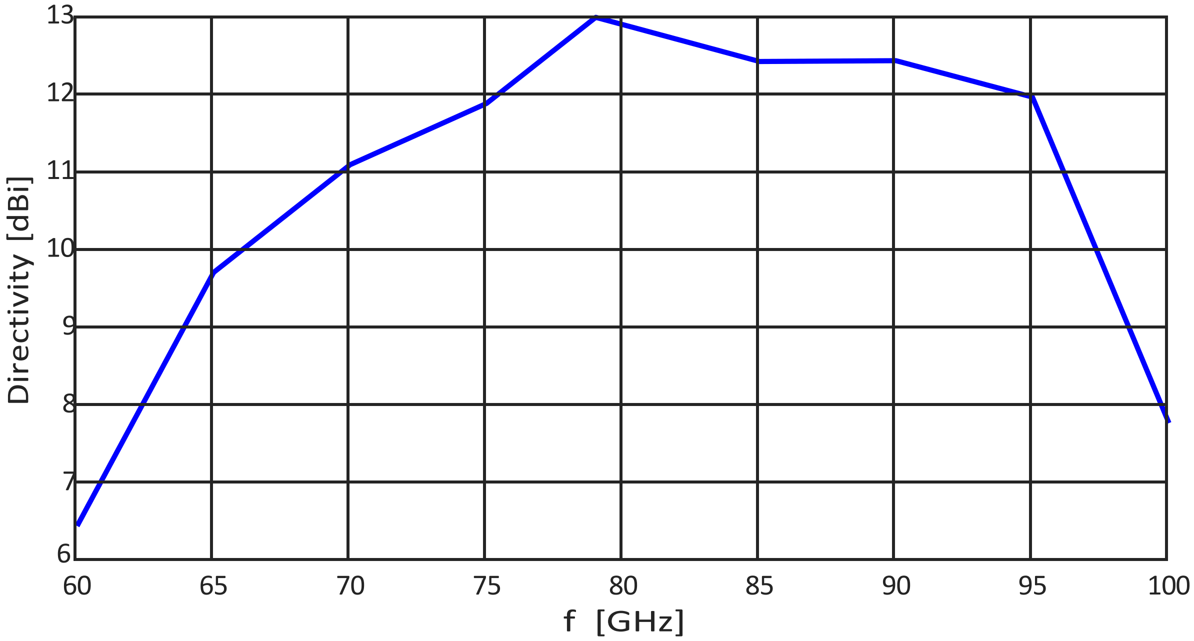

Source: Prepared by the author, 2025.

beam squint is a characteristic feature of series-fed arrays, resulting from the frequency-dependent phase progression along the feed line. Across the analyzed frequency range, variations in the SLL are also observed: the SLL reaches approximately −5 dB at 75 GHz and −7 dB at 85 GHz, while remaining around −10 dB for the other frequencies.

Figure **??** shows the simulated directivity of the uniform 8-element series-fed microstrip array antenna as a function of frequency in the 60–100 GHz range. The maximum directivity of approximately 13 dBi occurs at 79 GHz. By defining the operational bandwidth as the frequency range where the directivity remains above 10 dBi, the antenna exhibits a bandwidth from 66 GHz to 97.3 GHz, corresponding to a fractional bandwidth of approximately 38.3%. This result demonstrates that the array maintains a relatively stable radiation performance over a wide frequency range, consistent with the wideband behavior expected from series-fed configurations.

3.2.3 Taper for Side-Lobe Level of 20 dB

The array illustrated in Fig. 77 was designed using a Dolph–Chebyshev amplitude taper with a target SLL of 20 dB below the main lobe. The normalized excitation coefficients for the eight-element configuration are $a_1 = 1.000$, $a_2 = 0.8751$, $a_3 = 0.6603$, and $a_4 = 0.5799$, symmetrically applied with respect to the array center.

Figure 78(a) presents the simulated E-plane and H-plane radiation patterns of the nonuniform 8-element series-fed microstrip array antenna. The SLL is reduced to approximately 14.3 dB, representing an improvement compared to the uniform case (12.3 dB), although still below the desired 20 dB level. In addition, a slight beam asymmetry

Figure 77. Eight-element Array designed for SLL = 20 dB

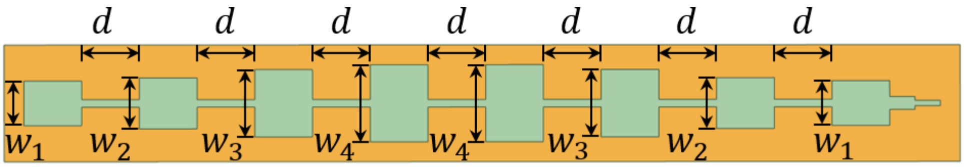

Source: Prepared by the author, 2025.

is observed, and the main radiation direction shifts to approximately 2.5°. Figure 78(b) shows the E-plane pattern limited to $\vartheta = \pm 60^\circ$, providing a clearer view of the main lobe behavior. Despite the applied amplitude taper, the pattern still exhibits noticeable asymmetry and residual side-lobes, mainly attributed to the phase progression along the feed line and mutual coupling between adjacent elements.

Figure 79 presents the radiation patterns obtained for inter-element spacings ranging from $d = 0.70$ mm to $d = 0.80$ mm, evaluated over the angular range of ±90°. It is observed that for values of d smaller than the nominal spacing ($d = 0.7255$ mm), the main beam shifts toward positive angles (above 2.5°), whereas for larger spacings, the beam steers in the opposite direction. Notably, when $d = 0.75$ mm, the main beam is precisely aligned at broadside ($\vartheta = 0^\circ$), while for $d = 0.74$ mm, the peak occurs at $\vartheta = +1^\circ$ and for $d = 0.76$ mm, the peak occurs at $\vartheta = -1^\circ$. In addition to the beam steering behavior, an improvement in side-lobe suppression was observed as the inter-element distance increased. Specifically, the SLL decreased from 15.5 dB for the initial spacing to 17 dB for $d = 0.75$ mm, indicating that a moderate increase in spacing effectively contributes to SLL reduction. Although the target value of 20 dB was not achieved, the adjustment proved beneficial in improving the overall radiation performance of the array.

The observed asymmetry is attributed to phase misalignment in the excitation of each element. Variations in the element widths introduce different phase shifts across the patches, resulting in the asymmetry. To mitigate this effect, a nonuniform element spacing strategy was adopted, with four distinct values, d_1, d_2, d_3, and d_4, arranged symmetrically, as illustrated in Fig. 80.

The first analysis focused on the element spacing d_1 (see Fig. 81), which was varied between 0.7 mm and 0.8 mm. It is observed that increasing d_1 reduces the SLL for $\vartheta > 0$, approximately at 35° and 60°. Conversely, for $\vartheta < 0$, the SLL increase around −25° and −50°. It is also noteworthy that modifying this parameter has a minimal effect on the main beam direction relative to the boresight ($\vartheta = 0$). A similar behavior is observed in Fig. 82 when analyzing d_2 in the range of 0.7 mm to 0.8 mm. Increasing d_2 reduces the side-lobe at approximately −50°, while the side-lobe at around 60° increases slightly.

Analyzing the element spacing d_3 (see Fig. 83), varied between 0.7 mm and 0.8 mm, a different behavior is observed compared to the previous cases. The side-lobes around

Figure 78. Radiation patterns for eight-element Array designed for SLL of 20 dB.

(a) Radiation pattern for ±90°.

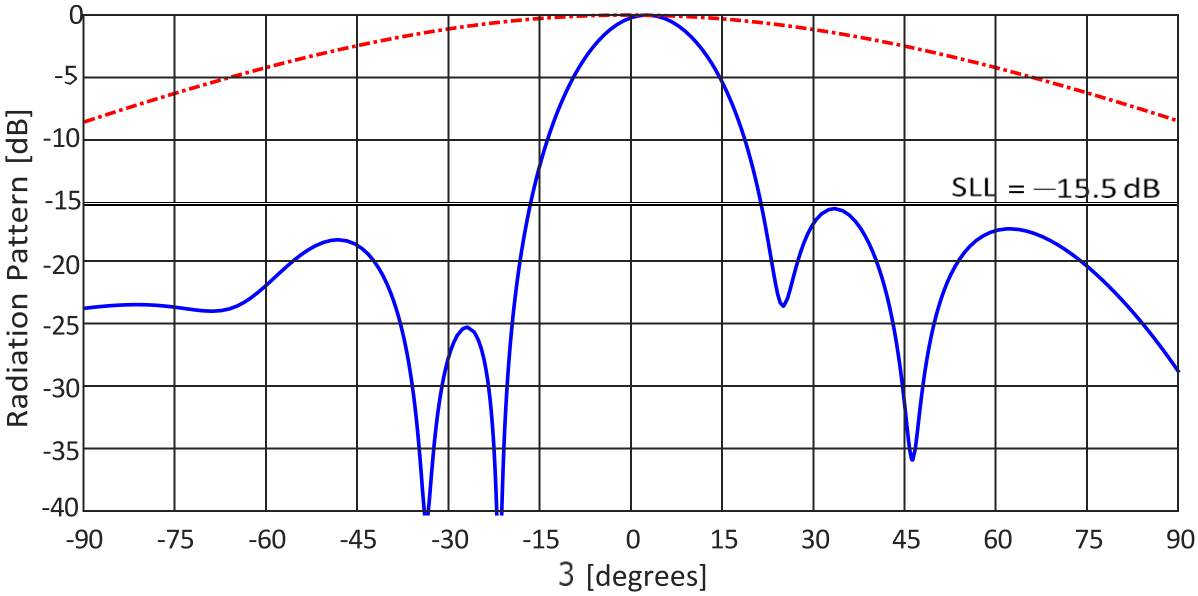

(b) Radiation pattern for ±45°.

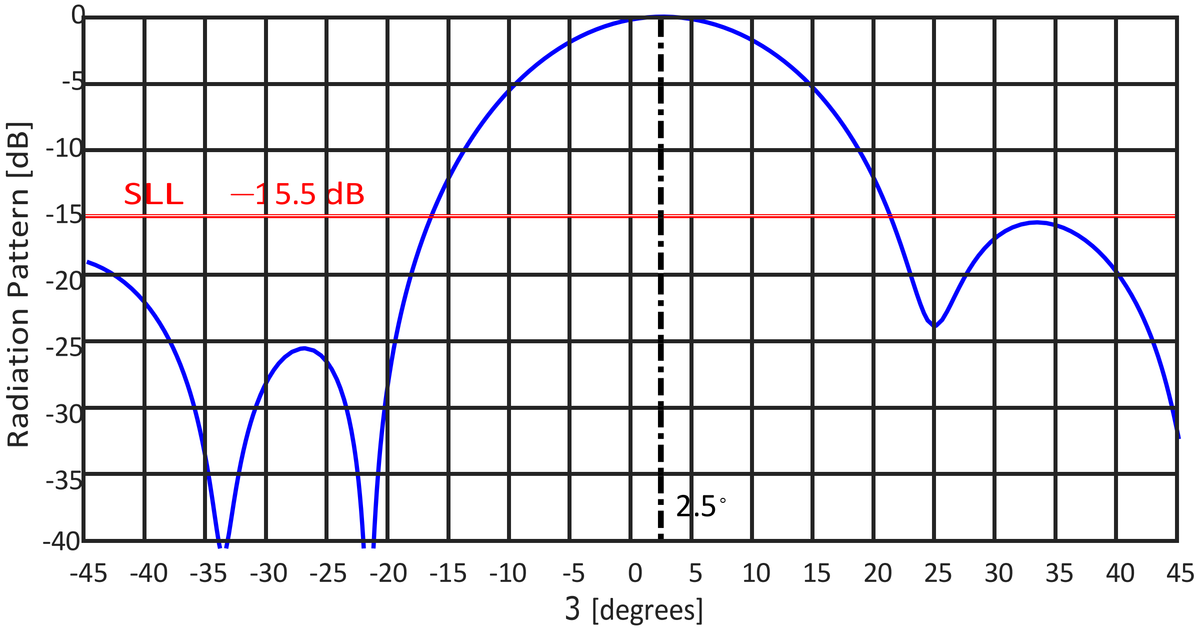

Source: Prepared by the author, 2025.

30° and 60° increase with larger values of d_3, while the side-lobe near -50° decreases. A noticeable shift of the main beam is also observed, which becomes more pronounced as d_3 increases. Finally, when analyzing the spacing between the central elements, d_4, an increase in the side-lobes near 50° and -50° is observed, accompanied by a reduction of the side-lobe around 60° as d_4 increases.

Considering the analysis performed, particularly the similarity in behavior observed

Figure 79. Radiation patterns for the parametric analysis of the inter-element spacing *d*.

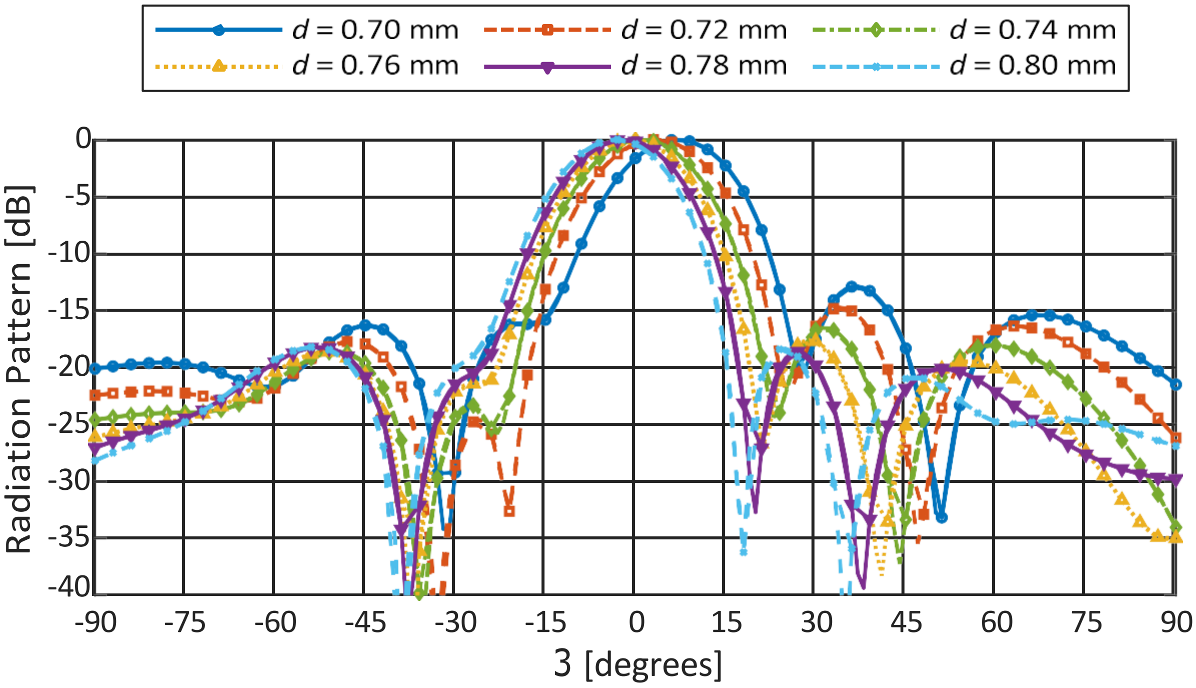

Source: Prepared by the author, 2025.

Figure 80. Eight-element Array designed for SLL = 20 dB

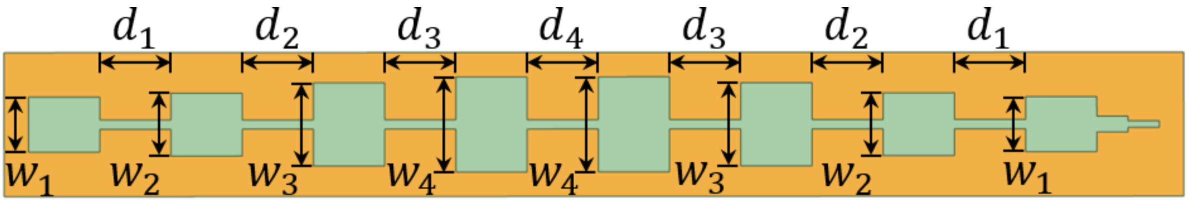

Source: Prepared by the author, 2025.

for variations of d_1 and d_2, the model shown in Fig. 85 adopts $d_1 = d_2 = d_{12}$, while $d_3 = d_4 = 0.7255$ mm. The radiation patterns obtained for different values of d_{12} (see Fig. 86), varied between 0.7 mm and 0.8 mm, show a reduction in the side-lobes near -50°, +30°, and +50° as d_{12} increases. The optimal value was found to be $d_{12} = 0.76$ mm, resulting in a minimum SLL of approximately 18.5 dB.

Figure 81. Radiation patterns for the parametric analysis of the inter-element spacing d_1.

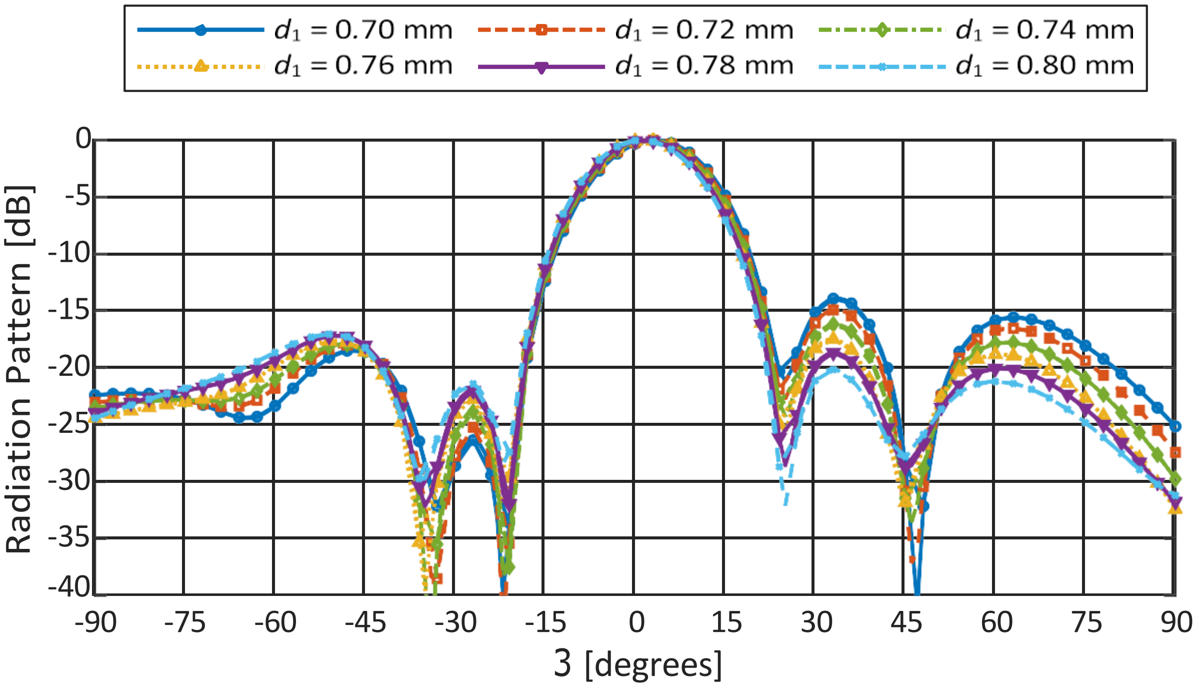

Source: Prepared by the author, 2025.

Figure 82. Radiation patterns for the parametric analysis of the inter-element spacing d_2.

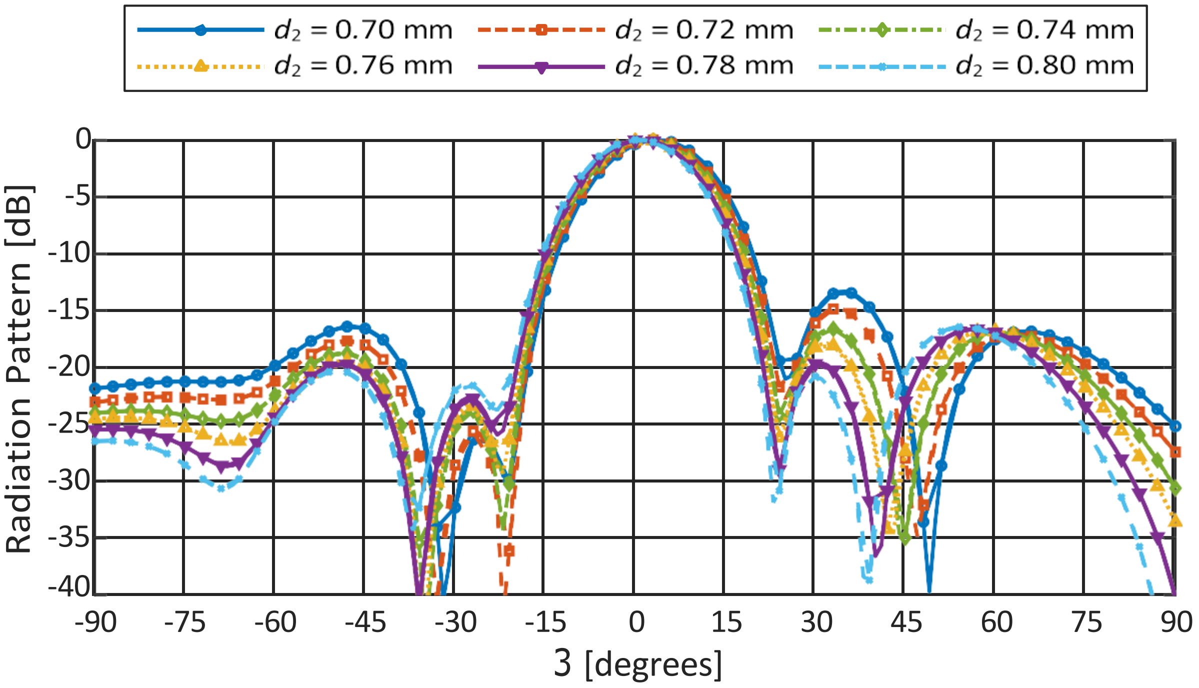

Source: Prepared by the author, 2025.

Finally, Fig. 87 illustrates the effect of element spacing adjustment on the array radiation pattern. The blue curve, corresponding to a uniform inter-element spacing, exhibits a SLL of approximately –15.5 dB. In contrast, the red curve shows a reduction in SLL to about –20 dB. This result demonstrates that proper parametrization of the

Figure 83. Radiation patterns for the parametric analysis of the inter-element spacing d_3.

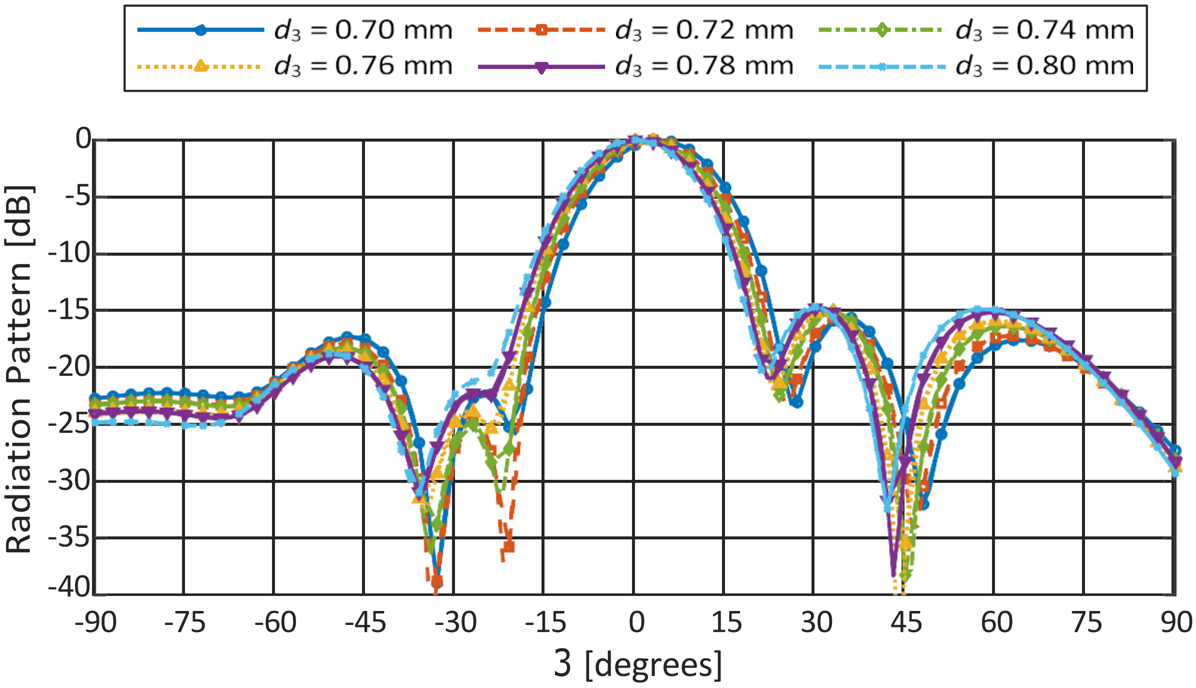

Source: Prepared by the author, 2025.

Figure 84. Radiation patterns for the parametric analysis of the inter-element spacing d_4.

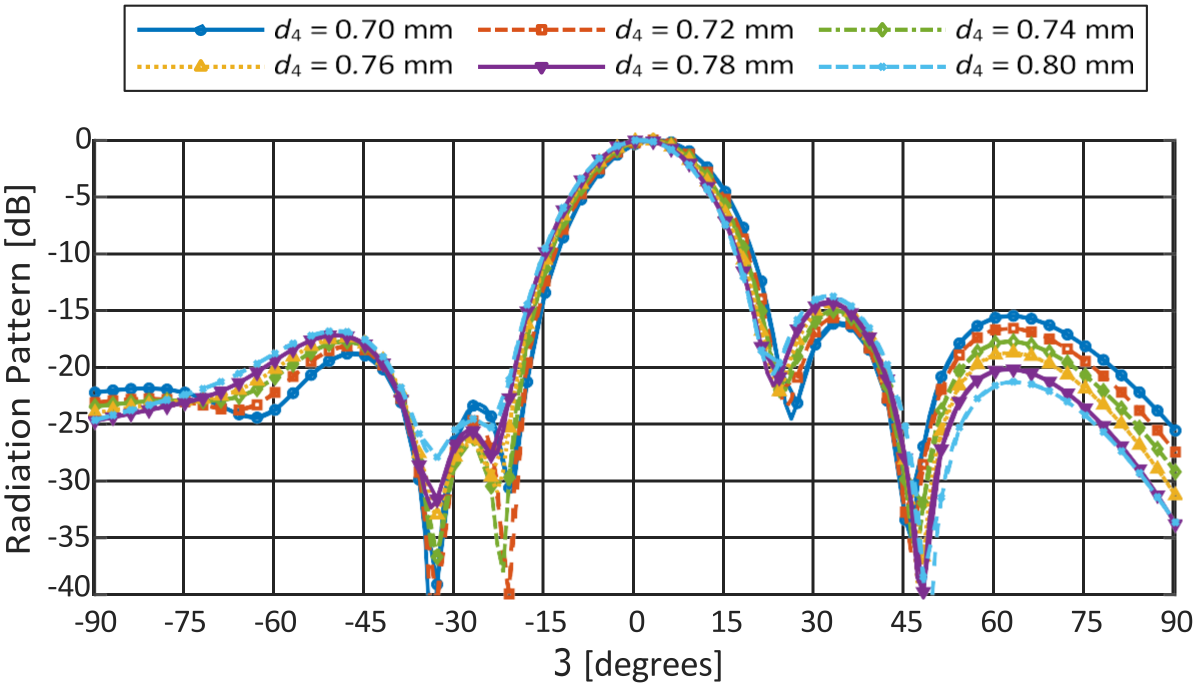

Source: Prepared by the author, 2025.

inter-element distance provides an effective means to control the SLL in the proposed array configuration.

This final configuration results in the reflection coefficient and Impedance Z shown

Figure 85. Eight-element Array designed for SLL = 20 dB.

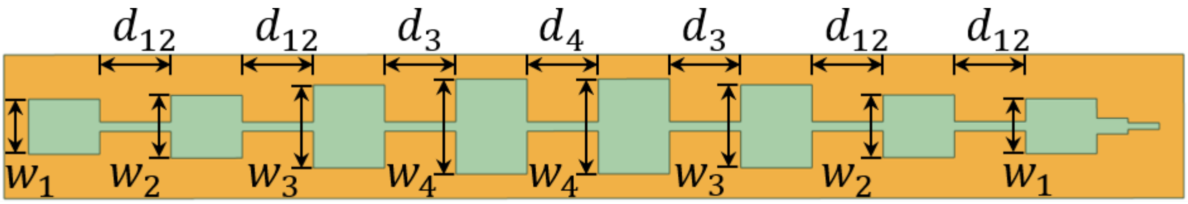

Source: Prepared by the author, 2025.

Figure 86. Radiation patterns for the parametric analysis of the inter-element spacing d_{12}.

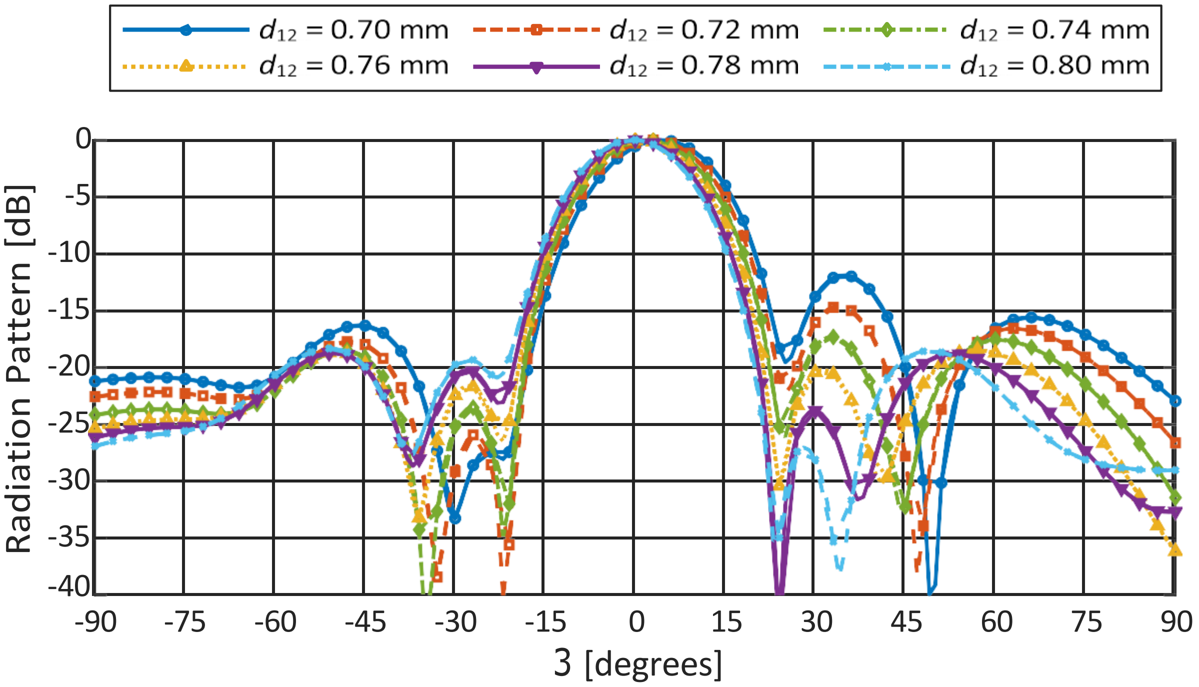

Source: Prepared by the author, 2025.

in Figures 88a and 88b, respectively.

Figure 87. Radiation patterns for optimized parameters d_1, d_2, d_3, d_4 at 79GHz.

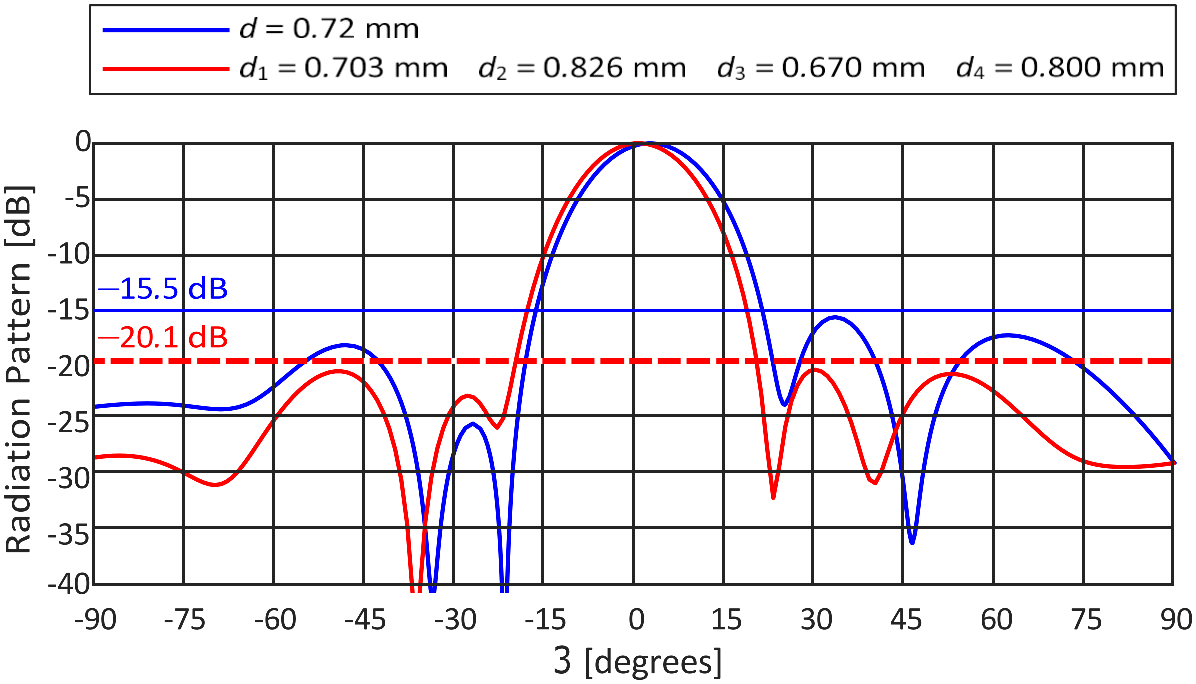

Source: Prepared by the author, 2025.

Figure 88. Simulated results for the uniform 8-element series-fed microstrip array antenna: (a) reflection coefficient (S_{11}) and (b) input impedance (Z_{11}).

(a) Reflection Coefficient $|S_{11}|$

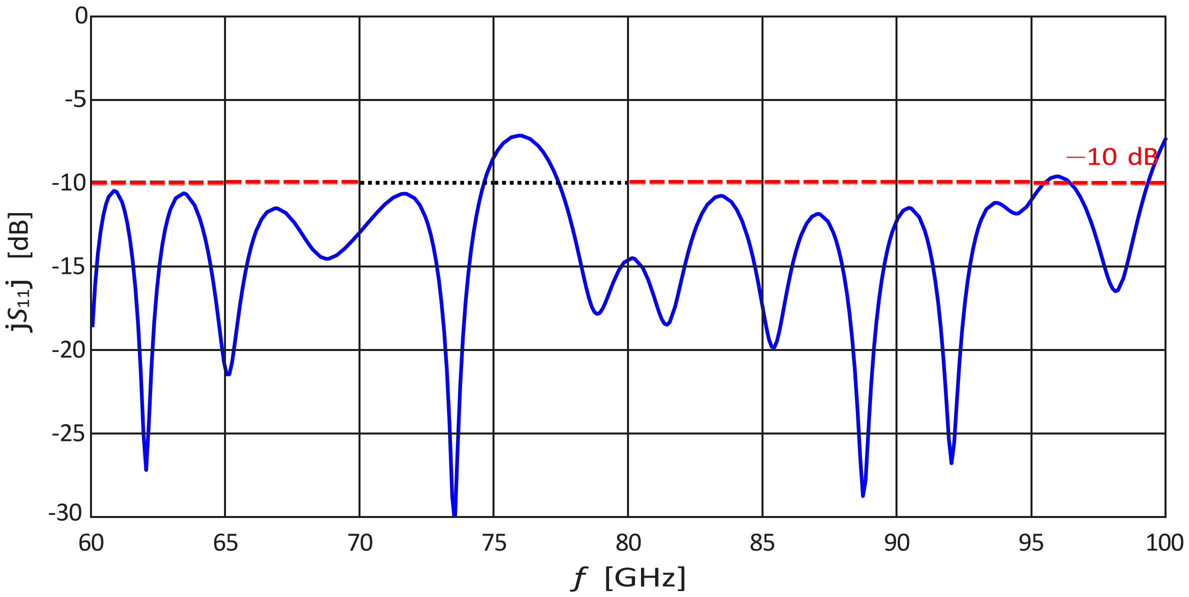

(b) Real and imaginary parts of the input impedance (Z_{11}).

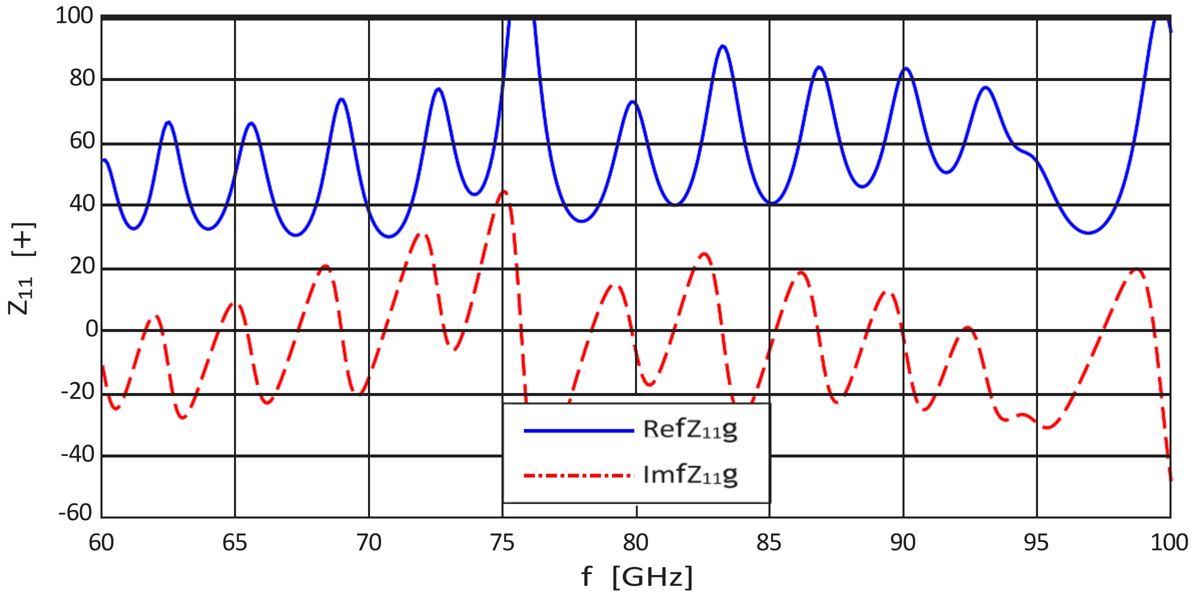

Source: Prepared by the author, 2025.

4 Conclusion

This study examined key aspects of mmW spectrum technologies, with emphasis on their applicability to high-precision automotive sensing functions such as ACC and ADAS. The growing demand for enhanced sensing performance, driven by automotive manufacturers and emerging regulatory requirements, underscores the relevance of antenna optimization methods for next-generation mmW systems.

The work conducted in this dissertation involved the design and analysis of rectangular patch antennas using the Ansys HFSS electromagnetic simulation platform. Coupling strategies and impedance-matching techniques were evaluated with the objective of achieving resonant behavior at 60 GHz and 79 GHz. To enable broadband operation, series-fed arrays were subsequently developed due to their simplicity of implementation and favorable beam-control characteristics. Arrays composed of two, four, and eight elements were designed, fabricated, and experimentally characterized in the mmWave Laboratory of Poli-USP, under the supervision of Prof. Dr. Gustavo Pamplona Rehder.

During the simulation and design phases, the emergence of multiple resonant frequencies was observed as the number of radiating elements increased. From an equivalent-circuit perspective, each additional element raises the order of the resonant system, introducing new inductive and capacitive contributions that manifest as additional resonances. While the single-element configuration exhibits only one resonance, the two-element arrangement presents a second, and arrays with four or eight elements exhibit up to eight distinct resonant points. In the eight-element case, an operational bandwidth approaching 20 GHz was achieved, with reflection-coefficient values remaining below −10 dB across the entire band (see Figure 59 and 88a). This multi-resonant behavior, identified through simulation and not extensively reported in the literature, represents a promising direction for future research on broadband mmWave arrays.

Beyond PCB-based implementations, this work also incorporated devices fabricated using metallic nanowire membranes (MnM). The MnM process enabled ultra-thin and mechanically compliant substrates with thicknesses below 50 μm, allowing conformal geometries and substantially reducing substrate-loading effects inherent to rigid PCB structures. Owing to their low effective permittivity and reduced dielectric loss, these membranes mitigated parasitic coupling in densely packed arrays and supported higher-frequency operation with improved radiation efficiency. Furthermore, the nanowire network facilitated localized control of surface impedance, enabling fine-scale tuning of inductive and capacitive behavior beyond what is achievable using conventional copper-etched laminates.

The dissertation also provided an in-depth examination of side-lobe level (SLL) reduction techniques, which are crucial in automotive sensing applications where mitigation of external interference is essential. Chapter 2 discussed several non-uniform array synthesis methods, whose effects on the radiation pattern and side-lobe suppression were evaluated. Based on this analysis, Dolph–Chebyshev tapering was applied to array configurations at 60 GHz and 79 GHz, yielding improved angular selectivity and reduced unwanted radiation outside the main lobe.

In the final stage of the study, non-uniform arrays were synthesized to target SLLs of −20 dB and −30 dB, as shown in Figures 64 and 68. Although the target values were not fully achieved experimentally, amplitude tapering significantly improved side-lobe suppression relative to uniformly excited arrays (see Figures 62, 65, 69, and 78). Inter-element spacing was also found to be a critical parameter, with parametric analysis revealing its strong influence on SLL reduction, directivity, and beam-steering performance (see Figures 66, 70, 79).

Table 10. Summary table

Array	**Freq.**	**-10 BW**	**Center Freq.**	**SLL**	**Directivity**
2X1 unif.	60 GHz	1.26GHz	59.9GHz	-8.6dB	7.4dB
4X1 unif.	60 GHz	0.89GHz	59.77GHz	-9.12dB	10.2dB
8X1 unif.	60GHz	16.9GHz	59.85GHz	-11.9dB	13dB
8X1 unif.	79GHz	27.1GHz	78.85GHz	-12.3dB	13.1dB
8X1 taper 1	60GHz	28.2GHz	59.9GHz	-16.8dB	12.65dB
8X1 taper 2	60GHz	12.5GHz	60.8GHz	-19.3dB	11.77dB
8X1 taper 1	79GHz	25.4GHz	78.9GHz	-15.5dB	12.6dB
8X1 taper 2	79GHz	25.4GHz	78.9GHz	-20.1dB	12.1dB

Source: Prepared by the author, 2025.

The methodologies and results presented in this dissertation were disseminated at the first Latin American Conference on Antennas and Propagation (LACAP 2024), which was held in Colombia. The findings generally highlight the potential of array optimization strategies that make use of combinations of emerging fabrication technologies, such as metallic nanowire membranes, to advance mmW antenna systems for use in automotive sensing and high-frequency communication applications.

BIBLIOGRAPHY

ABIR, M. A. B. S.; CHOWDHURY, M. Z.; JANG, Y. M. Software-defined uav networks for 6g systems: Requirements, opportunities, emerging techniques, challenges, and research directions. **IEEE Open Journal of the Communications Society.** *[s. l.]* v. 4, p. 2487–2547, 2023.

ALIAKBARI, H.; MOSALANEJAD, M.; SOENS, C.; VANDENBOSCH, G. A. E.; LAU, B. K. 79 ghz multilayer series-fed patch antenna array with stacked micro-via loading. **IEEE Antennas and Wireless Propagation Letters**. *[s. l.]* v. 21, n. 10, p. 1990–1994, 2022.

BALANIS, C. A. **Antenna Theory***: Analysis and Design*. Fourth. Hoboken, NJ: Wiley, 2016.

BANSAL, A.; KUMAR, A.; KUMAR, P.; GUPTA, S. **State-of-the-art millimeter-wave beam steering antennas for beyond 5g and 6g networks**: A comprehensive review. IEEE Access. *[s. l.]*. v. 12, p. 12345–12367, 2024.

BHARTIA, P.; BAHL, I.; GARG, R.; ITTIPIBOON, A. **Microstrip Antenna Design Handbook. Norwood, MA, USA**: Artech House, 2000.

CHONG, Y. I.; WENBIN, D. **Microstrip series fed antenna array for millimeter wave automotive radar applications.** IEEE MTT-S International Microwave Workshop Series on Millimeter Wave Wireless Technology and Applications. *[S.l.]*, 2012. p. 1–3.

DASH, J. C.; SARKAR, D.; ANTAR, Y. M. M. **Design of series-fed antenna array with low sidelobe level and improved azimuth fied-of-view for automotive radar application.** 2023 XXXVth General Assembly and Scientific Symposium of the International Union of Radio Science (URSI GASS). *[S.l]*, 2023. p. 1–4.

DAWN, D.; SARKAR, S.; SEN, P.; PINEL, S.; LASKAR, J. Cmos power amplifiers for millimeter-wave wireless systems. **IEEE Trans**. Microw. Theory Techn., *[s. l.]*. v. 59, n. 7,p. 1669–1678, Jul 2011.

DESHMUKH, A. A.; RAY, K. P. Analysis of broadband variations of microstrip antennas. **IEEE Antennas Propag.** Mag., *[s. l.]* v. 61, n. 4, p. 36–45, Aug. 2019.

DOLPH, C. L. A current distribution for broadside arrays which optimizes the relationship between beam width and side-lobe level. **Proceedings of the IRE**, *[s. l.]*v. 34, n. 6,p. 335–348, jun. 1946.

EDWARDS, T. C.; STEER, M. B. **Foundations for Microstrip Circuit Design**. Chichester, UK: John Wiley & Sons, 2016.

GANG, R. **Microstrip Antenna Design Handbook**. [*S.l.*]: Artech House, 2001. (Electrical engineering series).

GOVINDARAJULU, S. R.; HOKAYEM, R.; ALWAN, E. A. A 60 ghz millimeter-wave antenna array for 3d antenna-in-package applications. **IEEE Access**, *[s. l.]* v. 9, p. 143307– 143314, 2021.

HAMMERSTAD, E. O. **Equations for microstrip circuit design**. 5th European Microwave Conference. *[S.l]*, 1975. p. 268–272.

HANSEN, R. C. **Phased Array Antennas**. 2nd. ed. Hoboken, NJ, USA: Wiley, 2007.

HARRIS, F. J. On the use of windows for harmonic analysis with the discrete fourier transform. **Proceedings of the IEEE**, *[s. l.]* v. 66, n. 1, p. 51–83, jan. 1978.

HU, Y.; HONG, W. Design and analysis of mmwave series-fed patch arrays for 5g communications. **IEEE Trans**. Antennas Propag., *[s. l.]* v. 66, n. 8, p. 4132–4141, Aug. 2018.

JAMES, J. R.; HALL, P. S. **Handbook of Microstrip Antennas**. London, UK: Peter Peregrinus, 1989.

KANG, Y.; NOH, E.; KIM, K. Design of traveling-wave series-fed microstrip array with a low sidelobe level. **IEEE Antennas and Wireless Propagation Letters**, *[s. l.]* v. 19, n. 8, p. 1395–1399, 2020.

KASHINO, Y.; UNO, H.; SATO, J. **Design of millimeter-wave series-fed array antenna with loop elements.** International Symposium on Antennas and Propagation Conference Proceedings. *[S.l.: s.n.]*, 2014. p. 29–30.

KIM, K. W.; KIM, M. D.; LEE, J.; PARK, J. J.; YOON, Y. K.; CHONG, Y. J. Millimeter-wave diffraction-loss model based on over-rooftop propagation measurements. **ETRI J**., *[s. l.]* v. 42, n. 6, p. 827–836, 2020.

KRAUS, J. D.; MARHEFKA, R. J. **Antennas for all applications**. 3rd. ed. New York, NY, USA: McGraw-Hill, 2002.

LEE, J.; KIM, D. **Series-fed microstrip antenna array with inclined-beam for 77-ghz automotive radar.** In: Proc. IEEE Int. Symp. Antennas Propag. (APSURSI). Fajardo, Puerto Rico: *[s.n.]*, 2016. p. 1041–1042.

LEE, J.; PARK, S.; CHOI, J.; PARK, W.; JUNG, K.-Y. Compact series-fed microstrip patch array antenna in the 60 ghz band. AEU - **International Journal of Electronics and Communications**, *[s. l.]*. v. 187, p. 155513, 2024. Accessed on: Jun. 10, 2025. Available at: https://www.sciencedirect.com/science/article/pii/S1434841124003996.

LI, J.; MATOS, C.; GHALICHECHIAN, N. A low-cost vertically integrated antenna array at 60 ghz with 85 **IEEE Antennas and Wireless Propagation Letters**, *[s. l.]* v. 20, n. 4, p. 513–517, 2021.

LIU, Y.; BAI, G.; YAGOUB, M. C. **A 79ghz series fed microstrip patch antenna array with bandwidth enhancement and sidelobe suppression.** International Conference on Radar, Antenna, Microwave, Electronics, and Telecommunications (ICRAMET*). [S.l.: s.n.]*, 2020. p. 155–158.

MACCARTNEY, G. R.; ZHANG, J.; NIE, S.; RAPPAPORT, T. S. **Path loss models for 5g millimeter wave propagation channels in urban microcells.** In: Proc. IEEE Global Telecommun. Conf. (GLOBECOM). Atlanta, GA, USA: *[s.n.]*, 2013. p. 3948–3953.

MASUDA, H.; FUKUDA, K. Ordered metal nanohole arrays made by a two-step replication of honeycomb structures of anodic alumina. **Science**, *[s. l.]* v. 268, n. 5216, p. 1466– 1468, 1995.

METZ, C.; EBERHARDT, J.; BANGERT, A. Series-fed microstrip patch antenna array for 60-ghz wlan/wpan applications**. IEEE Antennas Wireless Propag**. Lett., *[s. l.]* v. 3, p. 252–255, 2004.

MOHAN, M. P.; JIMENO, J. M.; MEI, S.; ALPHONES, A.; SIYAL, M. Y.; KARIM, M. F. Wideband matching circuit for mmwave series fed patch array antenna. **IEEE Access**, *[s. l.]* v. 11, p. 62565–62573, 2023.

NAREKAR, N. P.; BHALERAO, D. M. **A survey on obstacles for 5g communication**. In: Proc. Int. Conf. Commun. Signal Process. (ICCSP). Melmaruvathur, India: *[s.n.]*, 2015. p. 831–835.

OH, S.; Oh, J. 140-ghz affordable miniaturized array antenna-on-package for sub-thz transceiver. **IEEE Access**, *[s. l.]* v. 11, p. 132780–132791, 2023.

PARK, S. J.; PARK, S. O.; OKAJIMA, Y.; UEMATSU, K.; LEE, J. H. A compact high-performance patch antenna array for 60-ghz cmos smart antenna systems. **IEEE Trans.** Antennas Propag., *[s. l.]* v. 67, n. 5, p. 3125–3130, May 2019.

PELEGRINI, G. S.; CAVALCANTI, M. S. M.; SILVA, R. T. P.; COUTINHO, A. C. S. L. S.; FILHO, J. C. S. S.; BATISTA, J. E. S.; OLIVEIRA, F. S. L. S.; FILHO, J. D. S.; FALCãO, R. L. S.; FALCãO, R. L. S**. Interposer based on metallic-nanowire-membrane (mnm) for mm-wave applications**. IEEE MTT-S International Microwave Symposium (IMS), *[s. l.]*. p. 1–4, 2016.

PELEGRINI, M. V.; PINHEIRO, J. M.; GOMES, L. G.; REHDER, G. P.; SERRANO, A. L. C.; PODEVIN, F.; FERRARI, P. **Interposer based on metallic-nanowire-membrane (mnm) for mm-wave applications.** In: 2016 46th European Microwave Conference (EuMC*). [S.l.: s.n.]*, 2016. p. 1461–1464.

PINHEIRO, B. M. **Development of passive circuits in nanowire-membrane technology for millimeter-wave applications.** Tese (Doutorado) — Université de Limoges, 2020. Accessed on: Jun. 12, 2025. Available at: https://theses.hal.science/tel-03222173.

RAHIM, H. M.; LEOW, C. Y.; RAHMAN, T. A.; ARSAD, A.; MALEK, M. A. **Foliage attenuation measurement at millimeter wave frequencies in tropical vegetation**. In: Proc. IEEE 13th Malaysia Int. Conf. Commun. (MICC). Johor Bahru, Malaysia: *[s.n.]*, 2017. p. 241–246.

RAPPAPORT, T. S. et al. Wireless communications and applications above 100 ghz: Opportunities and challenges for 6g and beyond. **IEEE Access**, *[s. l.]* v. 7, p. 78729–78757,2019.

SAAD, W.; BENNIS, M.; CHEN, M. A vision of 6g wireless systems: Applications, trends, technologies, and open research problems. **IEEE Network**, *[s. l.]*,v. 34, n. 3, p. 134– 142, 2020.

SECGIN, S. **Evolution of Wireless Communication Ecosystems**.: Wiley-IEEE Press, 2023. The ComSoc Guides to Communications Technologies.

SHAMSAN, Z. A. Rainfall and diffraction modeling for millimeter-wave wireless fixed systems. **IEEE Access**, *[s. l.]*. v. 8, p. 212961–212978, 2020.

TAN, Q.; CHEN, K.; FAN, K.; LUO, G. **A low-sidelobe series-fed microstrip patch antenna array for 77 ghz automotive radar applications**. In: 2020 Cross Strait Radio Science & Wireless Technology Conference (CSRSWTC). *[S.l.: s.n.]*, 2020. p. 1–3.

TAN, Q.; FAN, K.; YANG, W.; LUO, G. Low sidelobe series-fed patch planar array with amc structure to suppress parasitic radiation. **Remote Sensing**, *[s. l.]* v. 14, n. 15, 2022.

THEEDA, S.; KUMAR, G. Fabrication and characterization of metallic glass nanowire- anchored microfluidic channels. **Journal of Micro and Nano-Manufacturing**, *[s. l.]* v. 13, p. 1–14, 2025.

VERONA, B. M.; SIMIONATO, E.; PALOMINO, G.; ALDAYA, I.; PENCHEL, R. A.; SERRANO, A. L. C.; REHDER, G. P. Implementation of a millimeter-wave butler matrix on metallic nanowires-filled membrane platform. **IEEE Access**, *[s. l.]* v. 12, p. 22132–22143, 2024.

WANG, H.; LI, Y.; ZHANG, Z. High-efficiency resonant series-fed microstrip antenna array for 28-ghz applications. **IEEE Trans. Antennas Propag**., *[s. l.]* v. 64, n. 12, p. 5347–5352, Dec. 2016.

WHITTOW, W. G.; CHURM, J.; VARDAXOGLOU, J. C. 3d printing materials and techniques for antennas and metamaterials. **IEEE Antennas Propag**. Mag., *[s. l.]*. v. 61, n. 6, p. 46–54, Dec 2019.

XU, J.; HONG, W.; ZHANG, H.; WANG, G.; YU, Y.; JIANG, Z. H. An array antenna for both long- and medium-range 77 ghz automotive radar applications. **IEEE Transactions on Antennas and Propagation**, *[s. l.]* v. 65, n. 12, p. 7207–7216, 2017.

XU, J.; PENG, Z.; LONG, Z.; WANG, Z. Design of microstrip patch antenna element and array on quartz glass wafer with suspended cavity based on mems technology. **Microsyst Technol**, *[s. l.]*. v. 29, p. 835–846. 2023. DOI: https://doi.org/10.1007/s00542-023-05467-0.

ZANG, S.; DING, M.; SMITH, D.; TYLER, P.; RAKOTOARIVELO, T.; KAAFAR, M. A. The impact of adverse weather conditions on autonomous vehicles: How rain, snow, fog, and hail affect the performance of a self-driving car. **IEEE Vehicular Technology Magazine**, *[s. l.]* v. 14, n. 2, p. 103–111, 2019.

ZHANG, P.; YANG, B.; YI, C.; WANG, H.; YOU, X. Measurement-based 5g millimeter-wave propagation characterization in vegetated suburban macrocell environments. **IEEE Trans. Antennas Propag**., *[s. l.]* v. 68, n. 7, p. 5556–5567, Jul 2020.

ZHANG, Y.; MAO, J. An effective method to design traveling-wave series-fed microstrip array antennas. **IEEE Antennas Wireless Propag**. Lett., *[s. l.]* v. 16, p. 2987–2990, 2017.